PRODUCTION AND CHARACTERIZATION OF KILN CAST COMPOSITE ALLOYS

BY

TIM LUCEY

A THESIS SUBMITTED FOR THE DEGREE OF DOCTOR OF PHILOSOPHY (SCIENCE)

UNIVERSITY OF TECHNOLOGY, SYDNEY

2013

CERTIFICATE OF AUTHORSHIP/ORIGINALITY

I certify that the work in this thesis has not previously been submitted for a degree nor has it been submitted as part of requirements for a degree except as fully acknowledged within the text.

I also certify that the thesis has been written by me. Any help that I have received in my research work and the preparation of the thesis itself has been acknowledged. In addition, I certify that all information sources and literature used are indicated in the thesis.

_____

Signature of Student

ACKNOWLEDGEMENTS

It is with immense gratitude that I acknowledge my supervisors for their support and friendship through the course of my PhD: Dr Richard Wuhrer for his friendship and technical assistance on a near daily basis throughout the course of my PhD, Prof. Mike Cortie who took me on when my previous supervisor left the country and who has helped me especially with the modelling sections of my thesis and the editing of it as a whole, and Dr Paul Huggett for his wealth of knowledge, supply of experimental materials and the opportunity to work on this excellent project. I look forward to future collaborations with you all as I move into the wide world of industrial research. I would also like to thank Dr Wing Yeung for his guidance at the beginning of my doctorate. I wish you all the best in your future ventures.

I would like to thank the School of Physics and Advanced Materials and specifically the Institute for Nanoscale Technology for supporting me through airfares, accommodation and registration to many conferences both within Australia and overseas. It has also been a pleasure getting to know the staff of the department and I have enjoyed many varied and stimulating conversations.

I am very grateful to Mark Reid of the University of Wollongong who assisted with the thermodynamic simulation and high temperature confocal laser scanning microscopy, and to the staff of the Microstructural Analysis Unit at UTS for their assistance when using the electron microscopes.

I would like to thank my good friend Vijay Bhatia. We have journeyed through our whole university life together and I have appreciated your friendship throughout. I hope our paths cross often as we travel from the realms of academia and into a bright and exciting future. To my friends in the Nanotech office both past and present: Marty Blaber, Burak Cankurtaran, Jonathan Edgar, Daniel Golestan, Jonathon Mak, Supitcha Supansomboon, Alex Porkovitch, Dylan Riessen, Nick Stokes and Valerio Taraschi to name but a few, I have enjoyed your friendship, knowledge and insight. I will miss playing office cricket and having chats about any topic under the sun. I wish you all the greatest success.

To my family and friends who have been right there beside me throughout my candidature I cannot put into words how grateful I am of your encouragement, I could not have done this without you. To my Mum, Dad and sister, a special thanks for your constant love and support throughout and for your genuine interest in how I was going even though some of my work must have been a bore.

And finally, to my beautiful fiancée Michaela. Thank you for being the most wonderful, understanding and loving person in the world. Your passionate enthusiasm to see me achieve my goals has seen me through many a dark day when I felt overwhelmed.

TABLE OF CONTENTS

LIST OF FIGURES

LIST OF TABLES

LIST OF EQUATIONS

PUBLICATIONS AND AWARDS ARISING FROM THIS WORK

Refereed Papers

[1] T. Lucey, R. Wuhrer, K. Moran, M. Reid, P. Huggett and M. Cortie. "Interfacial reactions in white iron/steel composites." Journal of Materials Processing Technology 212(11): 2349-2357. 2012

[2] T. Lucey, R. Wuhrer, P. Huggett, K. Moran, W.Y. Yeung and M. Cortie. "Solidification Phenomena during Casting of Stainless Steel/Cast Iron Composites." Supplemental Proceedings: Materials Properties, Characterisation and Modelling, John Wiley & Sons, Inc.: 267-274. 2012

Conference Papers

[3] T. Lucey, R. Wuhrer, K. Moran, P. Huggett and M. Cortie. "Microstructural Analysis of the Interfacial Development of White Iron/Steel Composites." Microscopy and Microanalysis 18 (Supplement S2): 1670-1671. 2012

[4] T. Lucey, R. Wuhrer, P. Huggett, K. Moran, W.Y. Yeung and M. Cortie. "Solidification Phenomena during Casting of Stainless Steel/Cast Iron Composites", in Defects and Properties of Cast Metals, M. Jolly, B. Thomas and C. Reilly (eds.), Proceedings of the 141st TMS Annual Meeting & Exhibition, March 11-15, 2012, Orlando, Florida, USA.

[5] T. Lucey, P. Huggett, R. Wuhrer and W.Y. Yeung. "Effect of Soak Time on the Microstructural Evolution at the Interface of Kiln Cast White Iron/Steel Composites." The 7th Pacific Rim International Conference on Advanced Materials and Processing (PRICM 7), Cairns, Australia. 2010

[6] T. Lucey, P. Huggett, R. Wuhrer, K. Moran and W.Y. Yeung. "X-Ray Mapping and Analysis of the Interfacial Region of Kiln Cast Composites." Microscopy and Microanalysis 16(Supplement S2): 1674-1675. 2010

[7] T. Lucey, P. Huggett, R. Wuhrer and W.Y. Yeung. "Production and Characterisation of Vacuum Cast Composite Alloys." Materials Australia & Austceram 2009, Gold Coast, Australia. 2009

Awards

[1] Castaing Award – Best Student Paper, Microscopy Society of America, 2012

[2] 2nd Prize, Presentation, Materials Australia Jules Byrnes Student Presentation Night, 2009

[3] 2nd Prize, Poster, Materials Australia Jules Byrnes Student Presentation Night, 2009

[4] 1st Prize, Poster, UTS Student Research Showcase Poster Competition, 2009

CHAPTER 1 - OUTLINE OF THESIS

The aim of this study is to develop a technique by which wear-resistant steel parts may be created in both a cost effective and energy efficient manner. Manufacture of such items has previously been carried out by techniques such as hardfacing. However hardfacing is generally expensive and time intensive, can only create relatively thin wear layers (meaning they have to be replaced regularly) and can only be used to coat relatively simple geometric shapes. As another example, the O_2 Block™ kiln casting technique whereby a molten white iron is cast directly onto a solid steel substrate in a vacuum furnace has been utilised successfully but requires the process to be conducted in a vacuum furnace. This is quite expensive and slows the production of parts due to the need to pump down the furnace after inserting the part to be cast. This extended procedure also consumes more energy with the furnace cooling and subsequently requiring to be reheated between each cycle.

In the present project I seek to develop the above casting technique further, with the specific objective of finding a means to carry out the production of composite wear-resistant steel parts in a standard or protective atmosphere. To achieve this aim I needed to elucidate the mechanisms by which joining is obtained in this technique.

Chapter Two provides an introduction for the reader into the relevant work that has been carried out by other researchers in the field.

Chapter Three presents the reader with an introduction into the chemistry and microstructure of white irons, the wear mechanisms experienced by these alloys and some basic thermal properties of white irons that must be investigated in order to minimise the oxidation of these parts. In this chapter a suitable, low melting point white iron will be selected and investigated. Steel metallurgy and the oxidation mechanisms that occur at the gas-substrate interface are also investigated. Finally, mild steel a nd two popular heat resisting steels will be assessed for their suitability as substrate materials for composite wear-resisting parts.

Chapter Four describes the development of the kiln casting process (in air) using type 310 stainless steel in conjunction with a low melting point white iron alloy. This chapter will identify the mechanisms occurring at the interface between the molten white iron and the stainless steel and consider the advantage of this kiln casting process over other techniques.

Chapter Five provides a detailed analysis of the composite interface developed between a mild steel substrate and the low melting point white iron alloy. This chapter aims to further the research conducted in chapter four by applying the technique to more commercially viable materials. The aim of this chapter is to define optimal conditions for the creation of composite parts by studying the development of the interfacial layer formed between the white iron and the steel substrate while minimising the risk of oxide formation at the interface.

Chapter Six will examine both experimental and theoretical data relating to the diffusion mechanisms at play at the interface of these composites. This information will be used to analyse the mechanisms behind the growth of the interfacial layer discovered in chapter five.

Chapter Seven outlines the conclusion of this thesis and summarises the project outcomes.

References have been listed in the sequence of their use within the main thesis text and then numerically numbered.

CHAPTER 2 - LITERATURE REVIEW

In the present study a technique for joining white iron and steel is being investigated. Traditionally a hardened steel is used in the environments where such a white iron/steel composite could be used, however the wear resistance of a white iron would generally be even better. In this chapter, an introduction is given by way of a review of the literature, explaining the research that has been undertaken in understanding the metallurgy of both white iron and steel, as well as joining techniques that have been employed to create white iron/steel composites in the past.

2.1.1 - CAST IRON

The term cast iron is used to identify the large group of ferrous based alloys that contain over 2% carbon [1]. (All compositions in this thesis are given in weight percent, unless otherwise indicated.) Cast irons are also identifiable by their eutectic phase structure after solidification. Cast irons can also contain as much as 3% silicon with additions of alloying elements such as chromium, nickel, manganese, molybdenum, copper which are used to enhance specific chemical and mechanical properties.

Despite these alloying elements, the principles of the solidification of cast irons are readily understandable via the binary iron-carbon phase equilibrium diagram (Figure 2.1).

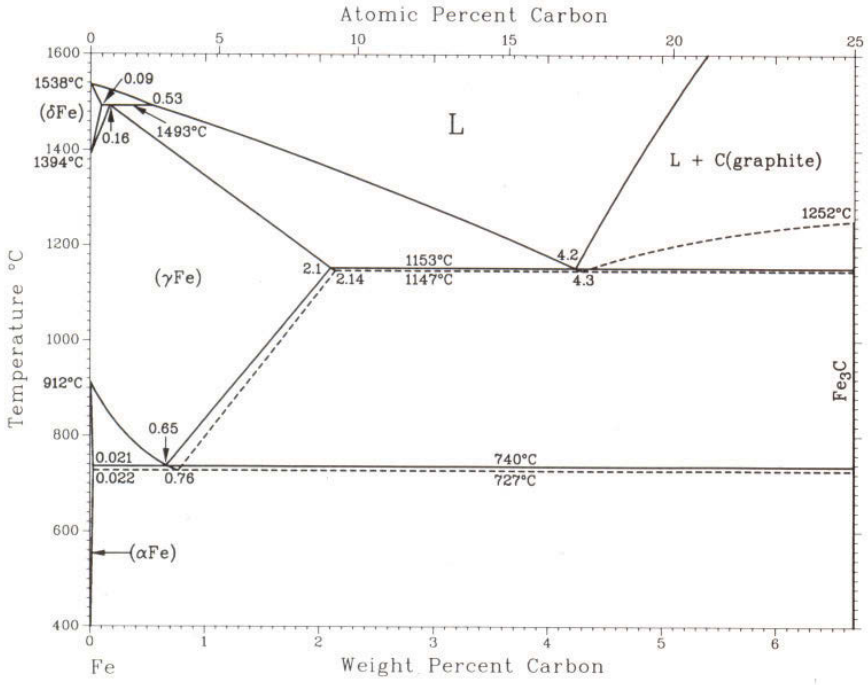

Figure 2.1: Binary Fe-C thermodynamic phase diagram[2].

This binary system allows solidification to occur in two ways:

1. as a thermodynamically metastable iron-cementite (Fe-Fe_3C) system; or
2. a stable Fe-graphite system

Under the Fe-Fe_3C system, the carbon-rich phase is iron carbide (cementite), whilst in the Fe-graphite system, the carbon-rich phase is graphite. These two basic eutectic microstructures have significantly different mechanical properties with respect to hardness, strength, toughness and ductility. The formation of a stable or metastable eutectic structure depends upon the chemical composition, cooling rate and nucleation potential of the liquid metal.

2.1.2 - Classification of Cast Irons

Historically, cast irons were classified based on the appearance of the fracture surface and were divided into two main groups:

1. Grey Iron
2. White Iron

With the advent of metallography, cast irons have been classified based on the nature of their phase microconstituents as well as the usage of the alloy. Along with the grey and white iron, two other classes of cast iron have been identified. These are:

1. Ductile Iron
2. Malleable Iron

Cast irons can also be identified according to their purpose, such as corrosion-resistant, heat-resistant, or wear-resistant irons. This study is concerned primarily with wear-resistant white irons.

2.1.2.1 - Grey Iron

Grey irons appear to have a grey fracture surface due to fracture occurring along graphite flakes. Graphite has many desirable traits due to graphite inclusions imparting excellent machinability, good wear resistance and high vibration absorption. Grey irons are generally an iron-carbon-silicon alloy that contains 2.5-4% C, 1-3% Si with additions of up to 1.2% Mn[3, 4].

Figure 2.2: Eutectic flake graphite in grey iron (Horizontal Width of Field, HWOF = 200μm)[4].

2.1.2.2 - WHITE IRON

White irons are also classified according to the appearance of their fracture, which appears white due to the fine crystalline fracture surface along eutectic carbides (Fe_3C). White irons contain an addition (e.g. chromium) which prevents the formation of graphite upon solidification and which stabilizes one or more very hard carbide phases instead. White irons have excellent wear resistance due to the formation of these eutectic carbides. Several white iron grades contain alloy eutectic carbides (M_7C_3 complex carbides), which are substantially harder than cementite, making them the most cost-effective solution for most high abrasion applications. There are a number of grades of white iron. Some examples are shown in Table 2.1.

TABLE 2.1: COMPOSITION REQUIREMENTS OF ABRASION-RESISTANT WHITE IRONS (WT.%), ACCORDING TO USAGE IN NORTH AMERICA[5].

Class	Designation	C	Mn	Si	Ni	Cr	Mo	Cu	P	S
I	Ni-Cr-HiC	2.8-3.6	2.0 max	0.8 max	3.3-5.0	1.4-4.0	1.0 max	—	0.3 max	0.15 max
I	Ni-Cr-LoC	2.4-3.0	2.0 max	0.8 max	3.3-5.0	1.4-4.0	1.0 max	—	0.3 max	0.15 max
I	Ni-Cr-GB	2.5-3.7	2.0 max	0.8 max	4.0 max	1.0-2.5	1.0 max	—	0.3 max	0.15 max
I	Ni-HiCr	2.5-3.6	2.0 max	2.0 max	4.5-7.0	7.0-11.0	1.5 max	—	0.1 max	0.15 max
II	12% Cr	2.0-3.3	2.0 max	1.5 max	2.5 max	11.0-14.0	3.0 max	1.2 max	0.1 max	0.06 max
II	15% Cr-Mo	2.0-3.3	2.0 max	1.5 max	2.5 max	14.0-18.0	3.0 max	1.2 max	0.1 max	0.06 max
II	20% Cr Mo	2.0-3.3	2.0 max	1.0-2.2	2.5 max	18.0-23.0	3.0 max	1.2 max	0.1 max	0.06 max
III	25% Cr	2.0-3.3	2.0 max	1.5 max	2.5 max	23.0-30.0	3.0 max	1.2 max	0.1 max	0.06 max

The three major classes of white iron are:

- The nickel-chromium white irons which are commonly identified by their trade name “Ni-Hard”
- The chromium-molybdenum irons
- The 25% chromium white irons, also known as high chromium white cast irons or HCWCI.

2.1.2.3 – DUCTILE IRON

Ductile iron is characterized by its ductility in an as-cast state. Ductility of these cast irons can range from 2-18% elongation to failure[1]. In comparison, both grey and white iron exhibit no significant ductility[4]. When ductile irons solidify, eutectic graphite forms as with grey iron, but due to chemical additions to the melt, the graphite

grows as spheres which alter the mechanical properties when compared to grey iron. Its relatively high ductility make it more suitable for many structural applications when compared with grey iron or malleable iron, but its complex metallurgy, specialized melting stock and need for accurate process control make it more expensive.

TABLE 2.2: DUCTILE IRON COMPOSITION (WT.%)[4, 6].

	C	Mn	Si	Cr	Ni	Mo	Cu	P	S	Mg
Ductile Iron	3.6-3.8	0.15-1.0	1.8-2.8	0.03-0.07	0.05-0.2	0.01-0.1	0.15-1.0	0.03 max	0.002 max	0.03 0-0.06

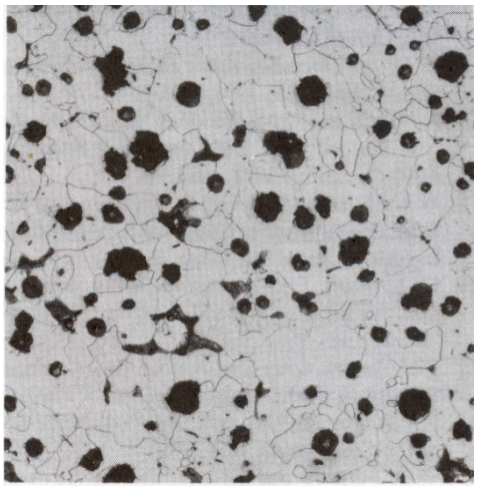

Figure 2.3: Typical microstructure of as-cast ferritic ductile iron (HWOF = 600μm)[4].

2.1.2.4 – MALLEABLE IRONS

Irregularly shaped graphitic nodules characterize the microstructure of malleable irons. Malleable iron is created by heat treating white cast iron and converting iron carbides into graphite nodules. This form of carbon is referred to as temper carbon due to its formation in the solid state during heat treatment. Malleable irons possess many of the

characteristics of ductile irons and as such have many of the same applications. However malleable irons are not suitable for thick castings due to solidification of the white iron throughout the section being essential for the production of malleable iron. Malleable iron is preferred however in applications requiring good impact resistance at low temperatures as well as good wear resistance[4].

TABLE 2.3: MALLEABLE IRON COMPOSITION[4, 7].

	C	Mn	Si	Cr	Ni	Mo	Cu	P	S
Malleable Iron	2.45-2.55	0.35-0.55	1.4-1.5	0.04-0.07	0.05-0.3	0.03-0.1	0.03-0.4	0.03 max	0.05-0.07

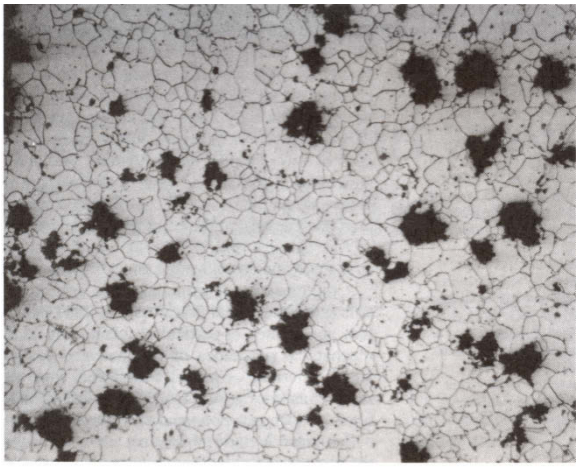

Figure 2.4: Microstructure of annealed ferritic malleable iron with temper carbon (HWOF = 950µm)[4].

2.1.3 – WHITE IRON MICROSTRUCTURE

As white iron is the focus of this study, most of my further discussion will be based on the iron-chromium-carbon system where three major microstructural types are found:

1. Hypoeutectic white iron
2. Eutectic white iron
3. Hypereutectic white iron

All three types consist of a ferrous matrix with a hard carbide phase but differ in the nature of the pro-eutectic phase formed. The ferrous phase can be austenite, ferrite, or various transformation products such as martensite or pearlite. The carbide phase is very hard and wear resistant, but is brittle. The wear resistance of the white iron is increased by increasing the carbon content and thus the amount of carbides present but this action reduces the toughness.

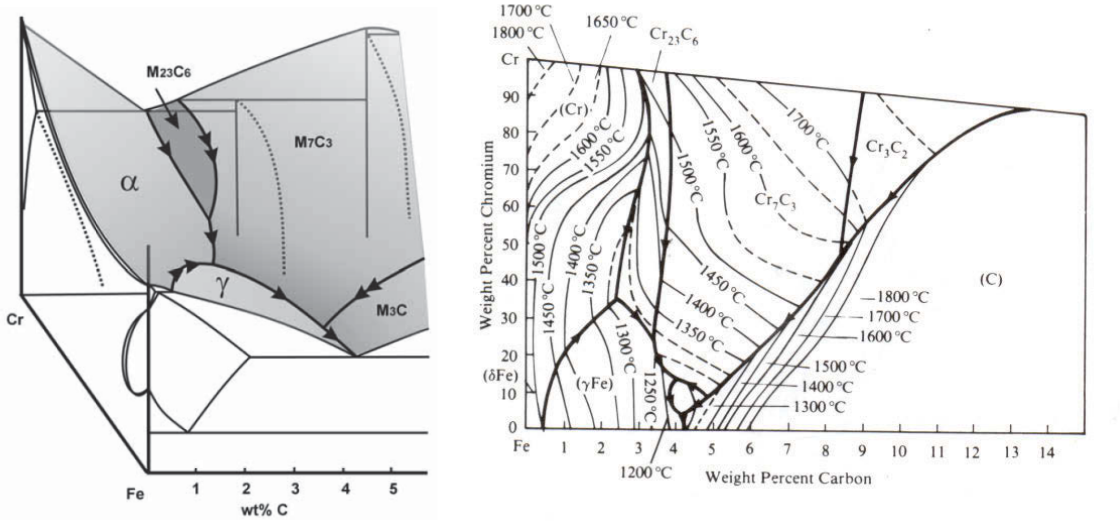

(a) (b)

Figure 2.5: (a) Metastable Fe-Cr-C phase diagram. Eutectic equilibria indicated by single arrow, double arrow indicates peritectic[8]. (b) Fe-Cr-C ternary system liquidus projection[2].

2.1.3.1 – Hypoeutectic White Iron

Hypoeutectic white iron has an austenitic pro-eutectic phase with carbides growing between the dendritic arms of the austenite. The ferrous matrix is the first phase to nucleate, creating a network of dendrites followed by the remaining liquid alloy solidifying along the eutectic temperature trough, forming M_7C_3 or M_3C carbides depending on the chromium content. Additional chromium carbide precipitates from the austenite matrix during heat treatment or slow cooling in the austenitic range.

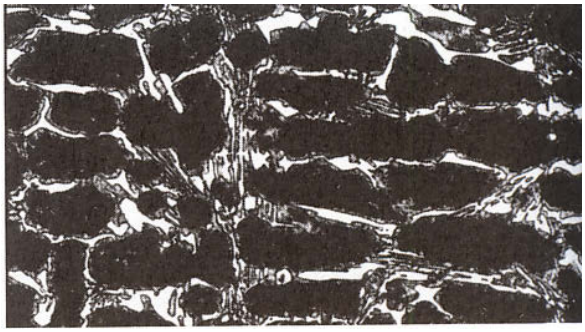

Figure 2.6: Hypoeutectic white iron microstructure. Carbides are white and matrix is black (HWOF = 800μm)[4].

Under equilibrium conditions, pearlitic transformation of the austenite occurs once it is cooled below the eutectoid temperature. As pearlite is generally undesirable due to its relatively low toughness, the white iron can be alloyed with molybdenum, manganese, nickel and copper to retard the transformation.

2.1.3.2 – EUTECTIC WHITE IRON

Eutectic white iron remains in a liquid state until the eutectic trough is reached, where both the austenite and carbide phase solidify simultaneously resulting in an interlaced structure known as ledeburite. Eutectic white irons have a continuous carbide network and if the composition lies directly on the eutectic, the microstructure is extremely fine. The nature of the eutectic microstructure can be altered by various alloying elements. The majority of the carbides formed in eutectic white iron are M_7C_3 and possess a long, rod-like structure[9]. The typical microstructure of eutectic white irons is shown in Figure 2.7. Many of the rods are seen end-on in this micrograph.

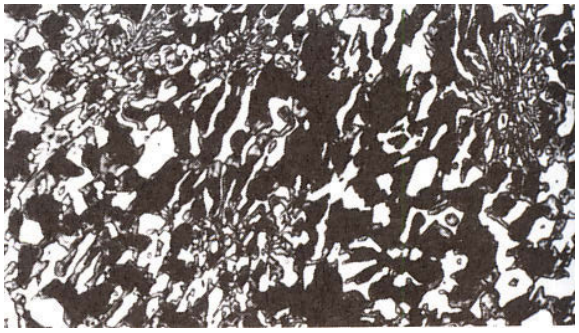

Figure 2.7: Eutectic white iron microstructure. Carbides are white and matrix is black (HWOF = 800µm)[4].

2.1.3.3 – Hypereutectic White Iron

Hypereutectic white iron consists of pro-eutectic M_7C_3 hexagonal carbides with a eutectic matrix. The primary carbides precipitate from the melt before the eutectic solidification of the austenite, creating the large hexagonal carbide rods shown in Figure 2.8. Due to the high content of both chromium and carbon, these white irons are very hard but have relatively low impact toughness.

Figure 2.8: Hypereutectic white iron microstructure. Carbides are white and matrix is black (HWOF = 800µm)[4].

The volume fraction of total carbide (both primary and eutectic) is determined by the overall chromium and carbon content. An empirical formula was derived by Powell and Lloyd[9], that estimates the carbide volume fraction. However this formula also takes into account the secondary carbides produced after heat treatment of the alloy, and is not an accurate guide when determining the carbide formed as a result of solidification.

$$\%\text{Carbides} = 12.33 \times \text{C}\% + 0.55 \times \text{Cr}\% - 15.2 \qquad \text{Equation 2.1}$$

2.1.4 – Effects of Alloying Elements in White Iron

Alloying elements have a significant effect on the properties of cast irons. In general, properties such as depth of chill (the depth to which the white cast iron microstructure was formed), hardness and strength can be improved with small additions of alloying elements, however significant improvements in abrasion resistance, corrosion resistance and elevated temperature properties require high alloy contents.

2.1.4.1 – Carbon

The main effect of carbon on the properties of white iron is an increase in hardness with increasing carbon content. Low-carbon white irons (~ 2.5% C) have a hardness of approximately 375 HB (Figure 2.9) but white irons with carbon contents of approximately 3.5% have hardness up to 550 HB in the as cast state and 650 HB after hardening [5]. Increasing carbon reduces the toughness of the alloy and also increases the tendency for eutectic graphite to form upon solidification, especially in the presence of high silicon content.

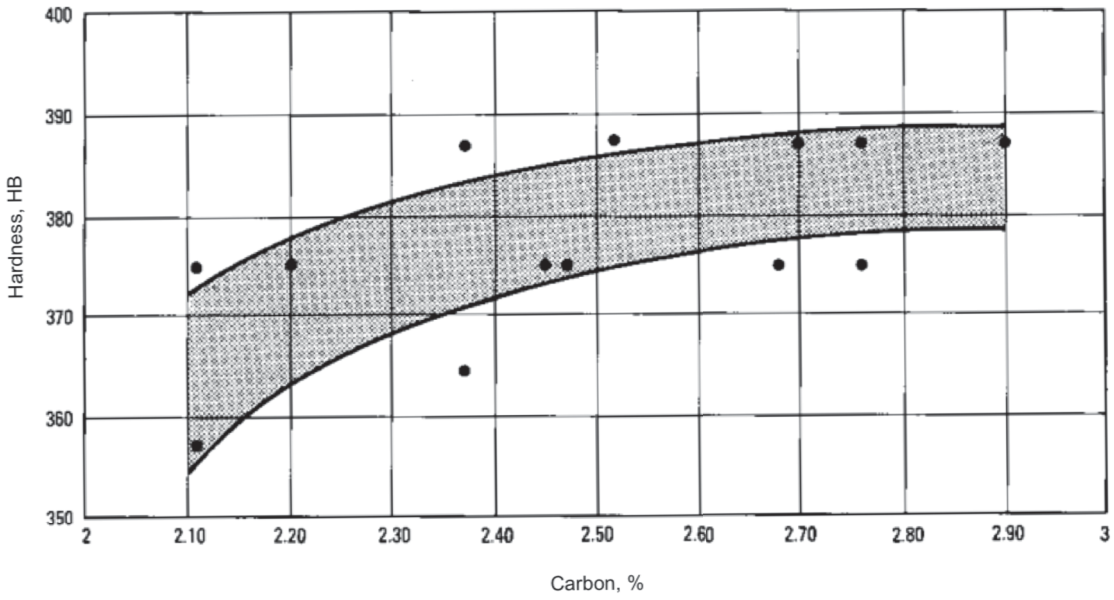

Figure 2.9: Effect of carbon on the hardness of low-carbon white iron[4].

2.1.4.2 – CHROMIUM

Chromium is the major alloying element used in white irons in addition to iron and carbon. It has three major functions:

1. To form carbides
2. To impart corrosion resistance
3. To stabilize the structure for high temperature applications

Chromium can form a variety of carbides depending on the overall composition. The form of the carbides is designated by a simple notation, where 'M' represents the major metallic alloying element(s) and carbon is represented by 'C'. The following carbide types can be typically found in chromium white irons:

i. M_7C_3 where M usually consists of chromium and iron creating a complex carbide $(Fe,Cr)_7C_3$
ii. M_3C where M is usually iron (cementite)
iii. M_2C where M is usually molybdenum
iv. $M_{23}C_6$ where M is usually chromium and iron, and occurs when the chromium/carbon ratio is high.

The presence of chromium stabilises the iron carbides and prevents them from breaking down to graphite at elevated temperatures.

2.1.4.3 – SILICON

Silicon is generally added up to 1 wt.% in order to increase the fluidity of the molten alloy during casting. As the alloy cools from the solidus temperature, the solubility of carbon in the ferrite dramatically reduces, resulting in the precipitation of carbon from the ferrite forming graphite. Silicon in high concentrations can also give good corrosion resistance, for example to sulphuric acid[10].

2.1.4.4 – MANGANESE

Fluidity can also be enhanced by the addition of manganese to the melt with generally 1% manganese added to give better fluidity. Manganese also acts as a strong austenite stabiliser providing the residual carbon level of the ferrous phase is sufficient.

2.1.4.5 – NICKEL

Nickel is a strong austenite stabiliser for white irons and also enhances the chemical resistance of the alloy. When added in amounts up to 2.5%, nickel creates a finer and harder pearlitic structure but when added above 4.5%, pearlite formation is suppressed and martensitic iron results when the casting cools.

2.1.4.6 - MOLYBDENUM

Molybdenum has two functions when alloyed with iron and chromium. When small quantities of molybdenum are alloyed, generally up to one percent, it acts as an austenite stabiliser. Above one percent additions, the molybdenum begins to form hard complex molybdenum/chromium/iron carbides.

2.1.5 – WEAR CHARACTERISTICS OF WHITE IRONS

Wear is a complex process that occurs in many different manners and for a variety of reasons. As this study is focussing on the usage of wear-resistant materials for mining applications, this next section will explain wear and how it occurs with an emphasis on wear that would be encountered by ground engaging tools (GETs).

2.1.5.1 - WEAR

Wear is a complex process that is described by Rabinowicz[11] as “the removal and deformation of a surface as a result of the mechanical action of the opposite surface”. The classification of various wear modes by Avery (which also includes corrosion as a form of wear but this is not a common definition in modern material science (Table 2.4)), separates wear into three basic categories:

1. Mechanical
2. Thermal
3. Chemical

Under each major category, several causes for wear are listed, along with various modes of interactions.

TABLE 2.4: CLASSIFICATION FOR WEAR MODES[12].

BASIC FACTOR	NOMINAL CAUSE	DESCRIPTION OF WEAR (Variables)
MECHANICAL	IMPACT	**Battering** (Stress, Deformation) **Rupture** (Stress, Deformation, Brittleness) **Cavitation** (Stress)
	FRICTION	**Smoothing** (Stress, Shear) **Seizing** (Stress, Deformation, Welding) **Galling** (Stress, Deformation, Welding, Shear)
	ABRASION	**Erosion** (Velocity, Impact, Stress, Shear) **Scratching** (Low Stress, Shear) **Grinding** (High Stress, Shear, Deformation) **Gouging** (High Stress, Shear, Impact, Deformation)
	VIBRATION	**Fatigue** (Stress reversals, Time, Cracking) **Corrosion** **Cracking** (Stress)
THERMAL	HEAT	**Creep** (Stress, Softening, Time, Deformation) **Sealing** (Oxidation, Corrosion) **Crazing** (Expansion, Stress, Deformation, Reversal, Time, Cracking, Fatigue) **Growth** (Graphitisation, Phase Change, Oxidation) **Transformations** (Expansion, Contraction, Stress, Phase Change)
CHEMICAL	CORROSION	**Solution** (Heat, Time, Chemical Action) **Erosion** (Solution, Velocity, Stress) **Intergranular** (Time, Chemical Action) **Electrolytic Action** (Heat, Dissimilar Phases) **Scaling** (Heat, Time, Chemical Action, Diffusion) **Galvanic** (Electrolytic, Dissimilar Phases) **Pitting** (Electrolytic, Dissimilar Media)

For mining applications, abrasion is the major form of wear although other forms of wear occur. In these applications, the wear process does not usually result in catastrophic failure of the material, but a gradual loss of material from the surface, which may lead eventually to the item becoming unfit for its intended purpose.

A summary of the descriptions of wear was also compiled by Zum Gahr[13]. A list of the major classification schemes for wear is given in Table 2.5.

TABLE 2.5: CLASSIFICATION OF WEAR PROCESS BY WEAR MECHANISM[13].

Burwell and Strange [14]	Abrasion, Adhesion, Corrosion, Surface Fatigue, Fretting, Erosion and Cavitation.
Jahanmir [15]	Adhesion, Delamination, Fretting, Abrasion, Erosion, Impact, Surface, Fatigue, Corrosion, Diffusion, and Electrical Contact Wear.
Godfrey [16]	Mild Adhesive, Severe Adhesive, Abrasion, Erosion, Fatigue, Delamination, Corrosive, Electrocorrosive, Fretting, Corrosive, Cavitation, Electrical Discharge and Polishing.
Rice [17]	Adhesion, Abrasion, Fatigue, Corrosion and Electrical.
DIN 50320 [18]	Adhesion, Abrasion, Fatigue, Tribochemical Reaction.

The preferred system for the classification of wear can be broken down into five major categories:

1. Abrasion: The removal of materials due to scratching.
2. Adhesion: The removal of materials due to formation and breaking of interfacial bonds.
3. Erosion: The damage caused by a second phase under motion induced by a carrier medium.
4. Corrosion: The chemical degradation of the surface.
5. Surface fatigue: The damage caused by cyclic applied stresses.

A common understanding of wear mechanisms and basic material selection for the mining industry was published in a report by the Australian Mineral Industries Research Association Ltd (AMIRA)[19]. In this report, wear was generalized as abrasion and wear of components and was deemed to be controlled by three main factors; the properties of the wear material, the properties of the abrasive material and the nature of the interaction between the abrasive and wear materials. A summary of the main factors affecting wear from this report is given in Table 2.6.

TABLE 2.6: SUMMARY OF FACTORS WHICH AFFECT WEAR[19].

ABRASIVE MATERIAL	CONTACT CONDITION	WEAR MATERIAL
Particle Shape	Force/Impact Level	Hardness
Particle Size	Velocity	Yield Strength
Particle/Material Hardness	Impact Angle	Elastic Modulus
Yield Strength	Sliding/Rolling	Ductility
Fracture Properties	Temperature	Toughness
Concentration	Wet/Dry	Strain Hardening
Characteristics	pH/Corrosivity	Fracture Toughness
		Microstructure
		Corrosion Resistance

Abrasion is defined as the loss of material due to hard particles or protrusions, forced against the surface at tangential angles[20]. Abrasive particles may be a product of the process, such as with crushing and milling, or an external component which enters the system. Hard particles can also take the form of protuberances, especially on a microscopic scale. A range of processes may occur during abrasion depending on the specific duty. Abrasive wear can be classified as either two-body or three-body, depending on the presence of free moving particles[21].

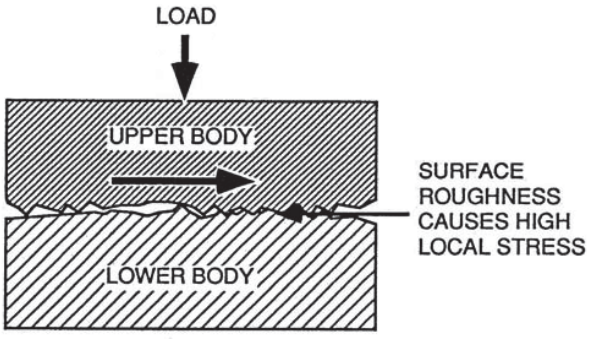

Two Body Abrasion

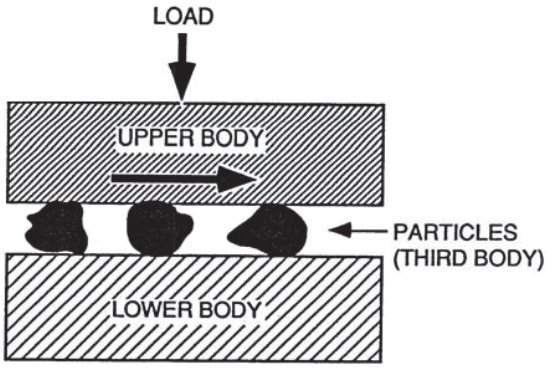

Three Body Abrasion

Figure 2.10: Two and three body abrasion models[13].

From Zum Gahr's work, four modes of abrasion are recognized (Figure 2.11):

i. Microploughing
ii. Microcutting
iii. Microfatigue and
iv. Microcracking

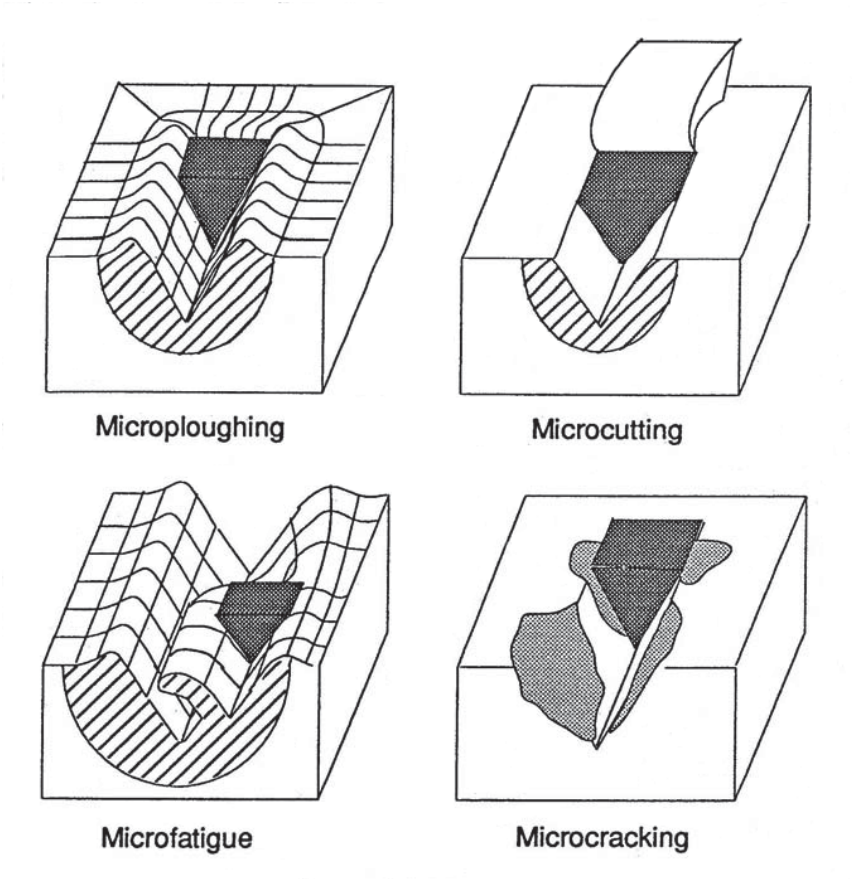

Figure 2.11: Four modes of abrasion[13].

Microploughing occurs when a deformation groove is created by an abrasive particle being dragged across the surface. The surface accommodates the deformation by allowing material to flow around the abrasive particle and as such, material loss from microploughing is negligible since rupture of the surface does not occur.

Microcutting occurs when an abrasive particle ruptures the surface of the material and is dragged, resulting in the formation of a chip. The surface does not flow around the abrasive particle and is removed by the machining action of the particle.

Microfatigue occurs under cyclic microploughing conditions. When several particles cause grooving of the material surface, lips form on the surface of the material which are subsequently sheared off with subsequent abrasive particles.

Microcracking occurs when the material surface is brittle As the abrasive particle moves across the material, the material chips at the particle/surface interface creating a

microcrack. These microcracks can propagate under repeated abrasion conditions and interconnect, resulting in spalling of the material surface.

The mechanical properties of the material determine the nature of the abrasive wear that occurs. The rate of material loss will depend on the nature of the abrasive material and the applied load. Abrasion is not velocity dependant as the volume of material removed does not increase with increasing velocity[22], however increasing the frequency of abrasion cycles will increase the amount of wear.

2.1.5.2 – Wear of White Irons

The wear of white irons is governed by their microstructure and the nature and scale of the wear system[19]. When wear is caused by abrasion or erosion due to large particles, the properties of the bulk material have the greatest effect on the wear rate, with the nature of the microstructural features playing a minor role. In contrast, in fine particle wear systems, the nature of the microstructure has the most effect on the overall wear rate.

2.1.5.3 – Effect of Mechanical Properties

In order to get a rough guide of the performance of an alloy in a wear situation, the bulk indentation hardness can be used. It has been found that homogenous alloys generally increase in wear resistance with increasing hardness [23]. Although unclear, the trend in multiphase alloys generally indicates that wear is reduced with increasing hardness. It has been found that there is no direct relationship between the hardness and wear resistance of white irons but the overall trend indicates an increase in wear resistance with increasing hardness[19].

2.1.6 – WHITE IRON LIQUIDUS

The basis of all white irons lies in the iron-rich corner of the Fe-Cr-C ternary system. Studies by Bungardt et al.[24], Jackson[25] , and Thorpe and Chicco[26] have led to a good understanding of the solidification properties of these alloys. Figure 2.12 shows a compilation of these studies in the resulting liquidus projection created by Thorpe and Chico[26].

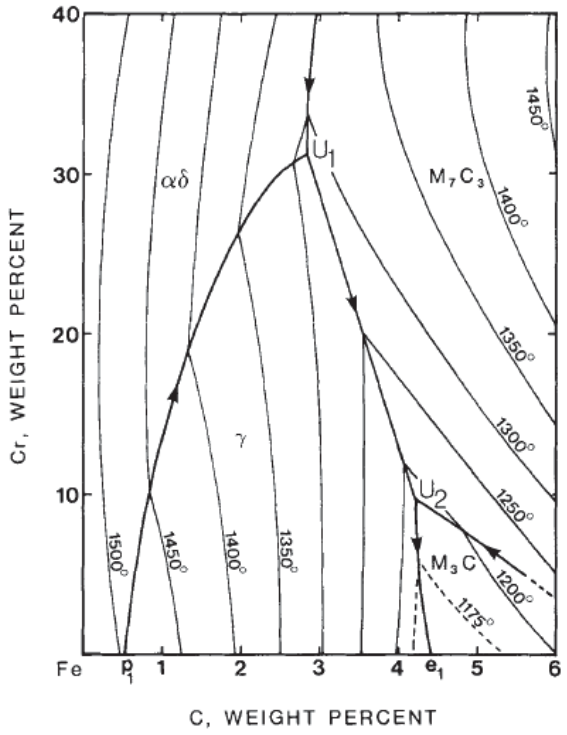

Figure 2.12: Fe-Cr-C ternary system liquidus projection[26].

Based on the liquidus projection shown in Figure 2.12, four pro-eutectic or primary phases can occur on solidification depending on the composition of the alloy:

1. Austenite (γ-Fe)
2. Ferrite (α,δ-Fe)
3. M_7C_3 Carbides
4. M_3C Carbides

The invariant liquidus reactions that are shown in the liquidus projection (Figure 2.12) are summarised in Table 2.7:

TABLE 2.7: SUMMARY OF INVARIANT REACTIONS

Invariant Location	Invariant Liquidus Reaction
U_1	L + alpha delta Fe -> gamma Fe + M_7C_3
U_2	L + M_7C_3 -> gamma Fe + M_3C
p_1	L + alpha delta Fe -> gamma Fe
e_1	L -> gamma Fe + Fe_3C

Study of the Fe-Cr-C phase diagram shows the eutectic trough follows a reducing temperature as it approaches the U2 triple point. At a composition of approximately 4 wt% carbon and 10% chromium (balance iron), the liquidus temperature is estimated to be 1200°C. However, from the perspective of commercial manufacturing, a composition consisting of just these three elements is impractical[27] because additions of other alloying elements such as silicon and manganese are needed as well.

In a study conducted by Schon and Sinatora[28] on the simulation of solidification paths for the Fe-Si-Cr-C alloy system, a range of computer predicted microstructures were compared to experimentally observed microstructures. Figure 2.13 shows the range of alloys reviewed and their predicted position on the liquidus projection.

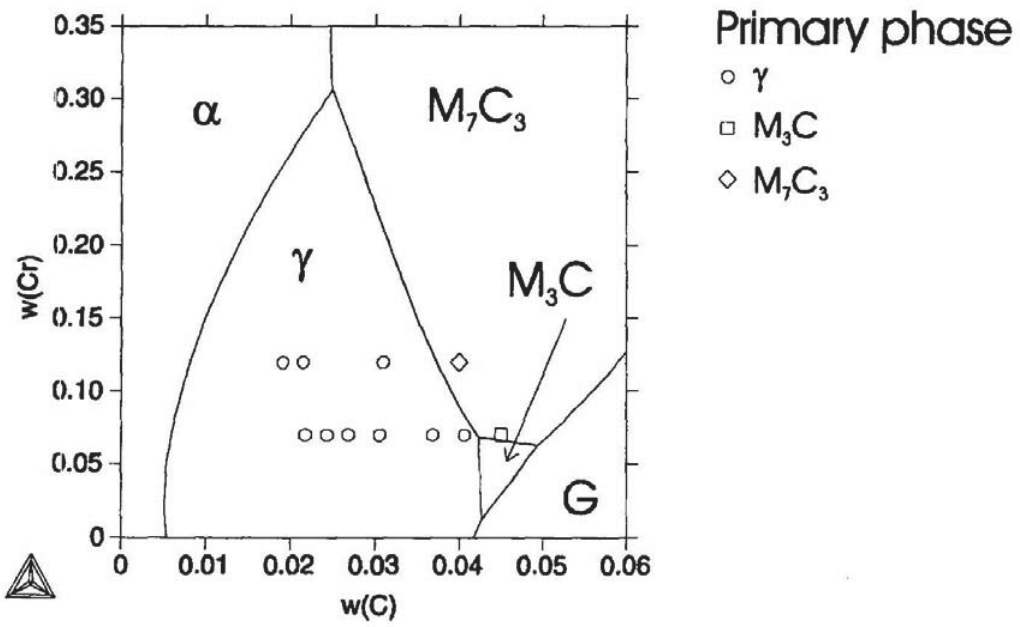

Figure 2.13: Fe-Si-Cr-C liquidus projection for 0.5 wt% Si[28].

2.2 COMPOSITES OF STEEL AND CAST IRON

Within the mining industry, quenched and tempered steels are used extensively in components that experience a high degree of abrasive wear. However, even some alloys with a bulk hardness of 400HV wear at an excessive rate when exposed to ore or rock containing quartzite, which has a hardness in the range 900 to 1280 HV[29]. Therefore in such environments use of a quenched and tempered steel may bring relatively few benefits[30]. In contrast, under low impact conditions, high chromium white irons exhibit a much higher degree of wear resistance in such environments[31]. This is due to the microstructure of these white irons containing an appreciable volume fraction of very hard (1400 to 1800 HV[29]) chromium carbides. Unfortunately, the relatively low fracture toughness of these materials means that they are only suitable for a small range of applications. As single alloys do not typically possess high wear resistance as well as high fracture toughness[32], composites of more than one alloy offer a way to obtain optimal performance of wear parts.

Alloy composites are used extensively within the mining industry and are manufactured by a variety of techniques[33-38]. For example, a method of “cast bonding” white cast

iron to steel substrates has been described by Arnold et al.[33]. In this method a melt of wear resistant alloy at 1600°C is cast onto a solid steel substrate in a foundry. Casting in vacuum, for example as described by Huggett et al.[37], produces an even better bond between wear-resisting layer and substrate but is obviously significantly more expensive. Vacuum brazing is yet another option, but requires precisely machined surfaces and a vacuum furnace[39]. In contrast, Coronado et al.[40] and Sapate and Rao.[41] described the hard-facing of a steel substrate by a variety of welding technologies. Good wear resistance was obtained. However, as Arnold et al.[33] have pointed out, hardfacing becomes prohibitively expensive for coatings of 50 mm thickness or greater. In addition, hardfacing and vacuum brazing techniques generally have a limited design scope, usually requiring flat surfaces or basic geometric shapes which require complicated fixing methods to enable effective wear protection[37].

2.2.1 – HARDFACING

Hardfacing by weld deposit is one technique that is commonly employed to apply a layer of wear resistant white iron. Hardfacing can be carried out by several welding techniques such as oxyacetylene gas welding (OAW), gas metal arc welding (GMAW), shielded metal arc welding (SMAW), submerged arc welding (SAW) and flux cored arc welding (FCAW)[34, 35, 42]. SMAW is the most commonly used technique due to the low cost of electrodes and easy application[34] although Coronado et al. found that hardfaced samples created by the FCAW process possessed higher abrasive wear resistance than those created by the SMAW process.

Chang et al.[42] found high-quality metallurgical bonding between high chromium white iron and ASTM A36 steel plate created by gas metal arc welding. They found that a thin layer had formed at the interface via epitaxial solidification with a planar growth front (Figure 4.1), which they refer to as the planar zone.

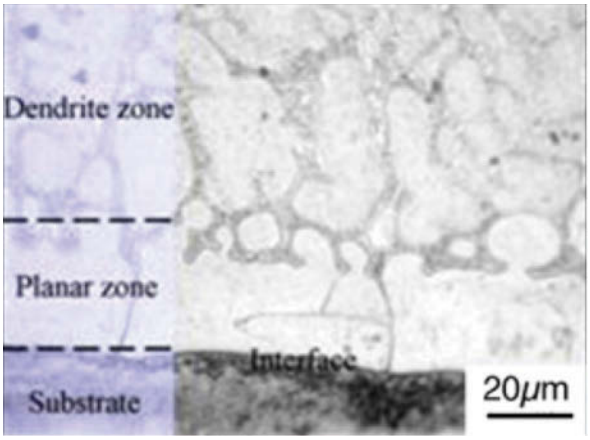

Figure 2.16: Optical micrograph of interfacial region of hardfaced alloy[42].

While hardfacing has been used successfully to join white iron to steel substrates, its main disadvantage is that it can only be used to create relatively thin layers (25-50 mm) and it cannot be used to clad complex shapes.

2.2.2 – VACUUM BRAZING

Vacuum brazing is a versatile technique that has been used as a metal joining technique since the 1950's. Vacuum brazing permits the joining of materials that could not be joined by other methods and produces strong and ductile joints.

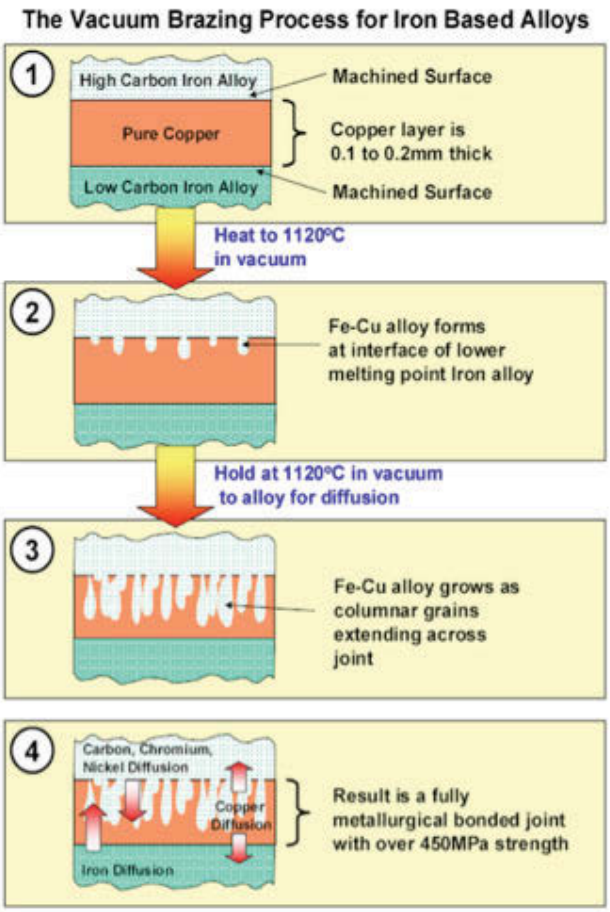

Figure 2.17: Schematic diagram for the vacuum brazing process for steel and white cast iron[43].

Brazing is a joining technique where a filler metal is heated until it is molten, and through capillary action, wets the surfaces of the materials to be joined, and solidifies upon cooling to create a strong joint.

Whilst the normal brazed joints are relatively strong compared to the parent material, there is usually no alloying of the filler metal to the parent metal, as with normal welding methods.

Inert gas brazing and, subsequently, vacuum brazing techniques, were developed to permit a wider range of materials to be joined in a more uniform and controlled manner, without the need for fluxes, which typically limit the temperatures to less than 800°C. If brazing of alloys using filler metals other than silver solder is required, then a

vacuum brazing process is the best choice due to tendency of filler alloys to oxidize and form scale at higher temperatures.

In copper brazing of ferrous alloys, the base metal (steel and white iron) dissolves into the molten copper until the iron in the molten copper reaches an equilibrium state fixed by the brazing temperature.

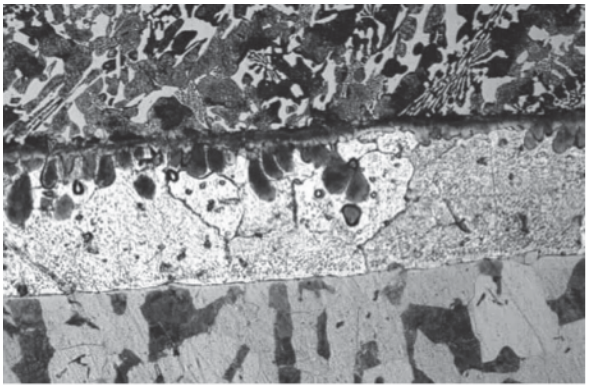

Figure 2.18: Steel/white iron composite (etchant: 5% HCl acid ferric chloride). White iron is located at the top of the micrograph with steel on the bottom with copper in the centre. Note the presence of the dissolution deposited columnar grains adjacent to the white iron/copper interface (HWOF = 470μm)[43].

Limitations associated with the vacuum brazing technique include the need for expensive heat treatment furnaces and also high tolerance machining of the surfaces as molten copper requires a gap of only 100-300μm in order to achieve a strong bond. Also the samples have to be cleaned in order for the surfaces to be wetted.

2.2.3 – CSIRO CAST BONDING PROCESS

A process called Cast-Bonding[33] has been developed by Australia's Commonwealth Scientific and Industrial Research Organisation (CSIRO) where white iron is cast directly onto steel substrates in a standard air atmosphere. The process requires the use of

fluxes coating the steel substrate to limit oxidation and improve surface wetting of the liquid alloy. The white iron is cast directly onto the steel after the steel substrate and mould are preheated to a moderate temperature of approximately 300 to 400°C. The Cast-Bond process has been successfully used to create high quality bonds between the steel and the white iron.

The cast-bonding process is an excellent alternative when compared with hardfacing for components requiring greater thickness of the hard overlay. The cast bonding process can also be used to cast complex shaped composites as opposed to the plate/block nature of the vacuum brazing process.

The main disadvantages of the CSIRO Cast-Bond process are the need to place the steel to be bonded inside a sand mould (or centrifugal casting unit if lining pipe), and establishing a method of preheating the steel within the sand mould. The steel insert will also act as a chill even if the steel is preheated and there will be a potential for shrinkage defects and other issues associated with using chills.

2.2.4 – VACUUM CASTING

The theory behind the vacuum casting process for steel/white iron composites was developed from the concept of vacuum brazing. As discussed in Section 2.3.2, vacuum brazing uses a copper shim, which is heated until liquid after which a dissolution/alloying process begins that establishes the growth of iron/copper columnar grains across the interface.

In the vacuum casting process, both the steel and white iron are be placed in the furnace and heated until the white iron is liquid. At this temperature, the white iron partially dissolves the surface of the steel creating a complex alloy and thus a metallurgical bond between the white iron and the steel substrate.

The main advantage this technique has over vacuum brazing in that a bonding agent is not required and thus sample preparation is simplified. Like the cast-bonding process, complex shapes can be cast, but vacuum casting does not require a flux, as oxidation is

limited via the use of a vacuum furnace. Also chilling is not an issue as both the white iron and the steel are heated simultaneously. The vacuum casting process would also enable the addition of other alloying elements within the one process such as tungsten carbides, which would provide additional wear resistance. The main disadvantage of vacuum casting is the need for an expensive vacuum furnace.

2.2.4 – CENTRIFUGAL BI-METAL CASTING

Bi-metallic composites created through a casting process have been around for over 40 years. In 1971[44], a patent was filed for the centrifugal casting of bi-metallic rolls. This is performed by first casting a wear resistant material in a mould spun at high rpm so that the outer surface of the casting is comprised of this alloy and then the mould is slowed and the remaining liquid metal allowed to flow out. A second alloy is then cast at a much lower rpm and a metallurgical bond is formed between the two materials. This technique is still in use today by companies such as Union Electric Steel[45] and the Åkers Group[46] and allows them to create rolls with wear and heat resistant outer layers and cores made of a tougher material. This technique has a limitation in that it is only suitable for cylindrical pieces.

2.3 THE NICHE FOR THIS PROJECT

Although vacuum casting is attractive, it does have cost implications. Therefore in my project I investigated whether a hybrid process would be feasible. In this new process, the isothermal processing of the vacuum casting method is applied, but processing is conducted *without* the need for establishing a vacuum environment.

The effect of furnace atmosphere/residual oxygen on the bond strength and degradation of the cast products could obviously be problematic and hence this

becomes a key factor to be studied in this project. When joining the white iron with the steel by casting the liquid white iron, oxides at the interface between the two materials should be avoided. Oxides will reduce the overall toughness of the composite and cause a part to fail prematurely. However, it is well worth pursuing this new approach because commercial production of composites would be considerably facilitated if a way can be found to economically produce sound composites of steel and cast iron under air and inert gas atmospheres.

Therefore, the aim of this project was to develop a joining technique that can be used to create complex shaped composites while creating these parts in an *air environment*. Work by Huggett [36, 37, 43] in the past on *vacuum* casting showed promising results but the production cost would be high relative to other established joining techniques such as welding and hardfacing. This is because using a vacuum furnace to generate these parts not only increases time spent and energy required creating each part but also requires a large capital outlay in the form of purchasing expensive vacuum furnaces.

Although the existing CSIRO-developed "cast bonding" in air is an attractive option because it provides obvious benefits in terms of throughput, capital costs and operating expenses, the quality of the interface between hard layer and the steel substrate is one of the major technical concerns in this field. A good mechanical bond between the two requires an absence of significant oxide inclusions, porosity or brittle phases on the interface, and well-developed metallurgical bonding. As I will show, I discovered early on in my own project that changing from a 'cast-on' method to an isothermal method brings an unexpected benefit in terms of interface quality. In my alternative process the melt of a wear-resisting alloy of comparatively low melting point is allowed to react *isothermally* with the steel substrate over *several minutes*. During this time some important interfacial reactions occur and these form the subject of much of my PhD. I term this isothermal process "kiln casting" in order to differentiate it from "cast bonding".

CHAPTER 3 - SELECTION OF MATERIALS

The aim of this project was to develop a joining technique that can be used to create complex shaped composites of ferrous materials by casting, with the process to be conducted in air or a protective atmosphere. Work by Huggett [36, 37, 43] in the past on vacuum casting showed promising results but to make this cast bonding technique a commercially viable alternative to other established joining techniques such as welding and hardfacing, the efficiency of production of each of these parts would need to be increased. Using a vacuum furnace to generate these parts not only increases time spent creating each part but also raises the capital costs significantly. The main reasons a vacuum furnace has been used in the past when creating these ground engaging tools (GETs) is to minimize oxide formation at the interface of these two materials (oxide inclusions along the joint between the two materials will reduce the mechanical strength) and to minimize material loss due to scaling (oxidation) of the original steel substrate.

For the purpose of this study, a white iron of the lowest practicable melting point and a steel substrate that will minimally oxidize at high temperature was desired. White iron was selected as the wear-resisting material because:

1. It has well-known resistance to abrasion and corrosion
2. It can be produced from relatively cheap raw materials
3. It has a melting point that is easily governed by carbon content

A low melting point white iron is ideal as a low casting temperature would result in energy savings, simpler processing and reduced oxidation of the substrate, regardless of the substrate material or protective coating.

The first task of this study was to define the composition of the white iron that would be used. It was decided that the low melting point white iron developed by Huggett and Ben-Nissan[27] and mentioned earlier was most suitable. This possessed a high carbide volume fraction which would aid in improving wear resistance and, being a eutectic alloy with a relatively low melting point, it would be readily castable at low

temperatures. The latter is important to minimize energy costs and minimise the oxidation of the steel substrate.

By choosing a substrate with a high scaling temperature or protecting a substrate with an oxidation resistant coating, the formation of oxides at the interface may be diminished.

The program Thermocalc[1] was used to create a series of phase diagrams for alloys ranging from 6-16% chromium, Figure 2.14. It can be seen that the liquidus decreases with decreasing chromium content. While the aim of this project is to select a low melting point white iron, eutectics with chromium levels less than 12% Cr will also form some Fe_3C upon cooling (in addition to M_7C_3). This must be avoided as it will reduce the wear resistant capabilities of the composite due to Fe_3C being lower in hardness[27].

To increase the toughness of the alloy, it is desirable for the white iron to have a matrix of austenite.

[1] Thermocalc is a product of Thermo-Calc Software AB, Norra Stationsgatan 93, Plan 5, SE-113 64 Stockholm

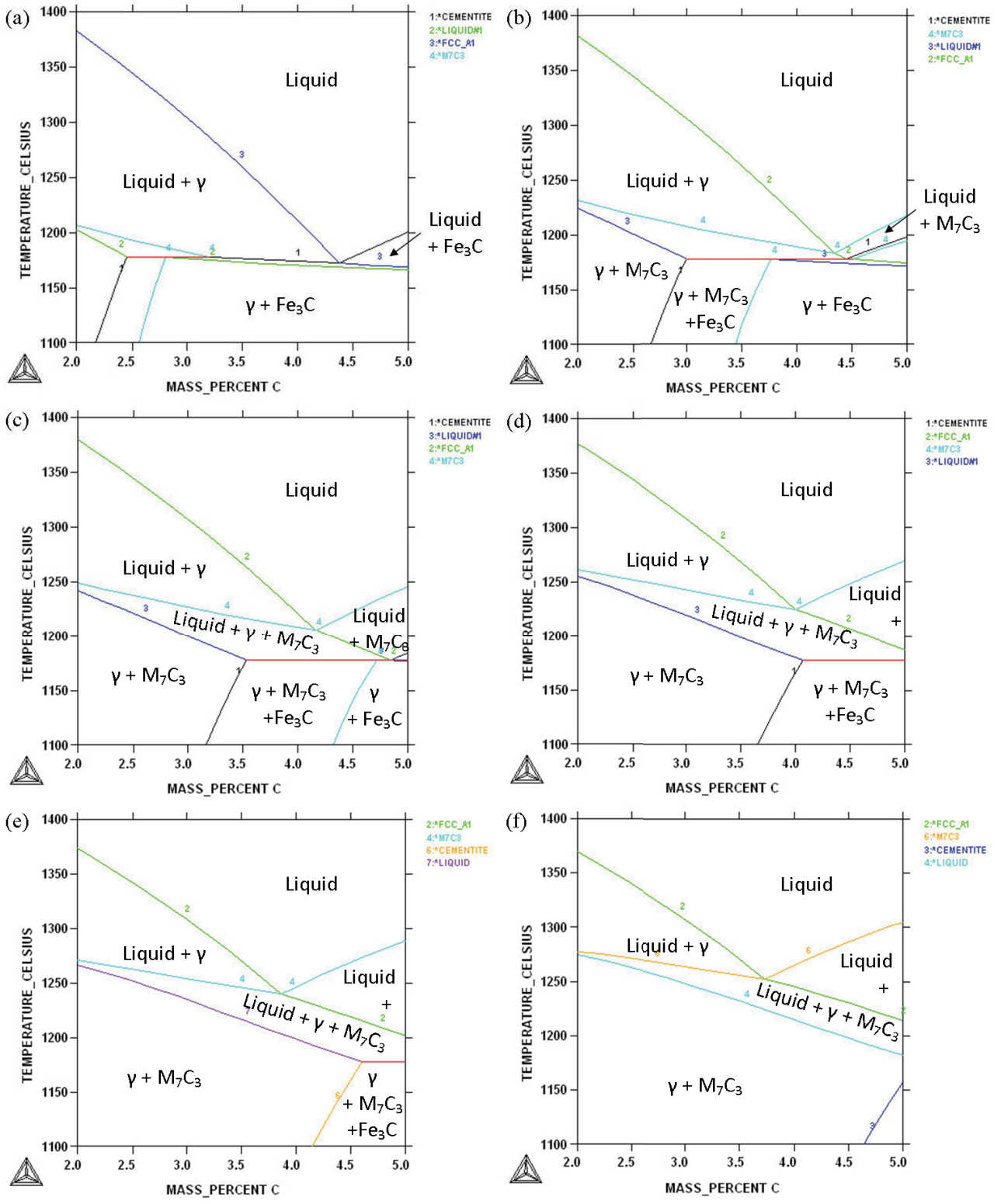

Figure 3.1: Fe-Cr-C equilibrium phase diagrams with (a) 6% Cr, (b) 8% Cr, (c) 10% Cr, (d) 12% Cr, (e) 14% Cr and (f) 16% Cr. Calculated using the ThermoCalc TCFE7 database.

These considerations confirmed that the white iron composition previously developed by Huggett et al.[27] was close to the optimum. This alloy has a nominal composition of:

Carbon = 4.1 weight %
Chromium = 12.0 weight %
Manganese = 1.6 weight %
Nickel = 1.0 weight %
Silicon = 0.5 weight %
Iron = Balance

In this study scaling of the steel substrate must be avoided. Scaling occurs when an iron oxide layer forms on the surface of the steel by the mechanism shown in Equation 3.1.

$$\text{METAL} + O_2 \rightarrow \text{METAL OXIDE} \qquad \text{EQUATION 3.1}$$

As soak temperature and time increases, the rate of scale growth will also increase. Once the scale is removed, a part with smaller dimensions results, which is undesirable. The surface finish of the part is also destroyed and subsequent grinding, dressing or other form of machining may be required to address this.

When steel is exposed to an oxidizing atmosphere, a multilayered scale forms consisting of FeO (wüstite), Fe_3O_4 (magnetite) and Fe_2O_3 (hematite) with the wüstite layer being adjacent to the steel surface, while hematite is at the gas-scale interface.

In order to calculate the rate of oxidation, either the increase of thickness Δx_{scale} of the scale layer with respect to time or mass gain, Δm_O due to oxidation with respect to time, Δt for and area A, must be known.

$$\rho_{\text{mole}} = \frac{\Delta x_{\text{scale}}}{\Delta t} = K_{S/O}\frac{\Delta m_O/\Delta t}{A} \qquad \text{EQUATION 3.2}$$

$K_{S/O}$ is the stoichiometric ratio of the scale mass per unit mass of oxygen in the scale and may be estimated from the Fe/O stoichiometry. In this layer of scale, the ratio of oxides

$FeO/Fe_4O_2/Fe_2O_3$ has been shown by Paidassi to be 95/4/1[47], and the stoichiometry Fe_yO can be approximated by y = 0.95 although Engell has shown that this atomic ratio may vary from 0.88-0.95[48].

Figure 3.1 shows a schematic of the mechanism of growth of the oxide scale layer based on Equations 1 and 2.

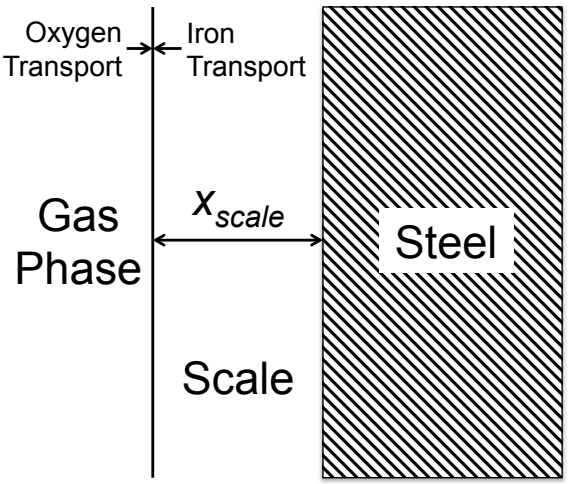

Figure 3.2: Schematic showing the formation of a layer of scale via atomic transport[49].

This chapter will provide an assessment of the techniques that may be employed to minimize the oxidation of the steel substrate during the process in which the wear resistant alloy is cast on to the substrate. Whatever solutions are found need to be compatible with the production of large scale castings.

3.1.1 – COATINGS

Coatings have been employed extensively in the past in order to minimise the oxidation of steels and other metals[50-60]. These coatings are generally of a ceramic nature with most being made through the sol-gel process, although they can also be applied by thermal processing ("flame spraying"). Many types of sol-gel coatings have been studied including zirconia[51-53, 55, 60], borosilicate[58], aluminosilicate[50] and ceria[54]. Substrates studied include stainless steels[51-53, 59, 60] and mild steel[55-57] with

most work highlighting the coatings' performance in corrosive environments. As merely one example, Li et al. [57] studied the protective effect of a zirconia sol-gel coating on a substrate of mild steel at a soak temperature of 500°C. They found that the rate of oxidation of the steel surface was retarded and that the degree of protection due to the zirconia coating depended on its thickness with six layer coatings providing the best performance. Baron and Ruiz also coated 1.25Cr-0.5Mo steel with a zirconia sol-gel coating and studied the oxidation of the steel at 700°C. They found that their coating provided a 62% reduction in oxidation when compared with the bare substrate.

There are also commercially available anti-scaling coatings such as Minimox™ by Materials Interface, Inc. and the Espon process developed by Steel Plant Specialties [61].

3.1.2 – Encapsulation

Small scale steel parts in a laboratory environment are often created or heat treated within a sealed quartz tube but this is not a viable solution for large scale parts created in the manufacturing situation. A common technique used to encapsulate steel and other types of metallic parts in order to minimise oxidation and decarburisation is wrapping in stainless steel foil[62-65]. A small piece of paper may be placed in the stainless steel envelope in order to consume the residual oxygen remaining.

3.1.3 – Inert Atmosphere

Another commonly employed technique to minimise oxidation of steel based products when performing heat treatments is to carry them out in an inert atmosphere[66-68]. Argon is a commonly used purging gas for furnaces but a mildly reducing gas could also be used.

3.1.4 – HEAT RESISTING STEELS

An alternative strategy is to use a steel that possesses intrinsic resistance to oxidation. A great deal of research has been carried out on "heat-resisting steels" dating back to the early 1900s with the discovery of Fe-Cr-Ni alloys by Guillet in 1906[69] and the original discovery of high chromium-high nickel steel's heat resistant properties in 1917-18 by Chevanard[70]. The 1950's brought the advent of 2.25Cr-1Mo T22 steel which has good creep-resistance (although not much additional oxidation resistance) and which is still used to this day in applications such as thermal power stations [8]. Heat-resisting steels were developed for applications where parts were required to maintain their strength and stability when subjected to extended periods of high temperature exposure making these steels ideal for the current application. The downside of these steels is that the alloying elements required to obtain high strength and stability are relatively expensive.

Heat-resisting steels can be divided into two main categories, ferritic and austenitic. Ferritic heat-resisting steels are actually comprised of martensitic or bainitic microstructures and are strengthened by the precipitation of secondary carbides. There are three major families of heat resisting ferritic steels with compositions 2.5, 9 and 12% Cr respectively but in general they only have a service temperature of up to 650°C[8, 71].

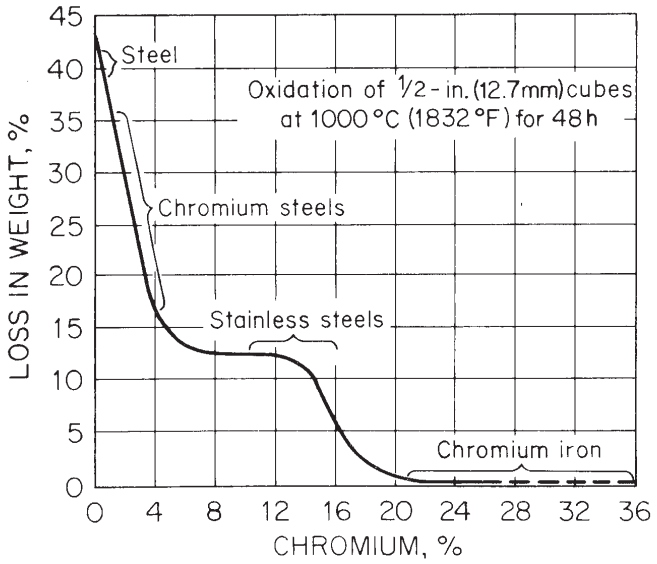

Figure 3.3: Oxidation of chromium steels at 1000°C[72].

Higher proportions of chromium increase the service temperature of the steel further as shown in Figure 3.3. Type 446 (24%Cr) stainless steel has a service temperature of 1150°C. The main disadvantage of high chromium ferritic stainless steels in the current application is their brittle nature[73, 74]. This brittleness has been shown to be caused by the precipitation of carbides and nitrides around grain boundaries[75, 76]. It has long been known that high purity, high chromium stainless steels created from electrolytic starting materials using vacuum melting techniques (thus keeping carbon and nitrogen levels below 100 ppm or so) will actually exhibit similar mechanical properties to austenitic grades of stainless steel[77, 78]. However, such processing adds hugely to the cost of the alloy and is generally regarded as impractical. In the present project white iron will be cast directly onto the steel substrate, so in this case carbon will rapidly diffuse into the steel substrate anyway. This would make a steel like type 446 even more brittle than usual and hence an unsuitable substrate material.

Austenitic heat resisting steels are generally more expensive as they possess higher proportions of expensive alloying elements such as nickel. However, due to the austenitic nature of the material, these alloys exhibit greater toughness than ferritic stainless steels. These steels are generally based on the iron-chromium-nickel system with up to 22% nickel and are employed for their heat resistance in environments above 650°C[79].

Brasunas et al.[80] showed that up to a certain level of nickel, scaling resistance is improved in austenitic stainless steels also containing up to 31% chromium, Figure 3.4. Below 20% chromium, oxidation resistance improves progressively with increasing nickel content and at higher chromium contents, optimal oxidation resistance occurs between 10 and 20% nickel. One of the best known heat resisting stainless steels is type 310, which is comprised of 24-26% chromium and 19-22% nickel which, as can be seen in Figure 3.4, make it a highly capable heat resisting stainless steel.

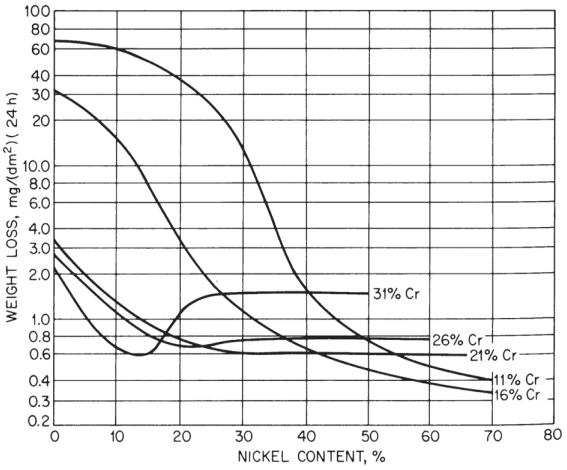

Figure 3.4: Influence of nickel on the scaling rates at 1000°C for ternary Fe-Ni-Cr alloys with chromium contents between 11 and 31%[80].

Both Nakamura[81] and Ramanathan[82] found that, with the addition of rare earth elements such as cesium, high temperature oxidation resistance is improved. Nakamura proposed that this protective effect was due to the rare earth element oxides serving as rapid nucleation sites for a passive chromium oxide layer. Ramanathan's study provided a similar hypothesis but went further saying that these rare earth elements refined the grain size and structure of this protective chromium oxide layer. In any event, the marked improvement in high temperature oxidation resistance imparted by small additions of rare earth elements led to the development of 253MA (micro alloyed) stainless steels. 253MA is comprised of 20-22% chromium and 10-12% nickel and is doped with 0.03-0.08 % cerium. This gives it heat-resisting properties similar to type 310 stainless but is much cheaper due to having approximately half the nickel content.

3.2 – Experimental

3.2.1 – Phase Diagram for White Cast Irons

The first step in characterizing the white cast iron alloy was identifying the expected microstructural constituents by studying its equilibrium phase diagram. Phase diagrams were generated using Thermo-Calc. Thermo-Calc is a software package used to perform thermodynamic and phase diagram calculations for multi-component systems. Calculations are based on thermodynamic databases produced by experimental data created using the CALPHAD method. The total volume fraction of

both the carbide and matrix phase of these alloys can be determined from these theoretically determined phase diagrams.

3.2.2 – Metallography

Scanning electron microscopy (SEM) was employed to examine the microstructure of the white iron. A Zeiss Supra 55VP scanning electron microscope was used at 20kV in conjunction with an electron backscatter detector to assess the distribution of the eutectic M_7C_3 carbides. In order to confirm the phases present in the alloy, energy dispersive spectroscopy (EDS), electron backscatter diffraction (EBSD) and X-ray diffraction (XRD) techniques were also used.

3.2.3 – Mechanical Testing

In order to understand the mechanical properties of this alloy, various techniques were used including nanoindentation and three-point bend testing. The nano indentor used in this study was a Hysitron TI 900 TriboIndenter® with a Berkovich tip. A load of 1000μN was applied for each indent for a period of 10 seconds. A Shimadzu AGS-X universal tester was used in conjunction with a compression cage in order to perform three-point bend tests on white iron rods. The white iron rods were cast from crushed alloy melted *in situ* in 4 mm inside diameter quartz tubes.

3.2.4 – Thermal Analysis

In order to confirm both the projected liquidus from Thermo-Calc as well as literature values, DTA/TGA was employed using a Thermal Analysis SDT-2960. The martensitic transformation temperature of this alloy was investigated using an electrical resistivity measurement system which has the capability to reduce the temperature of the sample down to -196°C. When the sample transitions into the martensitic phase, the crystal structure of the austenite regions change from face centred cubic to body centred tetragonal. Hence the electrical resistance of the material also changes and this can be monitored via a datalogger.

3.2.5 – Oxidation of Steel

Five separate oxidation minimization techniques were examined in this study and they are shown in Table 3.1. Lengths (5 mm) of approximately 6.5mm diameter steel rod were accurately sectioned in order to maintain similar total surface area and were subsequently polished on 800 grit paper prior to heat treatment to remove any oxide and then rinsed with ethyl alcohol. The samples were then accurately weighed and the total surface area of each sample was calculated. For samples that were coated, this was done after weighing and measurement. Type C samples were coated with 10% by volume colloidal graphite in isopropanol and allowed to dry and weighed after.

Type B samples were protected by high purity (99.997%) argon gas and the atmosphere was controlled by a positive pressure in the chamber during the heating cycle.

Type D samples were coated by an Espon HF (See 3.1.1), a commercial anti-scale coating and allowed to dry for 24 hours. This coating's composition is proprietary and comes in the form of a liquid paste that is painted onto the sample.

Table 3.1: Test samples heated to 1250°C for soak times varying from ten minutes to two hours.

Sample Name	Sample Type
A	Mild steel
B	Mild steel in argon atmosphere
C	Mild steel coated in colloidal graphite
D	Commercial anti-scaling agent
E	Type 310 austenitic stainless steel
F	253MA austenitic stainless steel

Samples were then placed in small, 30mm diameter, alumina crucibles in an electric muffle furnace held at 1250°C. Soak times of from ten minutes to two hours were applied.

When each sample was removed from the furnace, it was allowed to cool and the sample and any scale sitting at the bottom of the crucible was then weighed. The weight gain due to oxidation was then recorded and the five techniques were compared against those of the untreated mild steel.

3.2.6 – Three-Point Bend Testing

In order to assess the mechanical properties of each steel (and hence its suitability as a substrate for the white cast iron), three-point bend testing was carried out on each steel. From the load versus displacement curves, the flexural stress and strain along with the flexural modulus of the steel sample may be calculated.

The maximum flexural stress is calculated by the following equation:

$$\sigma_f = \frac{PL}{\pi R^3} \qquad \text{Equation 3.3}$$

Where P is the load, L is the span length and R is the radius of the test specimen. To calculate the maximum flexural strain the following equation:

$$\epsilon_f = \frac{6Dd}{L^2} \qquad \text{Equation 3.4}$$

where D is the deflection of the beam and d is the diameter of the beam.

3.3 – Results and Discussion

3.3.1 – Characteristics of the white cast iron

The basis on which the particular wear-resistant white iron used was selected was discussed at the start of this chapter. However, I still considered it necessary to confirm its key attributes. In order to theoretically verify the melting point quoted[27], Thermocalc was used to create an equilibrium phase diagram for the alloy in question, Figure 3.5(a).

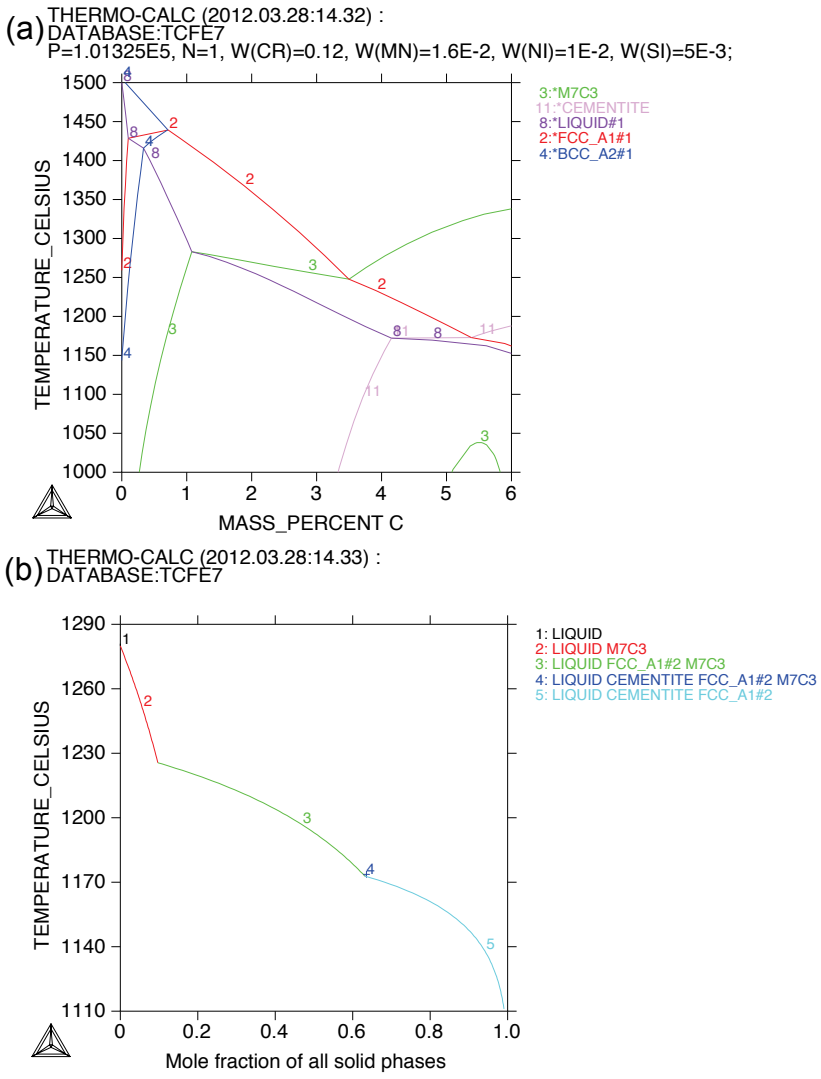

Figure 3.5: (a) Equilibrium phase diagram of Fe-12Cr-1.6Mn-1Ni-0.5Si-4.1C alloy. (b) Scheil diagram showing the solidification path of this alloy.

From both the phase diagram and Scheil diagram shown in Figure 3.5, it can be seen that Thermocalc predicts an alloy with Fe-12Cr-1.6Mn-1Ni-0.5Si-4.1C will form a slightly hypereutectic microstructure upon solidification. Actually, this alloy has been shown to be eutectic in nature[27] and hence will solidify with a microstructure of liquid + austenite + M_7C_3 upon cooling below the liquidus. As the alloy cools further to the point where approximately 75% of the alloy has solidified in the form of austenite + M_7C_3, then cementite + austenite forms.

Using an SEM with a Rutherford backscatter detector, it can be seen that the microstructure of the alloy shown in Figure 3.6 has a eutectic-like form. Based on the findings of the previous section, this alloy should produce a eutectic microstructure of austenite and M_7C_3 carbides surrounded by cementite.

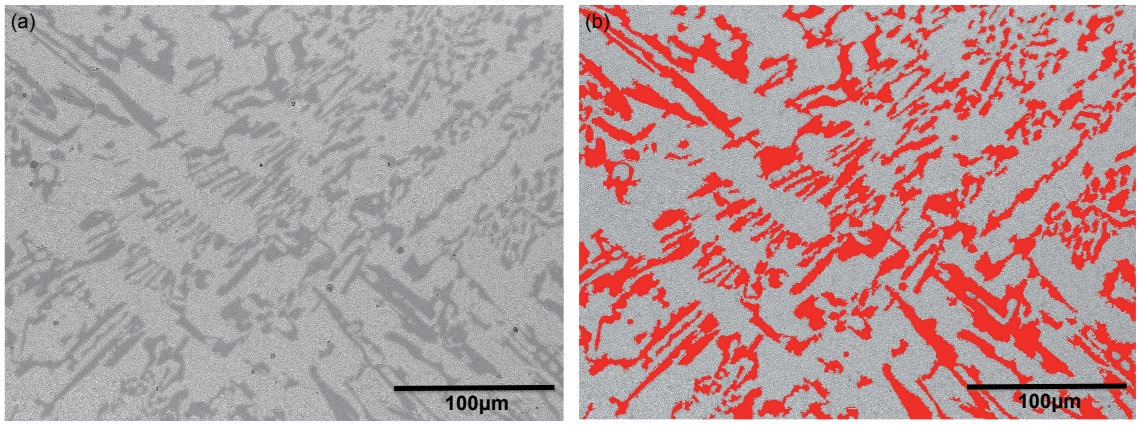

Figure 3.6: (a) Typical eutectic microstructure of Fe-12Cr-4.1C-1.6Mn-1.0Ni-0.5Si. (b) Overlay indicating the location of carbides (red) in the white iron. (HWOF = 348µm)

The micrograph and the carbide overlay shown in Figure 3.6 shows the microstructure of the as-cast alloy. By applying ImageJ software to the overlay we can calculate the carbide volume fraction (CVF) of eutectic carbides to be approximately 29 percent.

Data gathered from Thermocalc's predicted phase formation during the solidification of this alloy showed that approximately M_7C_3 carbides occupied 36 vol% upon solidification but upon cooling, this figure decreased to approximately 21 vol% due to the decomposition of these carbides into M_3C. This variation between theoretical carbide content and the experimentally observed results can be explained by the fact

that the theoretical calculations are carried out under equilibrium conditions while a quite rapid cooling cycle was employed in the real tests.

To confirm the phases present in the sample, XRD was used. From the intensity vs 2theta graphs shown in Figure 3.8 it can be seen that the as-cast sample is comprised of austenite and M_7C_3 carbides, with small traces of ferrite and cementite.

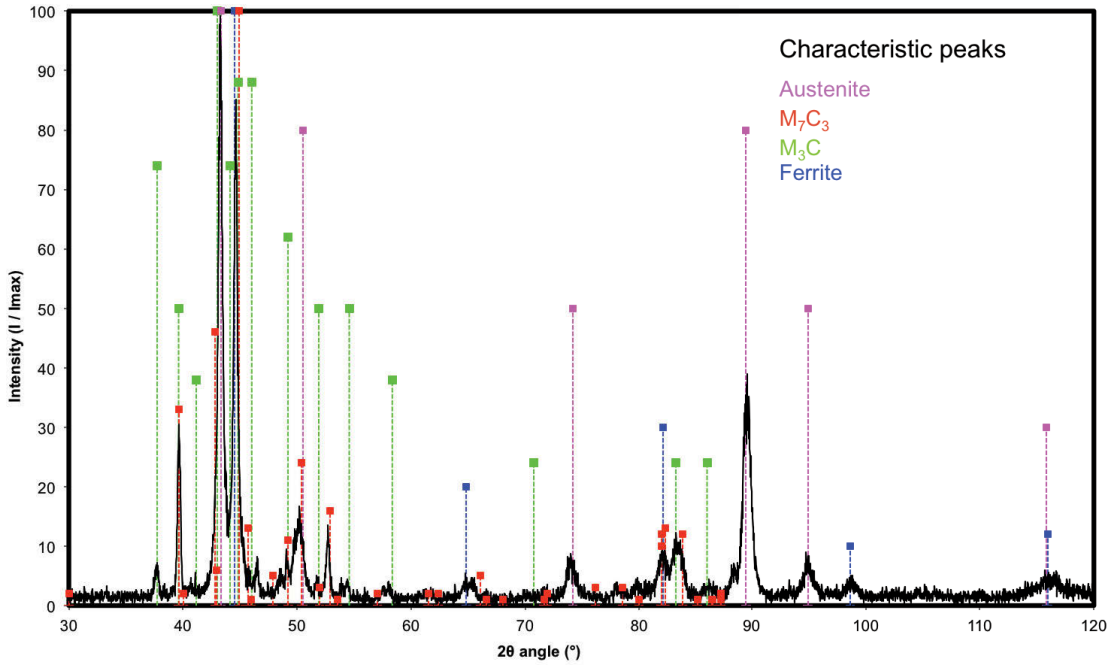

Figure 3.8: XRD pattern of as cast white iron created under typical casting conditions.

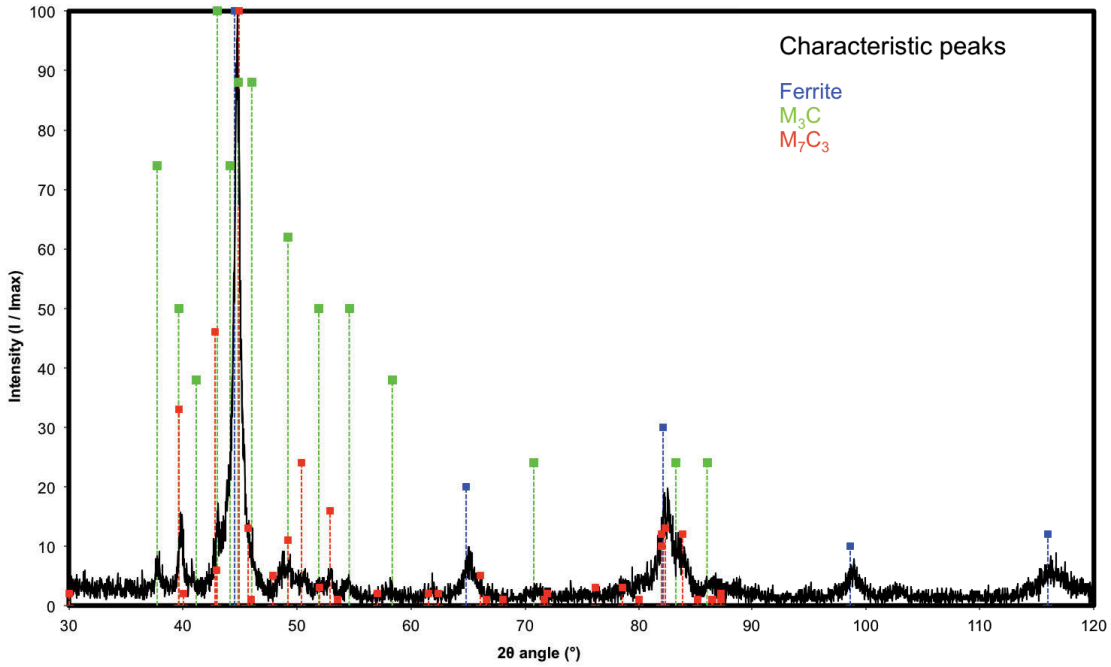

Figure 3.9: XRD pattern of as cast white iron cooled slowly.

This alloy may also form an undesirable microstructure of ferrite + cementite + M_7C_3 if the cooling of the alloy from liquid is carried out over a long period of time. While the Scheil diagram in Figure 3.5 shows no formation of ferrite, the phase diagram indicates a transformation to ferrite + cementite + M_7C_3 between 500-750°C. This is a highly undesirable microstructure as it will result in a reduction in toughness of the matrix, as well as reduction in hardness of the reinforcement phase (M_7C_3 is much harder than M_3C). Figure 3.9 shows the XRD patterns of cast samples of this alloy after extremely slow cooling. It can be seen that only a small quantity of the M_7C_3 carbides is retained with most being transformed into cementite, while the matrix has been transformed into ferrite. From the micrographs shown in Figure 3.10 it can be seen that these XRD results are confirmed with large regions of ferrite and cementite forming pearlite as shown in Figure 3.10(b) & (c).

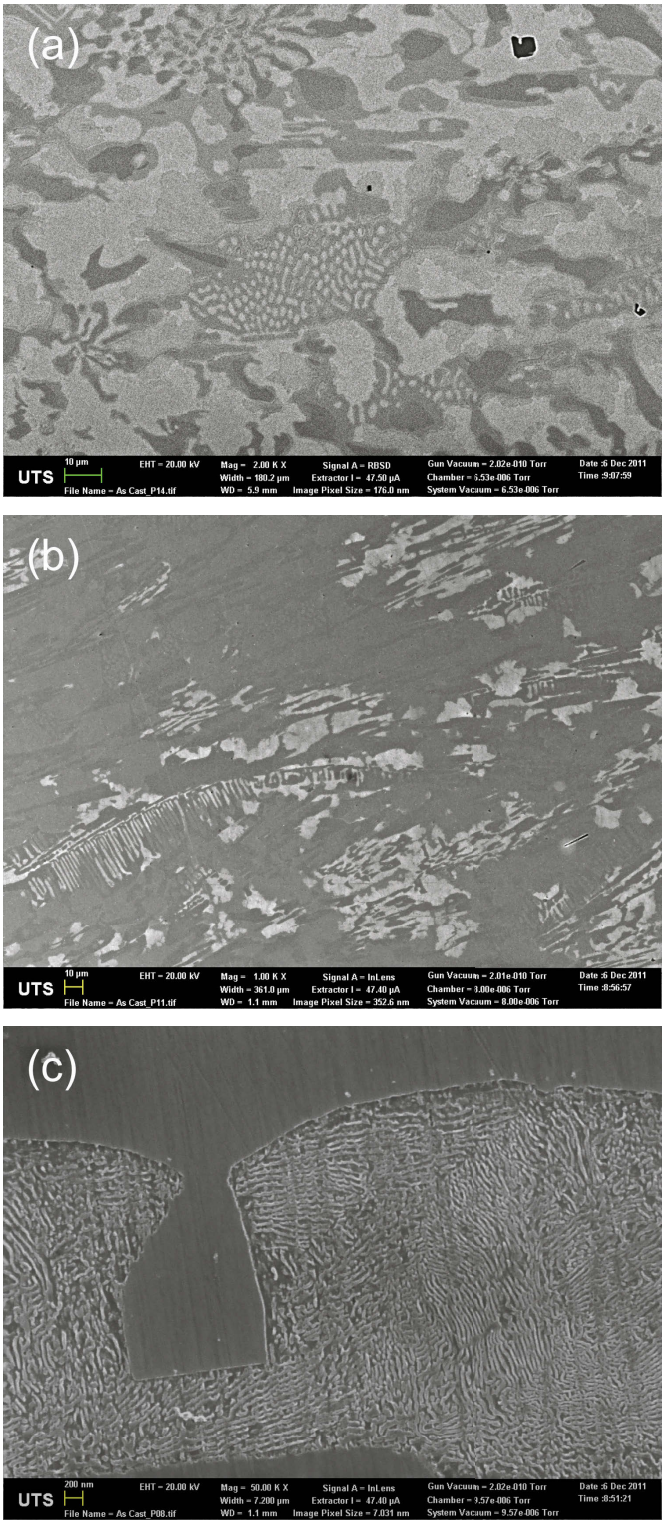

Figure 3.10: (a) Backscattered electron micrograph of as cast microstructure. Lightest phase is ferrite, darker phase is cementite and darkest phase is M7C3. (HWOF = 180µm) (b) In-lens detector micrograph with lightest phase indicating the location of localized pearlite. (HWOF = 360µm) (c) High magnification micrograph of pearlite grain. (HWOF = 7.6µm)

Care must be taken to ensure optimal microstructure is achieved. It was found that a cooling rate of approximately 15°C/min produced a satisfactory microstructure of austenite + M_7C_3 + small quantities of M_3C.

TABLE 3.2. COMPOSITION OF AUSTENITE, FERRITE AND M_7C_3 CARBIDES IN MICROSTRUCTURE PRODUCED BY 25 MINUTE SOAK AT 1250°C. ALL COMPOSITIONS ARE QUOTED IN MASS PERCENT. MEASUREMENTS WERE MADE USING WDS FOR CARBON AND EDS FOR ALL OTHER ELEMENTS.

Phase	Fe	Cr	C	Ni	Mn	Si
Ferrite	98.1	0.1	0.3	0.5	0.3	0.2
Austenite	90.2	5.5	0.6	1.5	1.3	0.7
M_7C_3	60.6	28.0	8.6	0.6	1.7	0.2

A rough idea of the martensite start temperature (M_s) in a range of ferrous alloys may be gained from a usage of Andrew's equation[83], Equation 3.6, and the composition of the austenite phase shown in Table 3.2. This indicates that the M_s should be approximately 150°C, well above room temperature, which clearly contradicts the XRD results shown in Figure 3.8.

$$M_S(°C) = 539 - 423C - 30.4Mn - 17.7Ni - 12.1Cr - 7.5Mo \qquad \text{EQUATION 3.6}$$

In order to prove the retention of austenite at room temperature, a sample was placed in a bath of liquid nitrogen and then re-examined at room temperature. A micrograph of the subsequent microstructure is shown in Figure 3.11. Raised laths of martensite can be seen protruding from the sample surface, particularly around the carbides, indicating a phase change. (The surface distortion is due to the transformation of the FCC austenite into the body centered tetragonal (BCT) martensitic crystal structure.)

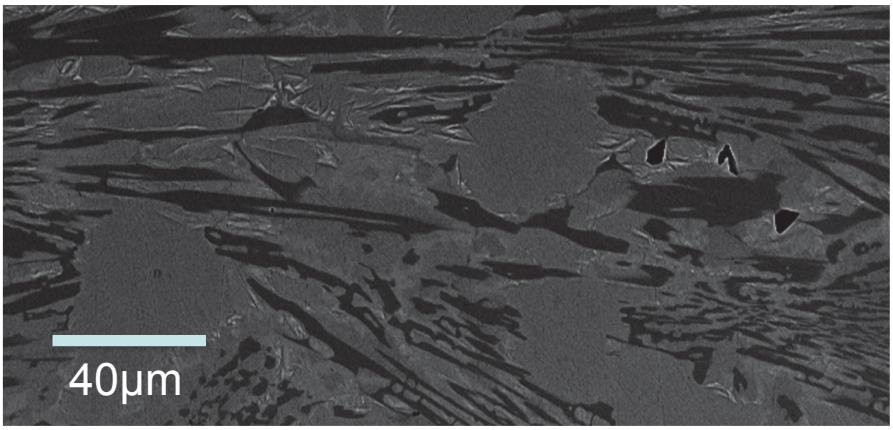

Figure 3.11: Backscattered electron image of microstructure after plunging into liquid nitrogen. The surface of the metal matrix is rough, especially around the carbides due to the transformation of austenite to martensite. (HWOF = 224µm)

In order to accurately determine the martensitic transformation range of this alloy, a two- point electrical resistivity test was taken on a sample of this alloy and the sample was cooled from room temperature to 130K or -143°C. These results are shown in Figure 2.22.

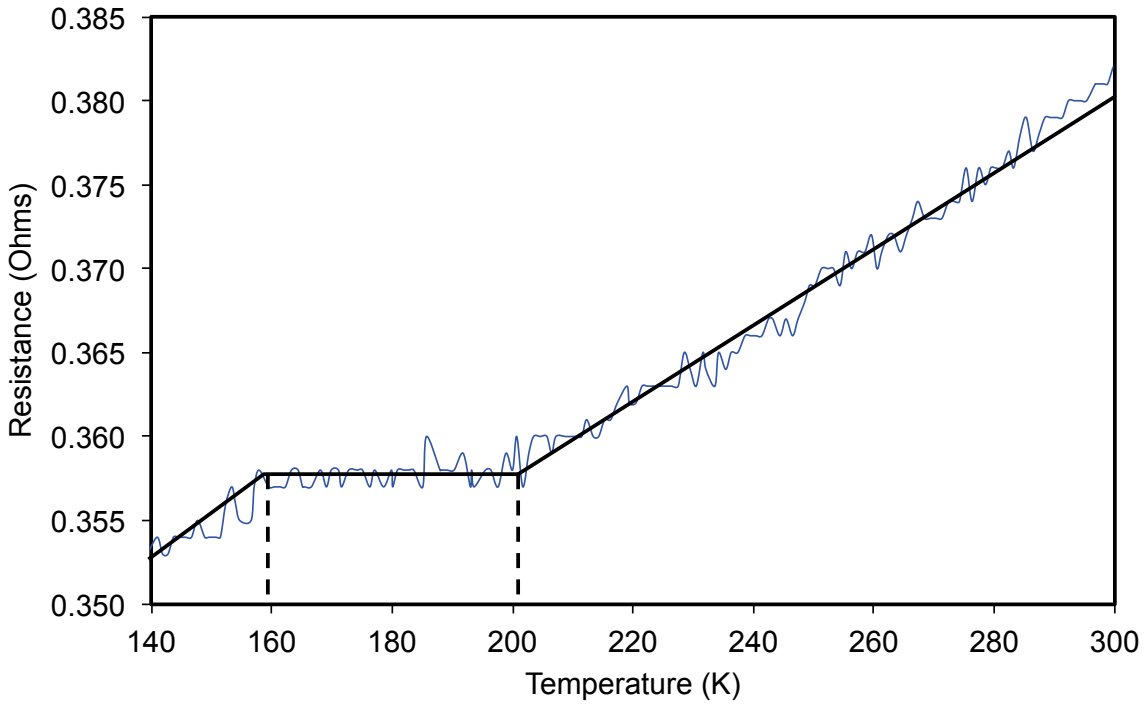

Figure 3.12: Electrical resistance of low melting point WCI alloy as a function of decreasing temperature.

From Figure 3.12, it can be seen that as the sample cools from room temperature the electrical resistance of the material decreases in a linear fashion. At approximately 200K or -73°C, the resistance plateaus until approximately 160K or -113°C where it continues to decrease again. This result clearly shows a transformation that has had a considerable effect on the electrical resistivity of the metal with the effect beginning at 200K (the martensitic start temperature) and finishes at 160K (the martensitic finish or M_f temperature).

These results confirm the data gathered via XRD and show that Andrews equation is not suitable for predicting the martensitic transformation temperature of this alloy.

A nano-indentation profile was taken across part of a polished section through the sample, as shown in Figure 3.13.

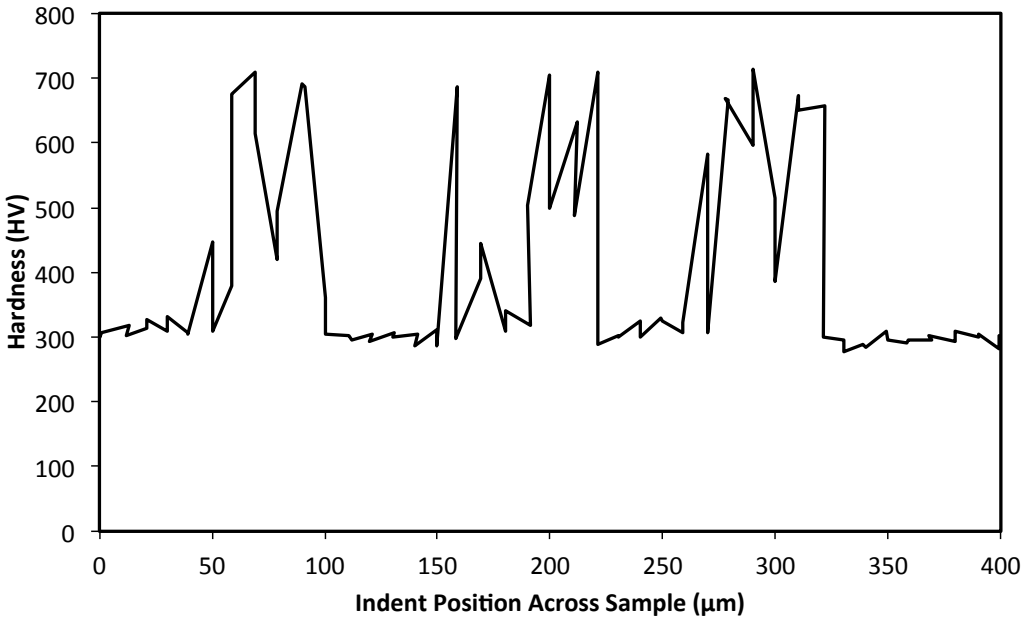

Figure 3.13: Comparative hardness profile of as cast sample from nanoindentation.

From this nano-indentation hardness profile it can be seen that the hardness increases dramatically from the austenite to the M_7C_3 carbides.

Three-point bend testing was applied to gain some information on the stiffness and also maximum flexural stress that may be applied to the material before it fractures. The decision to use three-point bend testing over other mechanical testing methods was due to a similarity between the loading the sample will undergo and that of a composite ground engaging tool made under the kiln casting process.

Under three point loading, flexural stress may be calculated using the following formula:

$$\sigma_f = \frac{PL}{\pi R^3} \qquad \text{EQUATION 3.7}$$

where P is the load at the particular point in the load vs displacement curve, L is the length of the span and R is the radius of the cylindrical test specimen.

From the flexural stress vs displacement curve shown in Figure 3.14 it can be seen that the maximum flexural stress that can be placed on a rod of Fe-12Cr-4.1C-1.6Mn-1.0Ni-0.5Si is approximately 700-800 MPa. The flexural strain, which is the strain on the outer

surface of the sample was calculated to be between 0.0218-0.022 mm/mm and the flexural modulus of elasticity ranged between 19 and 20 GPa.

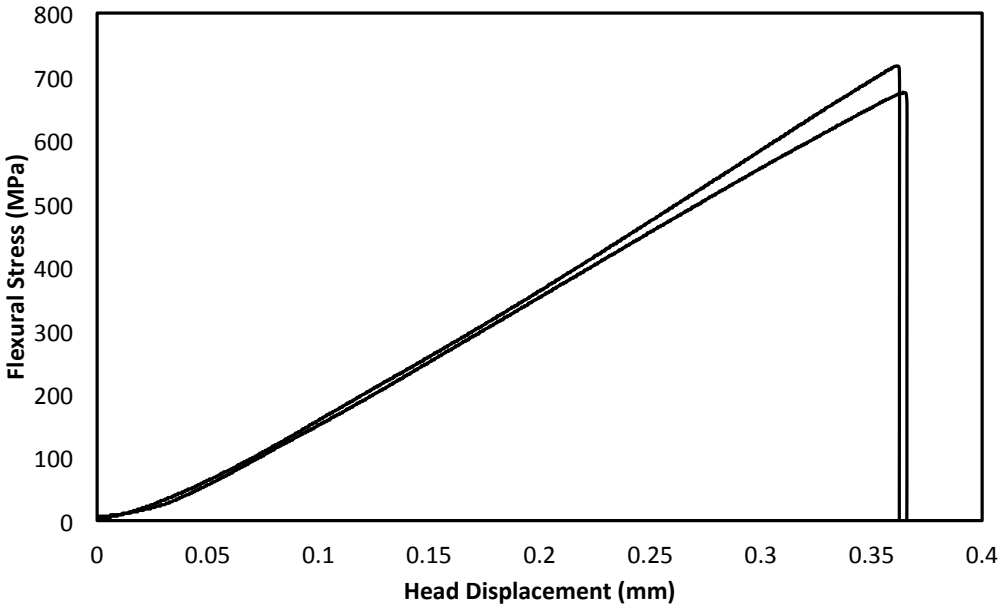

Figure 3.14: 3-point bend test flexural stress vs displacement curve.

The white iron pins failed suddenly without undergoing any plastic deformation as can be seen by the sharp drop in flexural stress when the sample cracked. This is typical of a sample that is brittle in nature. The fracture surface of one of these samples is shown in Figure 3.15.

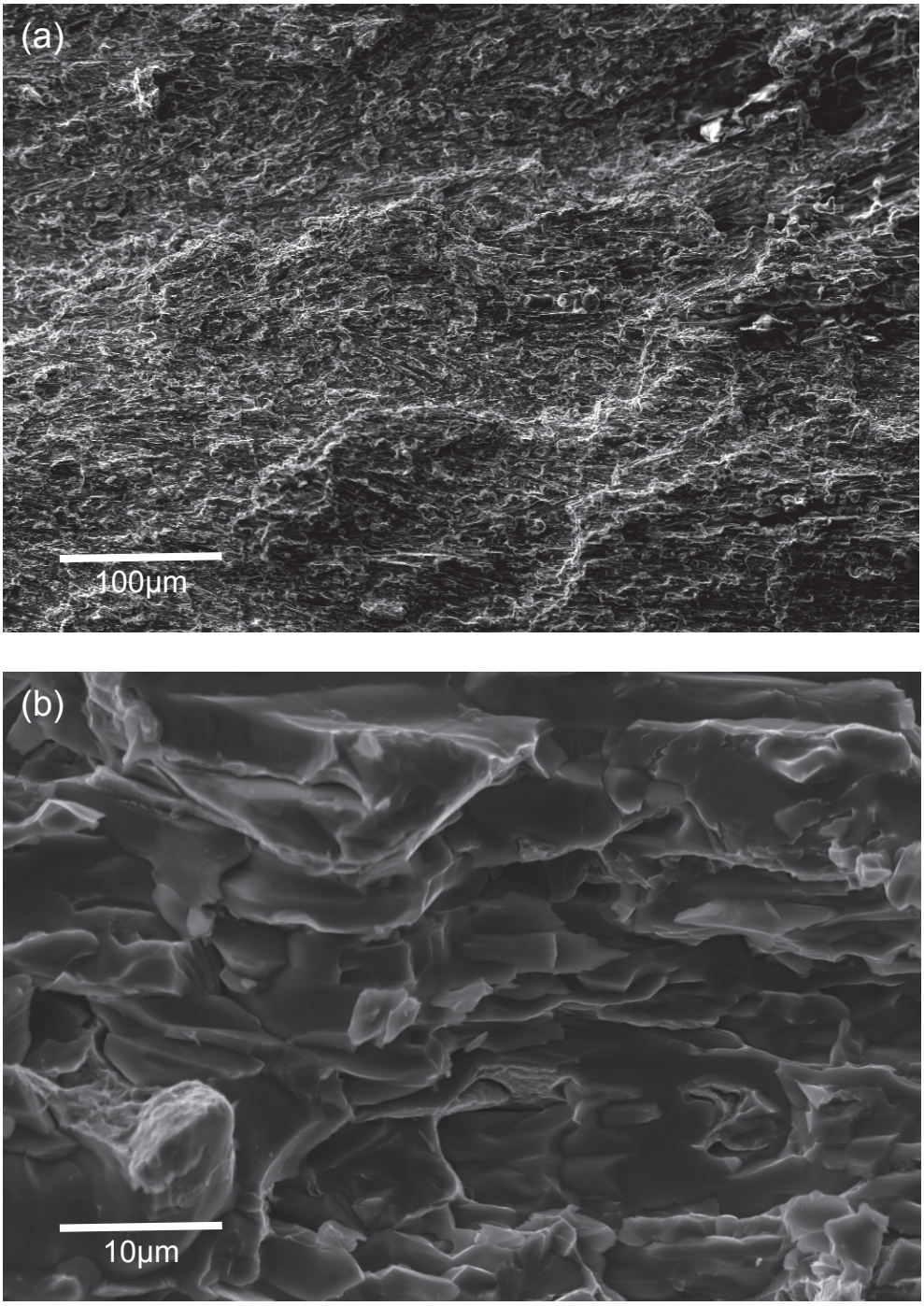

Figure 3.15: (a) Fracture surface of white iron after 3-point test. (HWOF = 600µm) (b) shows the brittle fracture surface of this material. (HWOF = 60µm)

From the micrographs shown in Figure 3.12 it can be seen that the fracture surface of this three-point bend test specimen consists for the most part of transgranular cracking, particularly through eutectic M_7C_3 carbide particles. The backscattered electron micrograph shown in Figure 3.15(a) shows highly angular facets. These appear as flat

surfaces in the SEM micrograph shown in Figure 3.15(b). This faceted texture is due to fracture along differently oriented cleavage planes within the grains.

3.3.2 – OXIDATION OF THE CAST IRON AND SUBSTRATE MATERIALS

Oxidation resistance of the white cast iron was determined in a TA Instruments SDT 2960 simultaneous DSC-TGA. The mass vs temperature curve shown in Figure 3.16 shows the increase in mass of this low melting point alloys due to oxidation of the sample. It can be seen that the rate of oxidation increases rapidly after approximately 1150°C. This corresponds with the melting of the sample as predicted in Figure 3.5. (The Thermocalc calculation predicted that the sample would transform into liquid + austenite + M_7C_3 at 1176°C and be completely molten at 1220°C.) In the actual experiment it seems likely that by 1220°C the sample had become liquid and had broken through its outer oxide layer and rapid oxidation had ensued. This test reconfirms the relatively low melting point of this alloy and also supports the theoretical calculations made using Thermocalc.

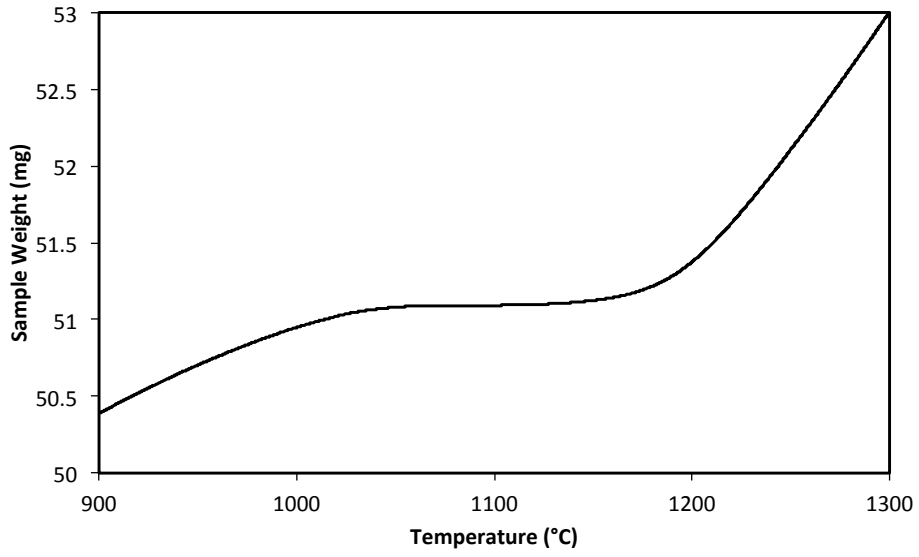

Figure 3.16: Mass vs temperature curve of low melting point white iron generated using thermogravimetric analysis (TGA).

Now that the soak temperature has been minimised due to the selection of a low melting point white iron, the performance of possible steel substrates must be analysed under these conditions.

The weight gain of the mild steel coupons due to oxidation is shown in Figure 3.17 with respect to soak time and it can be seen that mild steel oxidizes rapidly when subjected to high temperatures.

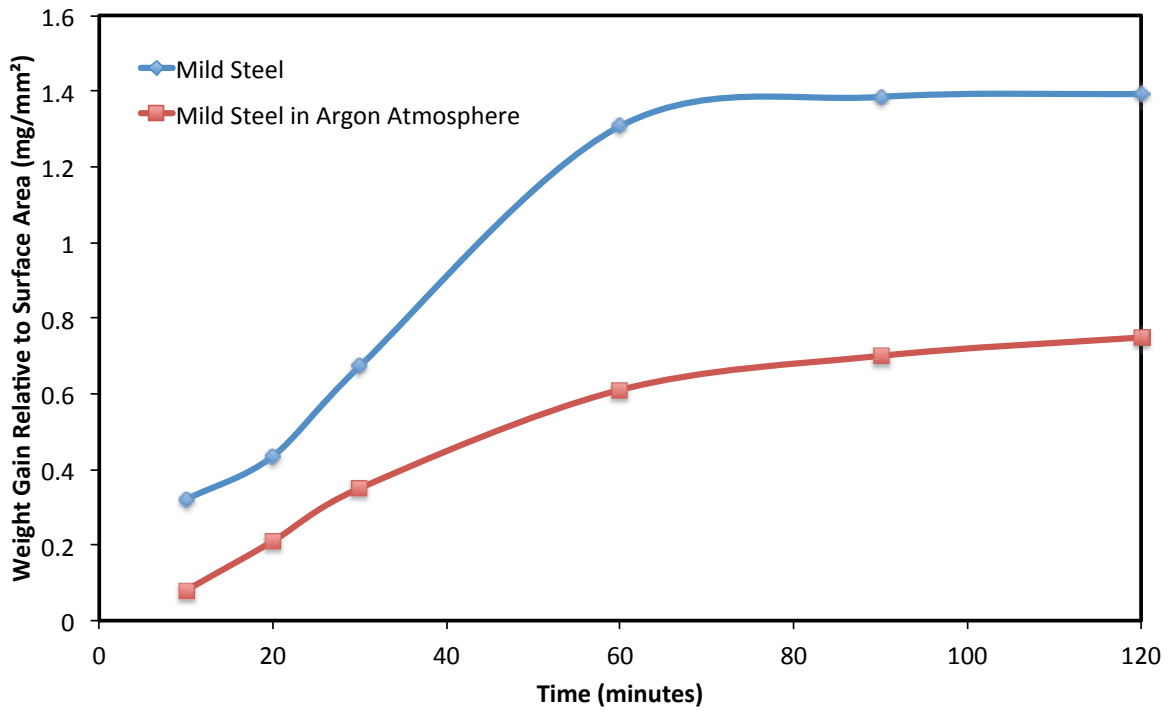

Figure 3.17: Weight gain due to oxidation at 1250°C of mild steel as a function of the soak time.

Figure 3.17 also shows the effect of an inert atmosphere, ostensibly of pure argon, on the rate of oxidation of the steel. After 10 minutes at 1250°C, the rate of oxidation has been cut to under a third of that in a standard air atmosphere. The difference between the extent of oxidation decreased as the soak time decreased but this may be accounted for by the fact that the oven door was opened to remove the samples and hence oxygen was introduced into the furnace. Note that the cylinder argon used contains ten ppm or more of oxygen and even this small amount will react rapidly with the steel at these temperatures.

When the sample oxidised, the outer layer of the steel sample was decarburised and a thin layer of scale formed as shown in Figure 3.18. With increasing soak time the thickness of the scale layer increases and hence the weight increases.

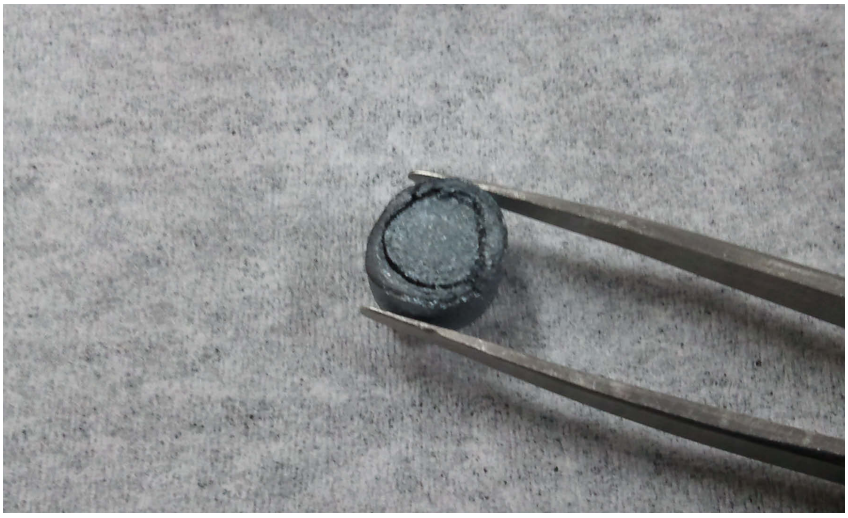

Figure 3.18: Mild steel sample oxidised at 1250°C for 30 minutes.

Figure 3.19 shows the rate of oxidation of a sample coated in colloidal graphite compared with the oxidation of uncoated mild steel. It can be seen that the colloidal graphite has had very little effect on the oxidation resistance of the substrate with heat treatments over 1 hour in length but does provide a slight improvement in the oxidation resistance of the steel with heat treatments of 30 minutes or less.

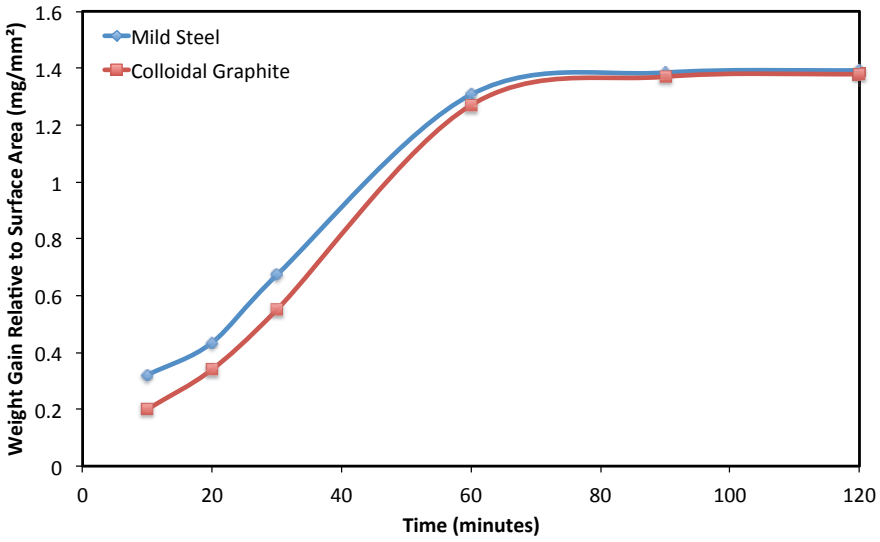

Figure 3.19: Comparison of the oxidation rate of mild steel and mild steel coated in colloidal graphite.

In contrast, the commercially available anti-scaling coating seemingly performed very well. Although some of the coating flaked off after cooling, small amounts of it remained on the sample. In a production environment this remaining coating could be removed by wire brushing or sand blasting, however, this was not considered viable for the small samples generated in the course of my project.

What can be gathered from these oxidation heat treatments is that samples coated in Espon HF exhibited very little visible oxidation. Figure 3.20 shows two of the samples after 30 minutes and an hour of heat treatment and it can be seen that a lot of the reflective nature of the steel still remains. The samples have lightly oxidised as it can be seen that the surface is slightly discoloured but this is slight in comparison with even the heat resistant stainless steels shown in Figure 3.22.

Figure 3.20: Samples coated in Espon HF after 30 mins (left) and 1 hour (right) heat-treatment.

Next, the oxidation resistance of alternative substrate materials was examined. Figure 3.21 shows a graph of the weight gain of both type 310 and 253MA steel with respect to the soak time of each sample. It can be seen that the type 310 stainless steel exhibited less oxidation at all soak times when compared with the 253MA. Both stainless steels seemed to reach a maximum degree of oxidation with the type 310 stainless steel reaching is maximum degree of oxidation after approximately 20 minutes and 253MA after 1.5 hours. Thereafter, both steels were protected by a layer of chromium oxide. This layer slows the diffusion of oxygen into the steel thus limiting the extent to which the steel can oxidize. Evidently, the nickel aids in the strength of adhesion between the oxide layer and the steel confirming work showing nickel increases the spalling resistance of steels[84].

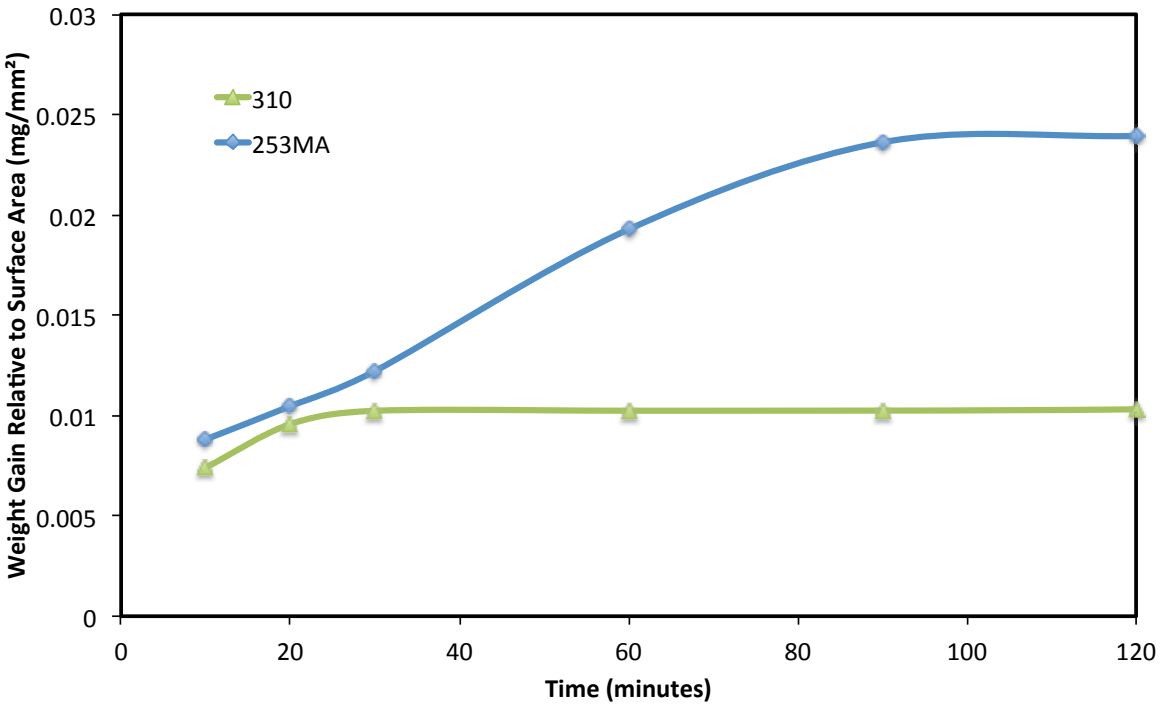

Figure 3.21: Weight gain due to oxidation at 1250°C of 253MA and type 310 stainless steels as a function of the soak time. (Note the vertical scale has been expanded when compared with the preceding figure.)

253MA stainless steel possesses almost half the nickel of type 310 and, perhaps not surprisingly, the adhesion of the oxide to steel is decreased as can be seen in Figure 3.7. A lot of the oxide scale has fallen off the sample during heating and can be seen in the bottom of the crucible in Figure 3.22(a). The quantity of oxide that had fallen off the sample increased with increasing soak time from $1.6*10^{-3}mg/mm^2$ of scale after 10 minutes to $2.8*10^{-2}mg/mm^2$ after 2 hours. The crucibles containing the type 310 stainless steel samples possessed far less discharged scale with none present after 10 minutes and only $1.5*10^{-3}mg/mm^2$ after 2 hours.

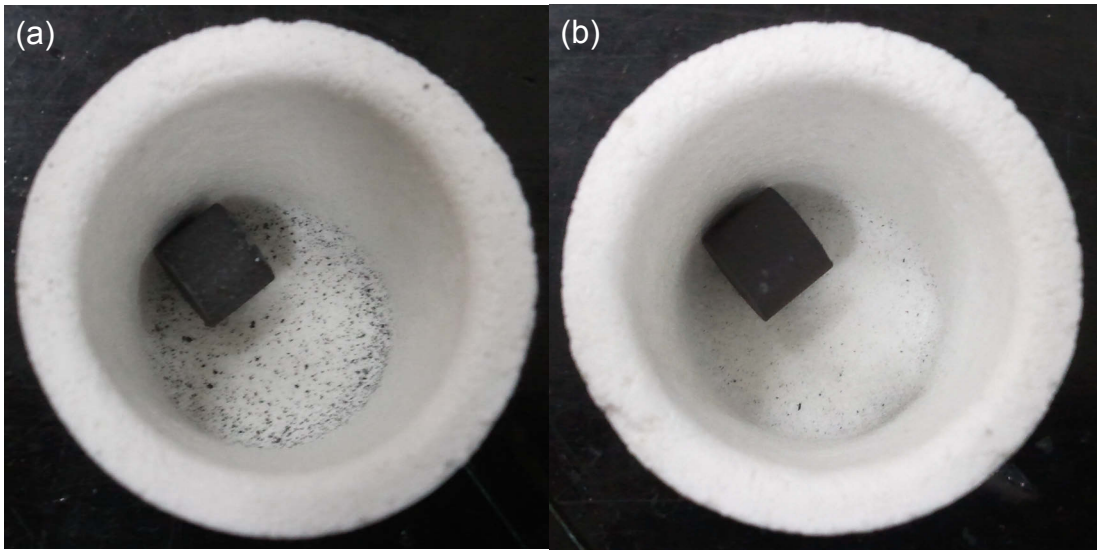

Figure 3.22: Steel samples in alumina crucibles after heat treatment. (a) shows the result of a 253MA sample after a 30 minute soak time. It can be seen that a lot of oxide can be seen in the bottom of the crucible while this occurred to a much lesser extent with the type 310 stainless steel sample (b).

3.3.1 – MECHANICAL PROPERTIES OF CANDIDATE SUBSTRATE MATERIALS

In order to assess the suitability of each steel in terms of their mechanical properties, three-point bend tests were applied. The results for these tests are shown in Figure 3.23 and it can be seen that the type 310 stainless steel possesses a greater flexural strength than that of both mild steel and 253MA. However, all three steels possess adequate strength for the proposed composite wear parts.

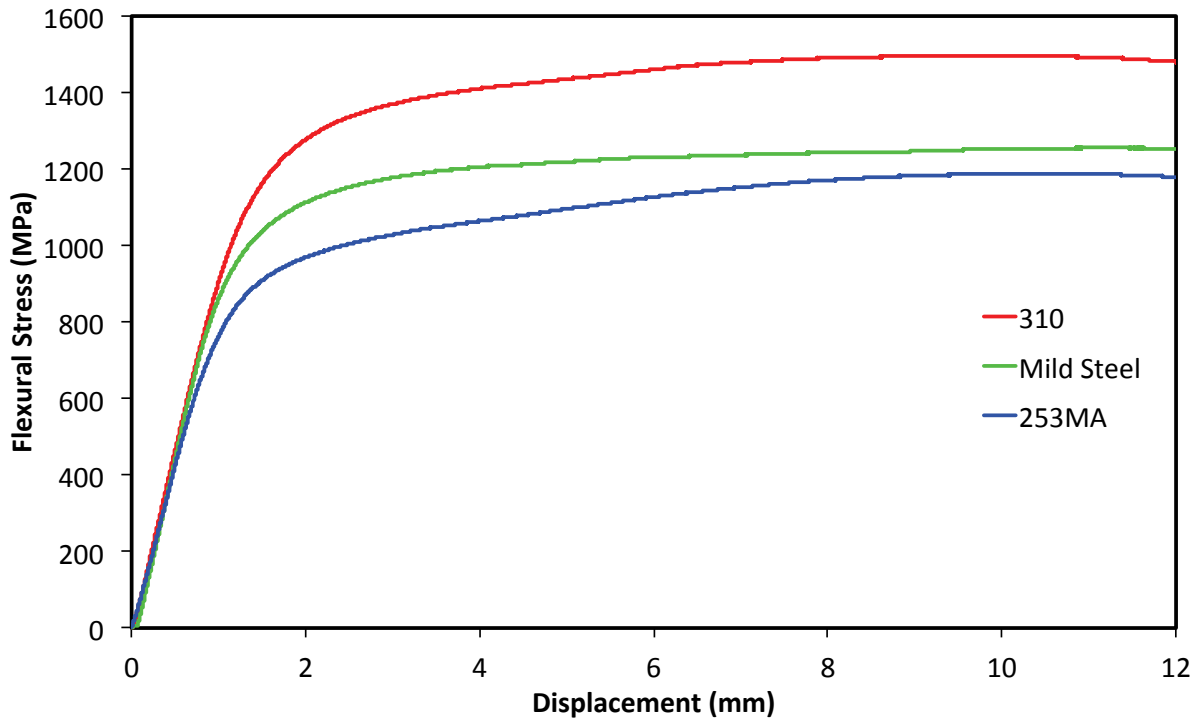

Figure 3.23: Flexural stress versus displacement curves for various steels.

3.4 – Chapter Conclusion

From the work shown in this chapter, and the background information in Chapter 2, it can be seen that the white iron chosen should be a suitable choice for making wear-resistant composite items. However, its inherent low fracture toughness restricts its usage as the sole material in parts experiencing high impact so it is necessary to back it with a substrate made of a tougher structural material.

The wear-resisting alloy chosen in this thesis is a low melting point (M.P. = 1209°C) white iron developed by Huggett and Ben-Nissan[27]. This alloy was chosen because (1) it possesses a relatively high volume fraction of carbides (CVF = 29%), (2) it melts at a relatively low temperature and is hence cheaper to cast; and (3) its lower melting point ensures that the extent of associated oxidation of the steel substrate will be reduced.

It was found that oxidation of the steel substrate during kiln casting could be minimized by either applying a protective coating, or by changing the substrate alloy. For example, the oxidation resistance of both type 310 and 253MA is much greater than that of mild

steel. However, performing the casting in an inert atmosphere of argon did not reduce the oxidation of mild steel much, due probably to the presence of oxygen impurities.

Type 310 stainless steel exhibited better oxidation resistance than the 253MA stainless steel as well as higher maximum flexural stress. Mild steel exhibited slightly lower mechanical properties than type 310 stainless steel but due to its much lower cost and the possibility of protecting it via coatings or inert atmosphere, it is a more enticing prospect for substrate material.

Key to the production of such composites will be the interface between the two types of material. This point will be investigated in further chapters of this thesis.

CHAPTER 4 – CASTING WHITE IRON ONTO STAINLESS STEEL

4.1 – INTRODUCTION

In previous chapters, the grade of cast iron to be used was identified, and some strategies for minimizing the oxidation of the substrate identified. In this chapter I pursue one of those strategies : the use of heat resisting, austenitic stainless steels as substrate. As mentioned in Chapter 3.1.4, one of the best known heat resisting stainless steels is type 310 which is comprised of 24-26% chromium and 19-22% nickel. This is an expensive, but highly capable choice for oxidation resistance.

Alternatively, it has been found that high temperature oxidation resistance of stainless steel is also improved by the addition of rare earth elements such as cerium [81, 82]. Therefore 253MA (micro alloyed) stainless steel will also be investigated in this chapter. 253MA is comprised of 20-22% chromium and 10-12% nickel and with addition of 0.03-0.08 cerium. This gives it heat-resisting properties similar to type 310 stainless but it is cheaper due to having approximately half the nickel content.

This chapter will outline the production and analysis of these alloy composites. The work has been published as "Solidification phenomena during casting of stainless steel/cast iron composites"[85].

4.2 – EXPERIMENTAL

4.2.1 – STAINLESS STEEL/WHITE IRON COMPOSITE CREATION

Type 310 stainless steel tubes were filled with white cast iron pieces as shown in Figure 4.1, and heated above the melting point of white cast iron and allowed to soak for one hour.

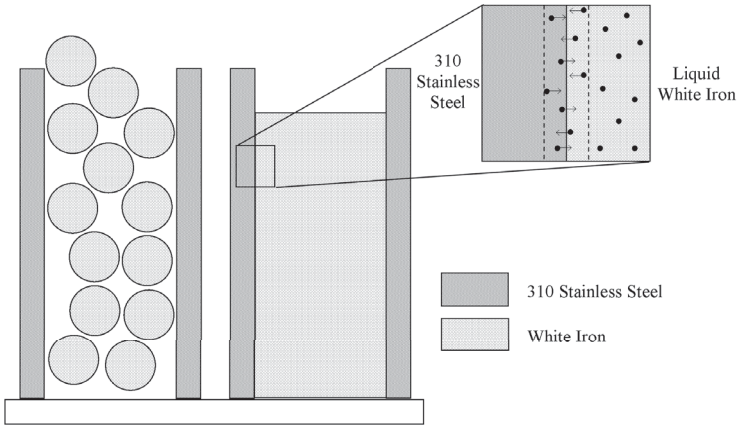

Figure 4.1: Cross-sectional schematic diagram of stainless steel tubing with white cast iron before and after casting. Also shown is a schematic of atomic diffusion between the liquid white iron and the stainless steel.

Composite alloy samples were produced in a specialised high temperature laboratory oven with vacuum and inert gas capabilities. The raw materials for the sample production consisted of foundry grade alloy ingots and wrought steel products. Each sample was produced under controlled thermal cycles where temperature, ramp rate, soak duration and cooling rate were all controlled and monitored. A typical heating cycle of these samples is shown in Figure 4.2.

The process of producing the composite alloys in the kiln has been termed 'kiln casting', and involves the whole sample, including mould and raw materials being placed into the furnace.

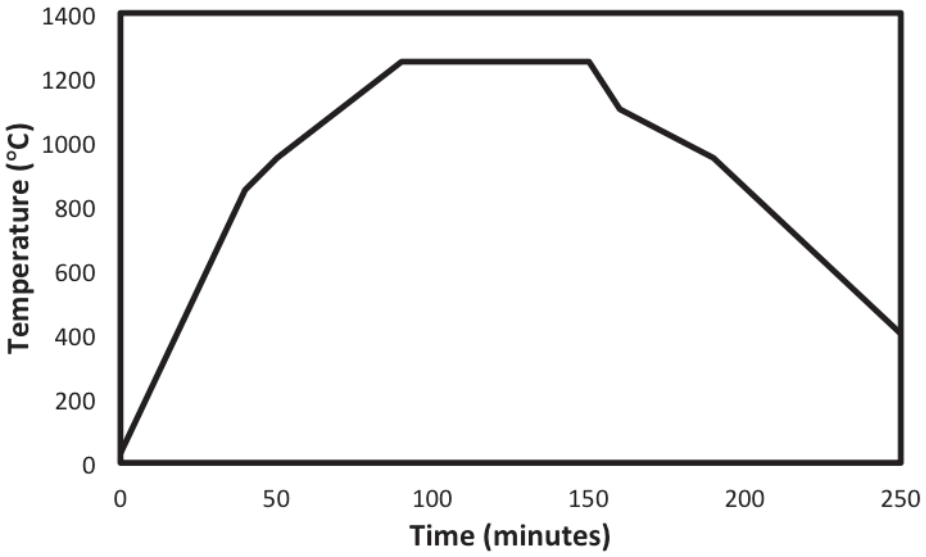

Figure 4.2: The typical furnace heating cycle used to create these composites.

The furnace process conditions were changed to study the effect of oxidation and choice of raw materials on the nature of the composite interface produced.

Three different samples were created in this manner. The details of these samples are shown in Table 4.1.

TABLE 4.1: CASTING PARAMETERS FOR TYPE 310 STAINLESS STEEL/WHITE IRON COMPOSITES

Sample No.	Temperature	Soak Time	Notes
1	1250°C	1 hour	Plunged into furnace set at 1250°C, air atmosphere
2	1250°C	1 hour	Placed in furnace at room temp and allowed to heat to 1250°C, air atmosphere
3	1250°C	1 hour	Plunged into furnace at 1250°C, along with ~2.5g of graphite, ~0.5g of manganese (99.9% electrolytic flake), air atmosphere

4.2.2 – Analysis Techniques

To improve the understanding of the diffusion mechanisms taking place in this composite manufacturing technique, the cylindrical samples were sectioned, mounted and polished in order to analyse the interfacial region of the sample. A variety of techniques were used to analyse the interface including optical microscopy, nano-indentation, scanning electron microscopy (SEM), energy dispersive spectroscopy (EDS), quantitative X-ray mapping (QXRM), and electron backscatter diffraction (EBSD) mapping.

SEM analysis was performed on a Zeiss Supra 55VP scanning electron microscope. The SEM was operated at 20 kV with a 120 μm aperture in high current mode for obtaining InLens, Secondary Electron and Back Scattered Electron images. EDS analysis using an Oxford Pentafet detector operating at 150 eV on setting 2 processing time and analysis performed for 100 seconds with 20,000 cps. The system was calibrated against copper at 20 kV for quant optimisation. HKL Technology EBSD was performed with an accelerating voltage of 20 kV and the sample tilted at 70°. X-Ray maps were taken using a JEOL 35CF operating at an accelerating voltage of 20 or 25 kV with the Moran Scientific XRM system and processed using Moran Chemical Imaging software.

4.3 – Results and Discussion

4.3.1 – Microstructural Investigation of the Composite Interface

Images taken from samples 1 and 2 are shown in Figure 4.3.

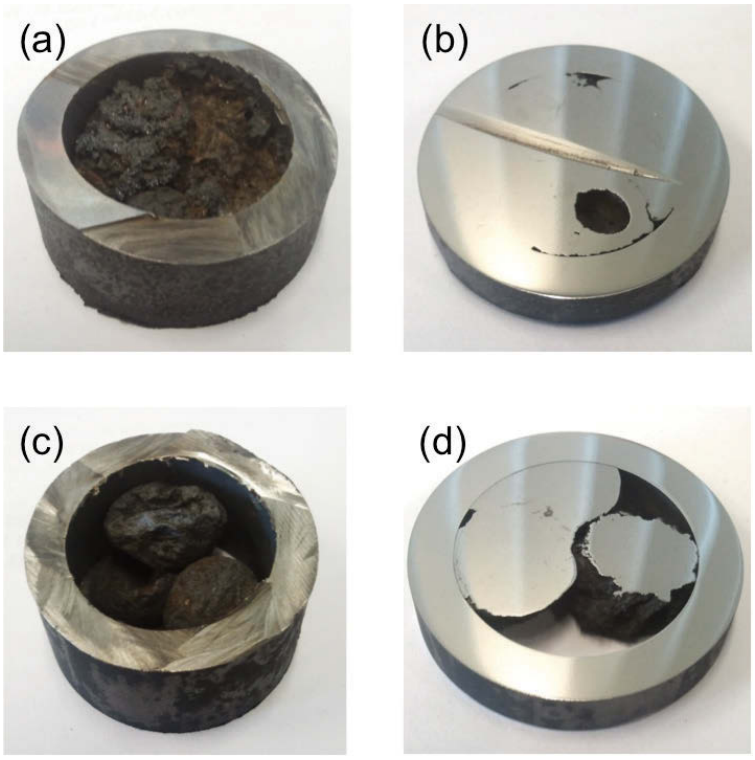

Figure 4.3: (a) Shows extensive oxidation of the white iron balls and (b) shows the poor bonding with the stainless steel substrate. (c) Sample 2 shows even greater oxidation of the white iron and (d) very poor bonding with the steel substrate.

It was found that the cast iron of both samples 1 and 2 was badly oxidised and very poorly bonded with the steel substrate. Clearly oxidation needed to be minimised, so in sample 3 graphite flakes were added in order to scavenge the oxygen in the surrounding volume, while manganese was added in order to increase wetting of the steel substrate by the liquid white iron.

As can be seen in Figure 4.4, the molten white iron of sample 3 adequately wetted the steel substrate and excellent bonding was achieved with the stainless steel tube when compared with Figures 4.3 (a) & (c).

Figure 4.4: Image showing the stainless steel tube with white cast iron bonded to the inner wall of the tube.

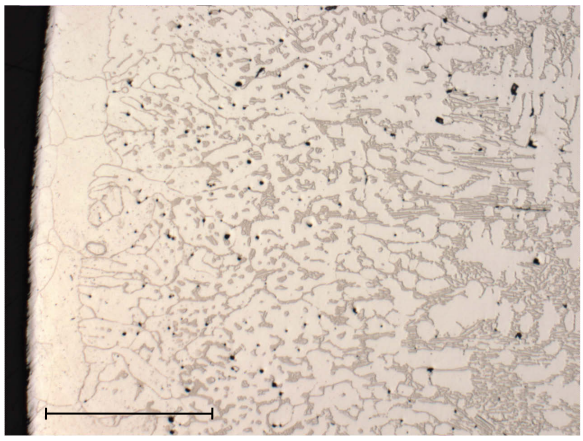

Figure 4.5: Optical micrograph of interfacial region of the sample shown in Figure 4.5. LHS steel tube, RHS white cast iron. Black spots in white cast iron region of sample were caused by carbide pullout during grinding and polishing. 2.5x magnification, horizontal width of field. (HWOF = 3.5mm)

Figure 4.5 shows the growth of eutectic carbides on the right hand side of the optical micrograph. The total number of carbides per unit area decreases from right to left indicating a decreasing proportion of carbon across this diffusion affected zone.
Optical microscopy revealed that there was a continuous and high quality metallurgical bond between the cast iron and the outer tube. The interface had a complex microstructure and considerable diffusion of carbon had occurred into the type 310, as evidenced by the large proportion of carbides in the stainless steel tubing that was virtually carbon free prior to casting.

When comparing the interface of the type 310 stainless steel composite shown in Figure 4.6 to composites made with other types of steel substrates (Figure 4.6), it can be seen that there is no defined interface layer in the case of the type 310 composite.

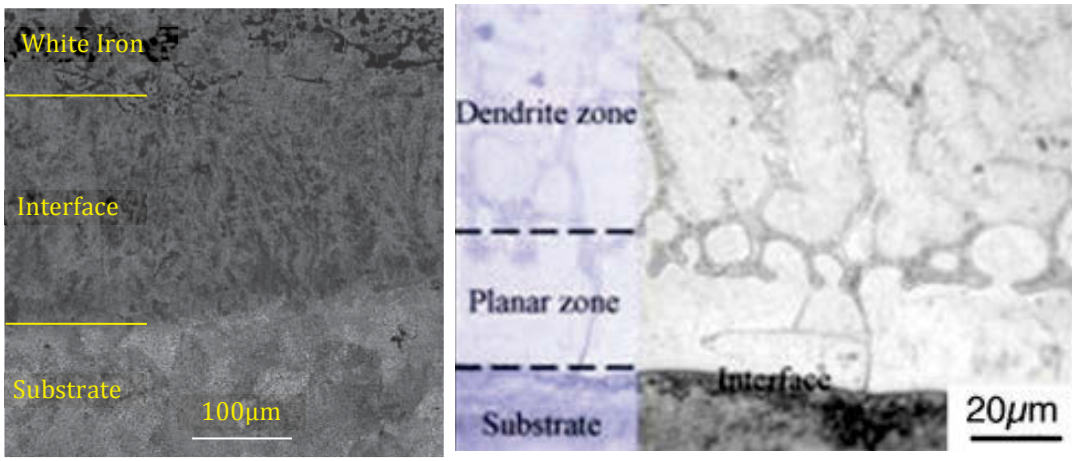

(a) (b)

Figure 4.6: (a) shows the interfacial region of a white iron/mild steel composite created using the vacuum cast technique [37]. Micrograph (b) shows the interfacial region of a white iron/steel composite created using hardfacing [42].

In order to gain a better understanding of the degree of diffusion of various elements, quantitative X-ray mapping (QXRM) was employed. Figure 4.7 shows an EDS map of the interfacial region of this sample with a 5.56 mm horizontal width of field (HWOF).

Due to the low magnification of this image, quantitative WDS carbon mapping was not possible but a full spectrum map above 0.2 keV was acquired using EDS revealing the inter-diffusion of iron, chromium, nickel etc. between the two materials.

As previously mentioned, the type 310 stainless possessed little carbon originally, so it is fair to assume that the carbon required for the formation of the chromium-rich carbides present up to a depth of 2.5 mm into the type 310 stainless has diffused from the WCI into the type 310 stainless tube.

Still, based on the microstructure observed across the interface of the composite, the joint can be defined by four distinct regions. Zone A is still substantially type 310 stainless steel and is not much altered by the heat treatment. Zone B consists of chemically altered type 310. This region remained solid during the heat treatment but analysis indicated that it has been depleted of nickel and enriched in carbon. This must have been by counter-current processes of diffusive mass transfer across the solid-liquid interface. Zone C was evidently partially molten during the heat treatment. It appears to have consisted of solid dendrites of austenite surrounded by carbon-rich liquid while at temperature. Zone D was the original molten cast iron, now solidified with a hypoeutectic carbide microstructure.

Given that the type 310 tube had a wall thickness of 4.5 mm at the start, it is also obvious that it has partially dissolved into the molten cast iron phase. The stainless steel contained little carbon originally, so the carbon in the carbides visible in its chemically affected Zone B must have diffused there from the cast iron. These carbides originally took the form of stringers and have proceeded to grow thicker and form eutectic carbides. Quantitative analysis also indicates that nickel has diffused from the type 310 tube into the cast iron.

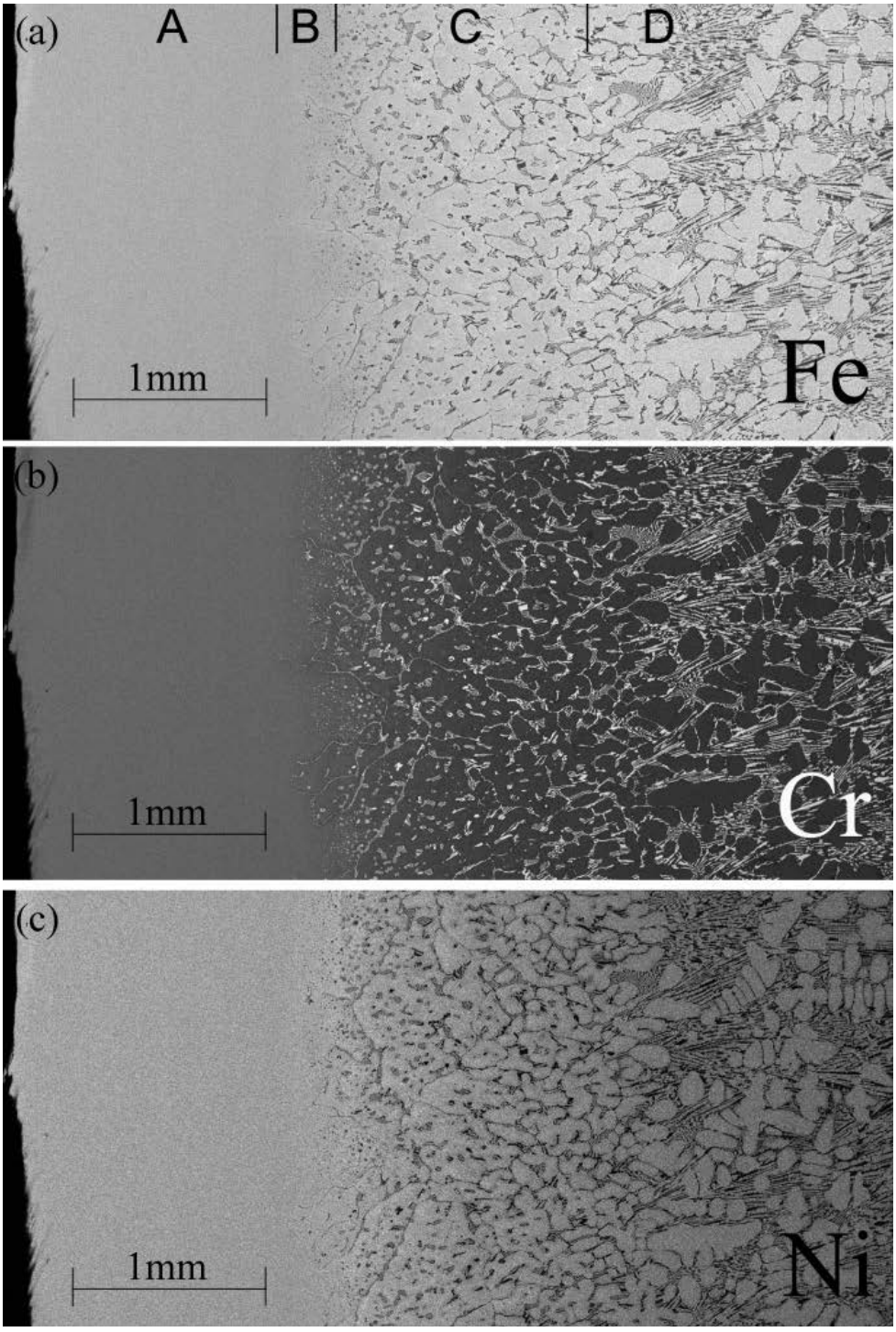

Figure 4.7: Elemental maps taken over interface between type 310 tube and white cast iron interior. The four distinct zones in the microstructure are labelled A, B, C and D. The original position of the inner surface of the type 310 tube corresponds closely to the right hand edge of the images, illustrating that considerable dissolution of the tube occurred. (HWOF=5.56mm)

Figure 4.8 shows a pseudocolour X-ray map of the interfacial region. Full spectrum data was gathered at a rate of 200 ms per pixel. In this image nickel content is blue, chromium is green and iron is red. The horizontal width of field is approximately 5.5 mm. The dotted white line indicates the inner edge of the stainless steel pipe and it can be seen that carbon, in the form of M_7C_3 carbides, has diffused approximately 2.5 mm into the pipe, creating a strong interfacial bond between the white cast iron and type 310 stainless steel. A gradient of colour from purple to pink can be seen on the right hand side of the XRM. This is due to the nickel diffusing out of the tube and into the white cast iron.

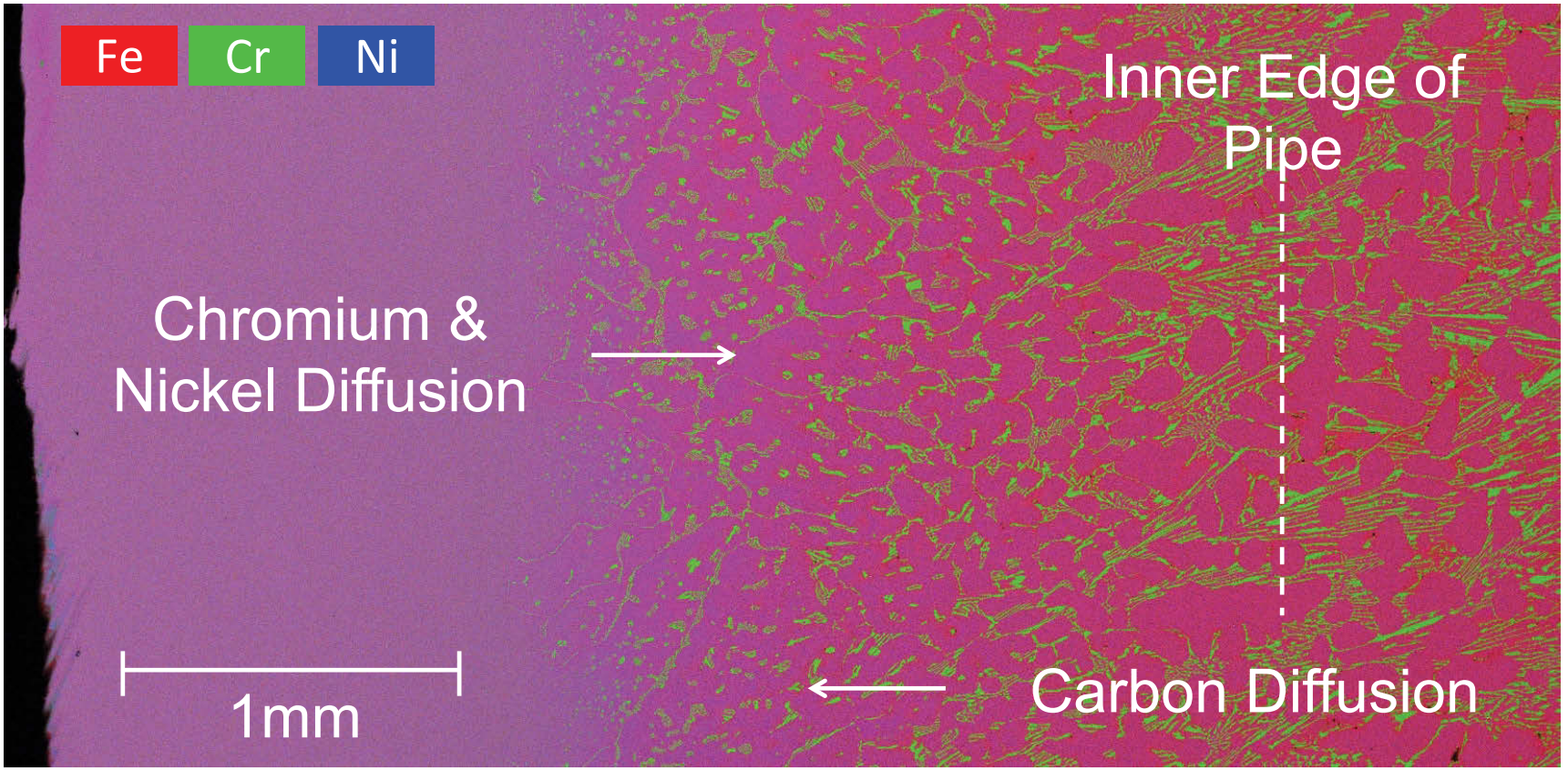

Figure 4.8: Pseudocolor XRM at the interface of stainless steel (left) and white cast iron (right). Nickel is shown as blue, Iron as red and Chromium as green. 30x magnification. (HWOF = 5.56mm)

In order to better understand the specific phases present at the interface, a higher magnification X-ray map was taken of this interfacial region with the iron, chromium and nickel maps shown in Figure 4.9.

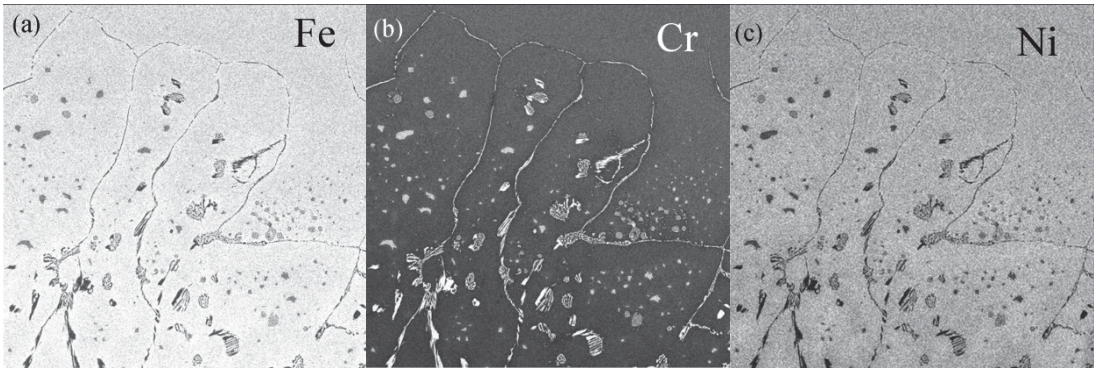

Figure 4.9: Elemental maps of the interface approximately 1.8 mm from the outer edge of the pipe. The stainless steel is top right and the white cast iron bottom left in these images, with the interface diagonally between them from top left to bottom right. (HWOF = 900μm)

When these three maps are combined and coloured as shown in Figure 4.10 it can be seen that there is a gradient of nickel and iron between the bottom left and the top right hand corner of the screen. It appears that chromium carbides have formed along the grain boundaries and these carbides are generally higher in chromium than those that have formed in the middle of grains.

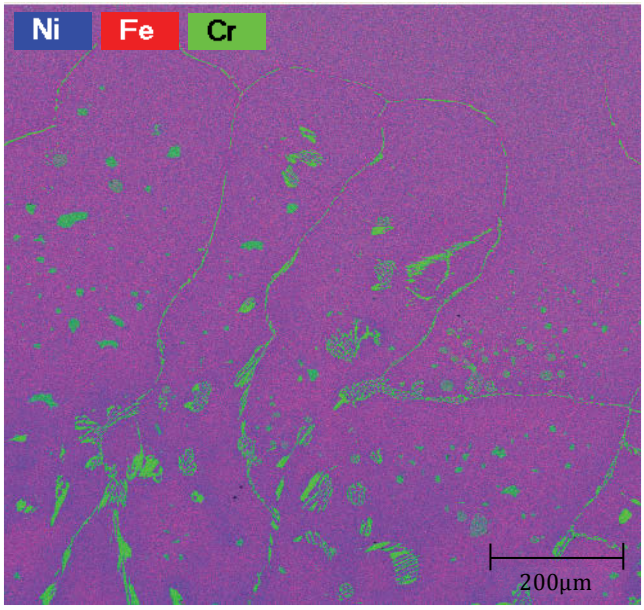

Figure 4.10: Pseudocolor XRM at the interface of stainless steel (top right corner) and white cast iron (bottom left corner). Nickel is shown as blue, iron as red and chromium as green. 300X magnification. (HWOF = 900µm)

The X-ray intensity distributions of the elements from an X-ray map allow us to generate two dimensional scatter diagrams thus converting spatial information into concentration dimensions, which is a helpful tool for displaying the spatial relationships of elements or phases in materials.

Two-dimensional scatter diagrams show pixel frequency versus element concentration profiles and are plotted against each other for selected elements within the sample. The two dimensional scatter diagrams are given an extra dimension by thermally colouring the intensity of points on the diagrams. This dimension indicates the number of points in the image with this concentration. From these scatter diagrams we observe clusters, also referred to as nodes, which correspond to different chemical phases (Figure 4.11).

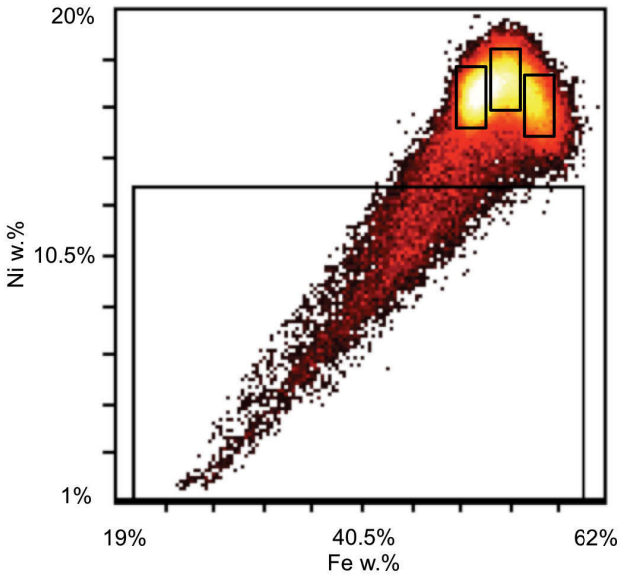

Figure 4.11: Within this iron-nickel scatter diagram, four phases can be identified. We can observe linking between clusters indicating the boundaries between phases within a material.

The contributing pixels of each cluster can be used to reconstruct the spatial distribution of its associated chemical phase or boundary in a chemical image of the specimen. Figures 4.12 to 4.15 show secondary electron images with information from the different clusters of their respective scatter diagram superimposed over the image in yellow. After the phase has been selected on the scatter diagram, the chemical data of that phase can then be quantified and the composition of each phase can then be determined.

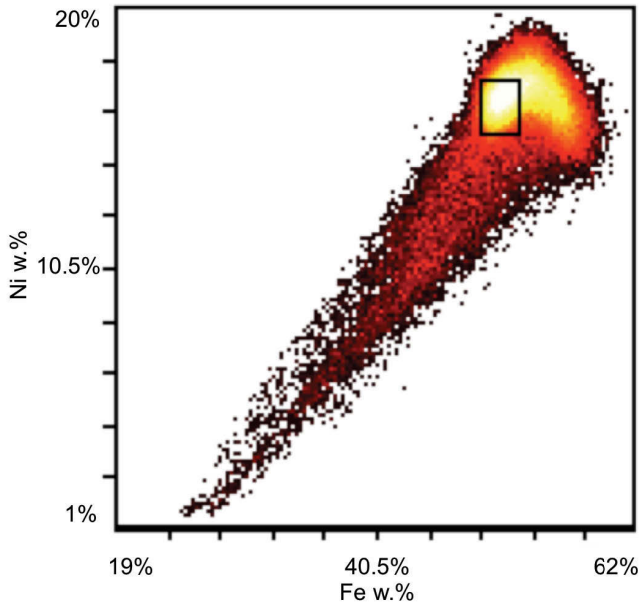

Element	Atom %	Weight %
Ni	16.7	17.9
Fe	52.2	53.1
Mn	3.1	3.1
Cr	26.7	25.3
Si	1.3	0.6

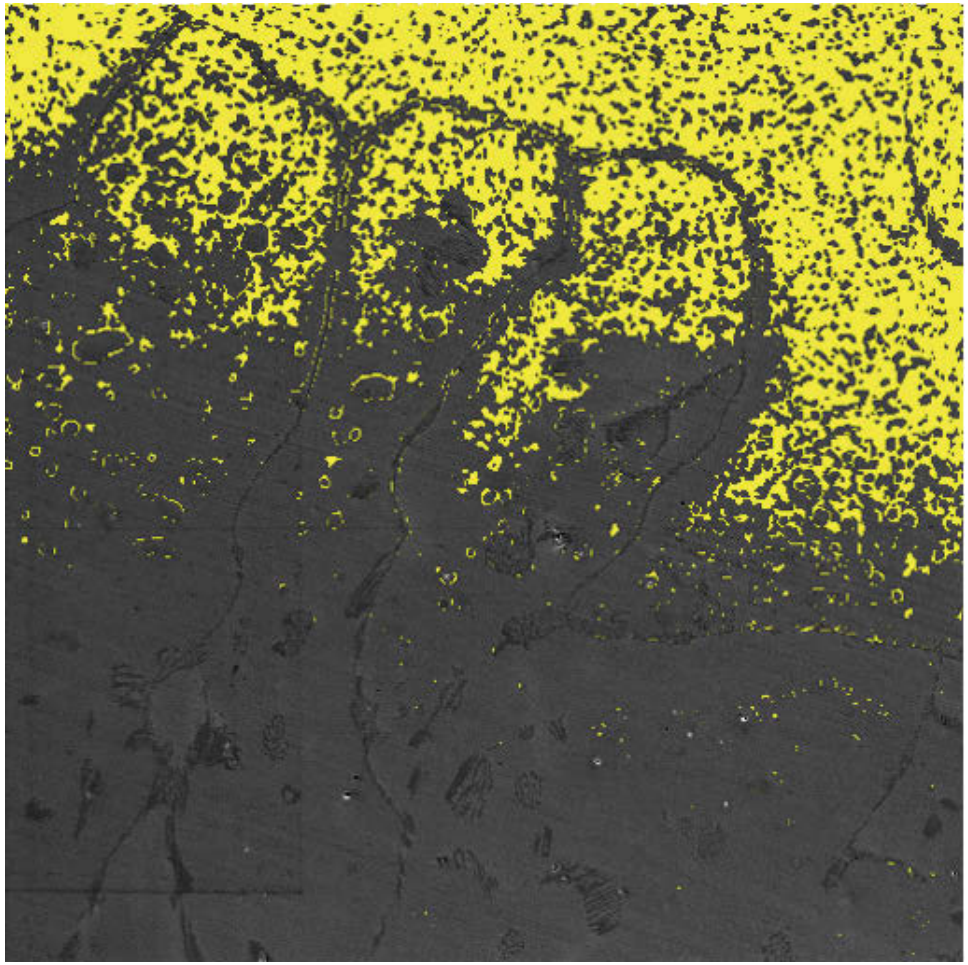

Figure 4.12: Phase selection of the substrate side of the interface. Across this interface there appears to be an inverse relationship between chromium and iron contents as shown in the nickel/iron scatter diagram and this phase was selected based on high nickel/low iron content. (HWOF = 900µm)

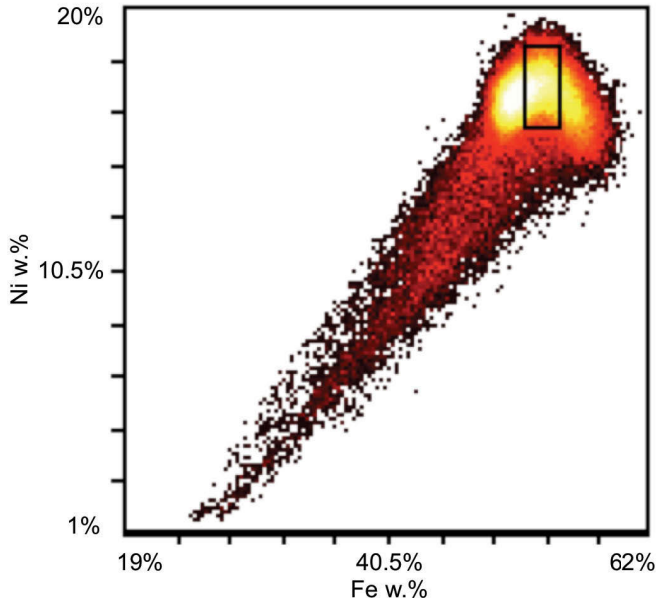

Element	Atom %	Weight %
Ni	17.6	18.8
Fe	55.3	56.1
Mn	2.9	2.9
Cr	22.9	21.6
Si	1.3	0.7

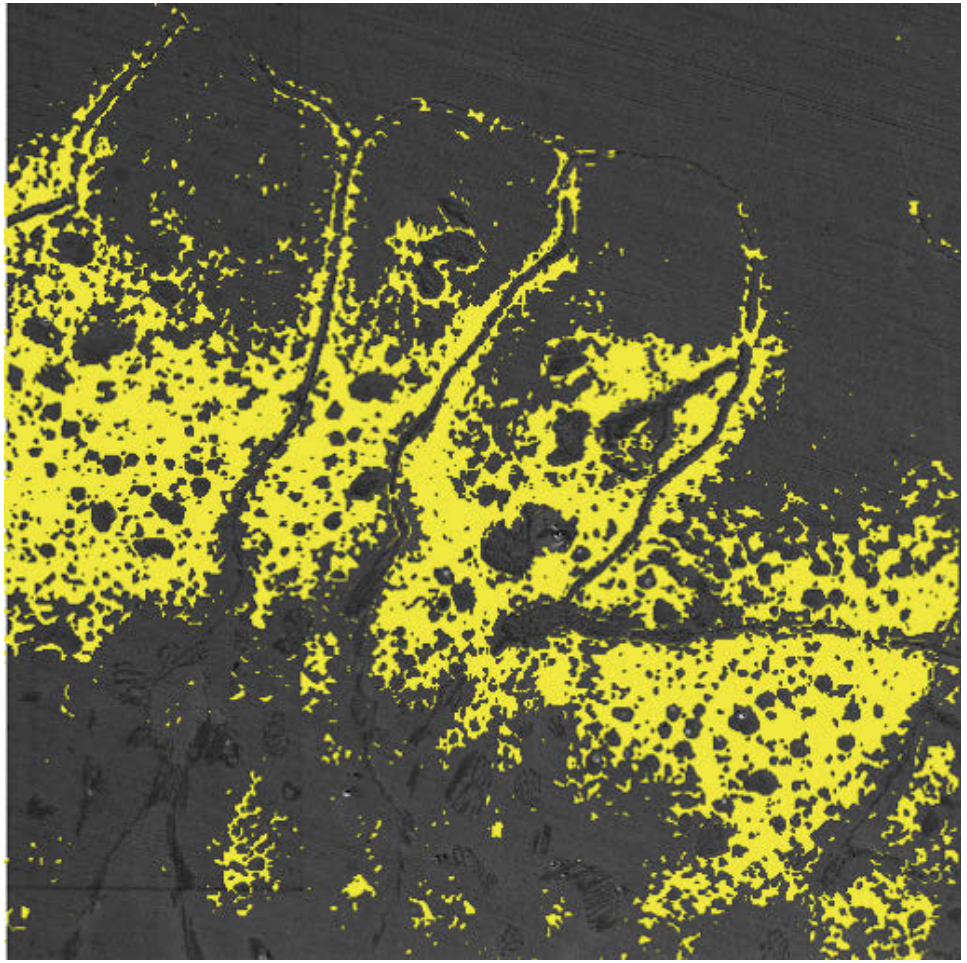

Figure 4.13: Phase selection of the interfacial region of this composite. This region is typified by slightly higher nickel content. (HWOF = 900µm)

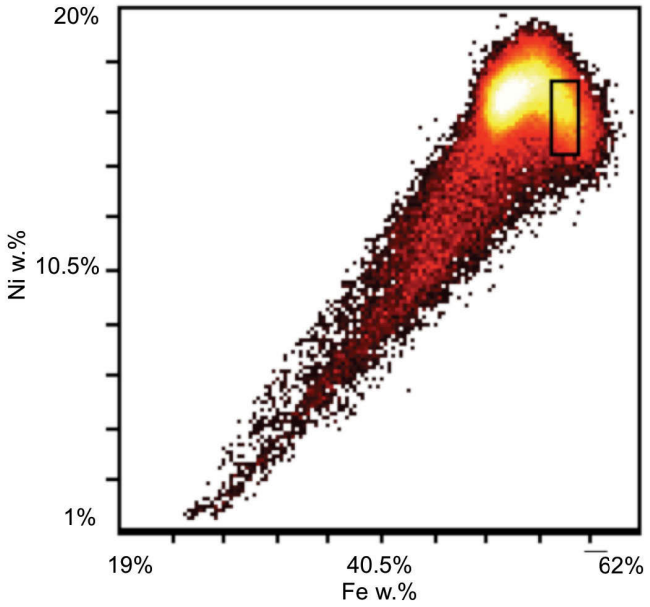

Element	Atom %	Weight %
Ni	17.1	18.1
Fe	58.8	59.5
Mn	2.8	2.8
Cr	28.1	18.9
Si	1.3	0.7

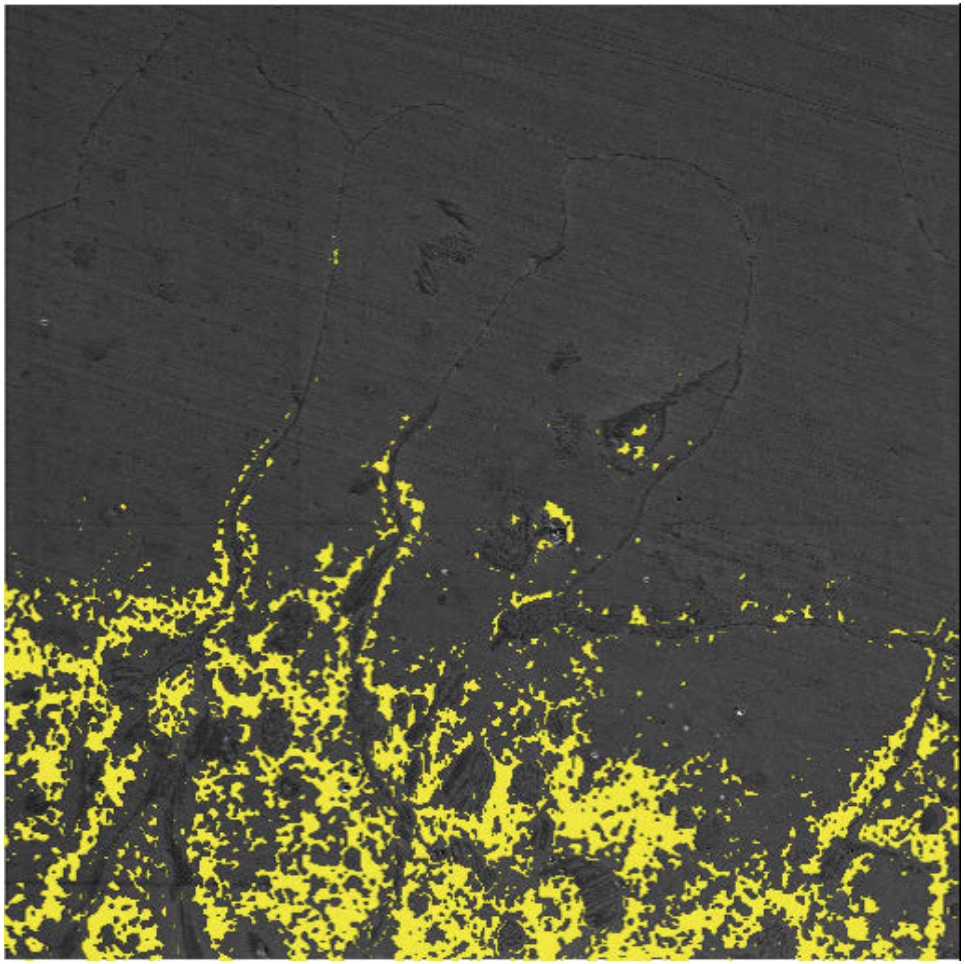

Figure 4.14: Phase selection of the white iron side of the interfacial region. This region is identified by higher iron/lower nickel content. (HWOF = 900µm)

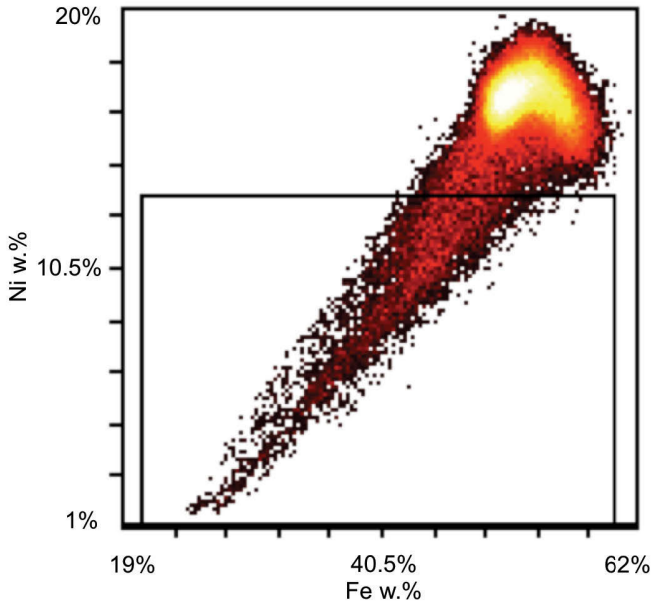

Element	Atom %	Weight %
Ni	6.4	7.0
Fe	35.2	36.6
Mn	4.0	4.1
Cr	53.6	51.9
Si	0.8	0.4

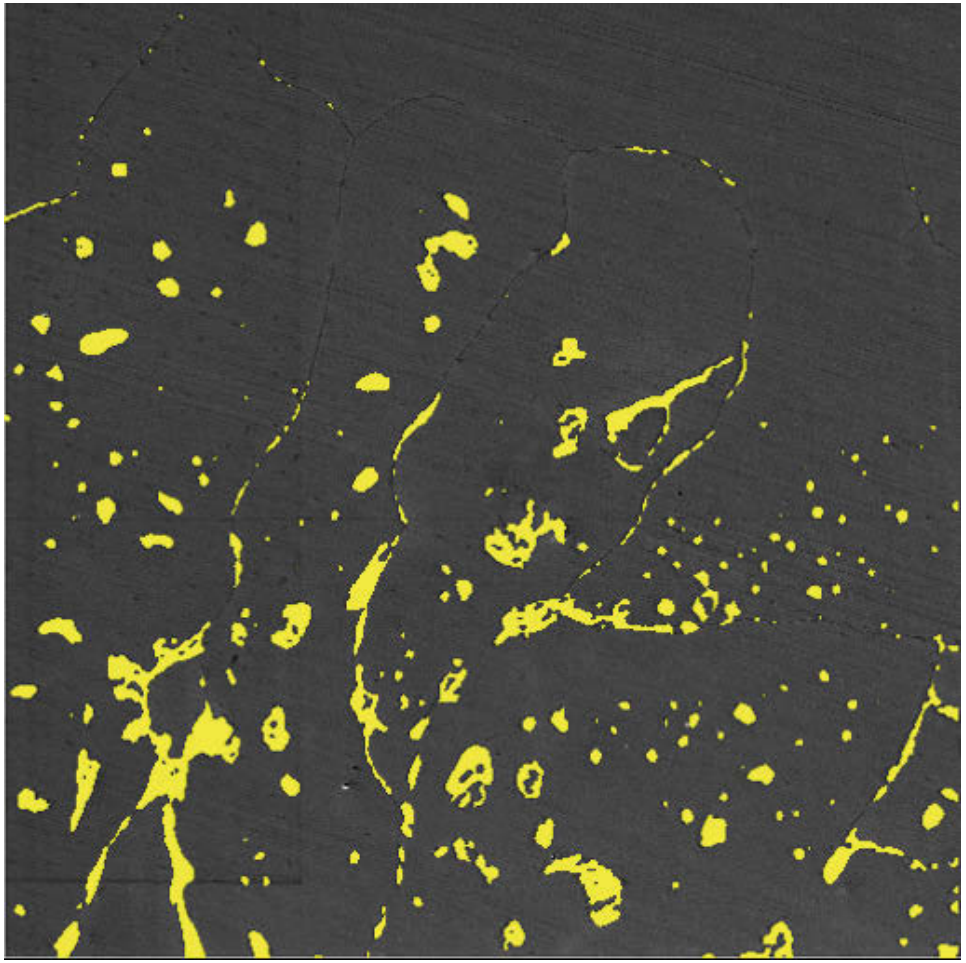

Figure 4.15: Phase selection of the white iron side of the interfacial region. This region is identified by lower iron/lower nickel content. (HWOF = 900µm)

Figures 4.12-15 shows three different zones in the interfacial region. These zones are shown as nodes in the Ni-Fe and Ni-Cr scatter diagrams. In Figure 4.13 it can be seen that nickel levels increase in the central area of the interfacial region and this increase could thus be used to identify the location of the interface of the stainless steel and white cast iron.

From these results we can assess the extent of the diffusion of the carbides and this could be used as an identifier of the interfacial region.

4.3.2 – Nanoindentation of the Stainless Steel/White Iron Composites

As an alternative to using X-ray mapping, nano-indentation may be used to identify the extent of the growth of the M_7C_3 carbides. Figure 4.16 shows a nano-indentation profile taken across the interfacial region of the type 310 stainless steel/white cast iron composite. The ferrous matrix is shown to possess a relatively uniform hardness and the hardness increases when a carbide is struck by the diamond indentor.

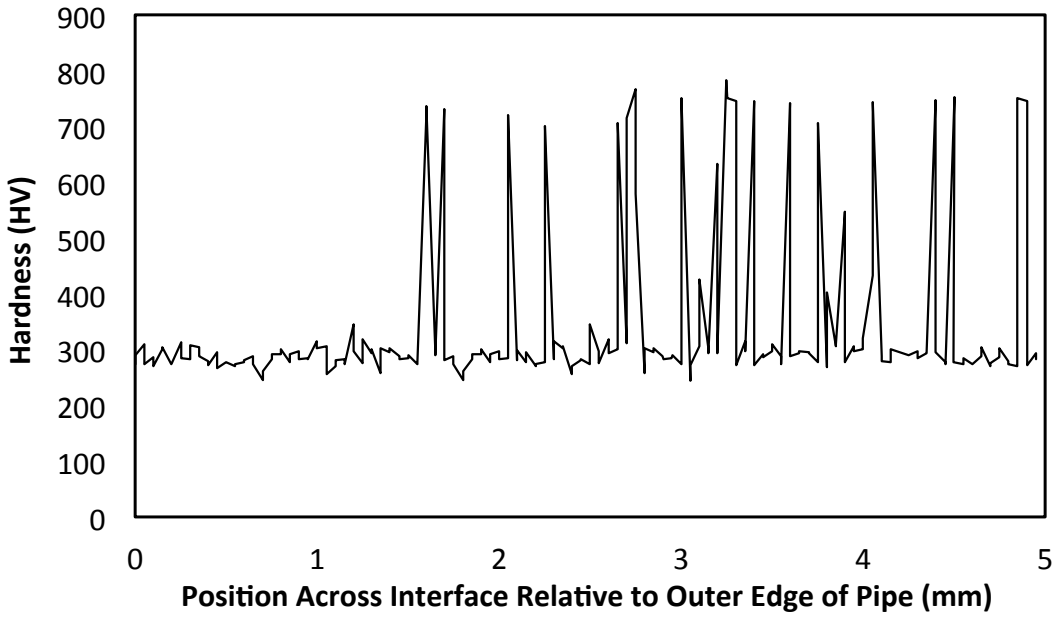

Figure 4.16: Comparitive hardness profile of sample across the interface from nanoindentation. The first 1.5 mm of the profile is of the carbide free, outer edge of the type 310 stainless steel tube.

The nano-indentation profile confirms the results obtained from X-ray maps. It can be seen that carbides have grown 3 mm into the steel tube with the outer 1.5 mm of the steel tube being still free of carbides after the treatment.

Nano-indentation can also reveal the reduced modulus, E_R, of the material which is related to the Young's modulus of the material as shown in Equation 1 where v_i is the Poisson ratio of the indentor tip and E_i is the Young's modulus of the indentor tip which are 0.07 and 1140GPa respectively for a diamond indentor. Here v_s is the Poisson ratio of the test specimen and E_s is the Young's modulus of the test specimen.

$$\frac{1}{E_R} = \left(1 - \nu_i^2\right)/E_i + \left(1 - \nu_s^2\right)/E_s \qquad \text{EQUATION 4.1}$$

A profile of the reduced modulus is shown in Figure 4.17 and it can be seen that as the carbon has diffused into the stainless steel tube, it has had the effect of reducing the elastic modulus of the material.

Figure 4.17: Nano-indentation profile showing the reduced modulus of the sample across the interface using a Hysitron Triboindentor 900 nano-indentation system.

4.4 – CHAPTER CONCLUSIONS

In this chapter it has been shown that a good metallurgical bond can be attained between a stainless steel substrate and white iron that has been cast onto it, even if melting is conducted in air. Use of X-ray mapping in a SEM revealed extensive counter-current diffusion of iron, chromium, nickel and carbon. The individual analyses could be combined to yield a detailed understanding of the microstructure of the interface. Carbon diffuses into the stainless steel via both the grain boundaries and solid state volume diffusion, causing carbides to form along the grain boundaries and specifically at the triple junctions between grain boundaries. Other elements have diffused to a much lesser extent into the stainless steel substrate while nickel has diffused from the steel substrate into the liquid white iron. The microstructure could be further characterized using nano-indentation transects, which provided a confirmation of the zonation determined using compositional metallography.

CHAPTER 5 – CASTING OF WHITE IRON ONTO A MILD STEEL SUBSTRATE

5.1 – INTRODUCTION

In the previous chapter I used the example of a type 310 stainless steel substrate to demonstrate that excellent bonding between white cast iron and a substrate can be achieved provided that oxidation can be restricted. However, type 310 would be an exceedingly expensive and inappropriate choice for mining equipment subjected to impact and wear. Ideally, the industry wants to use cheap mild steel or medium carbon steel as the backing material, with only the wearing surface made of the white cast iron. Therefore, in the present chapter I investigate the all-important question of whether the "kiln casting" process can produce good joints between white cast iron and a mild steel substrate.

Prior to my project there had been no detailed study of the interfacial phenomena occurring during the kiln casting process. Therefore, the present chapter will examine in detail the nature of the interface obtained by kiln casting of white cast iron onto mild steel in an air environment. The work in this chapter has been published as "Interfacial reactions in white iron/steel composites[86]

In the present work, the joint between the steel and the white iron is characterized by a clearly visible interfacial layer of several tens of microns thickness. Interfacial layers have also been observed in other joints between dissimilar alloys produced by techniques such as vacuum casting[39] and hardfacing[87]. For example, the latter workers found that fusion bonding of a 40% chromium white iron to an ASTM A36 steel plate resulted in the formation of a planar interfacial layer of alpha phase layer via epitaxial solidification. Following formation of the layer, solidification of the balance of the melt occurs to form a solid with the nominal composition of the cast iron or filler. However, the nature, rate of formation and crystallographic orientation of the interfacial layer formed in the present mild steel/white cast iron joints was not known.

These parameters would be expected to affect both method of production and performance in service.

As it has been shown that the nature of the growth of this layer is epitaxial[42] it is important to understand what epitaxial growth is. The term epitaxy is derived from two Greek words, *epi,* meaning "upon," and *taxis,* meaning "ordered." Epitaxial growth is characterized by the growth of a thin crystalline layer upon a crystalline substrate with the new layers atoms aligning with the crystal structure of the layer below it, creating a larger single crystal or grain. Clearly, the newly deposited material inherits the crystallographic texture of its substrate.

5.2 – EXPERIMENTAL

5.2.1 – CASTING OF WHITE IRON/STEEL COMPOSITES

White cast iron (WCI)/mild steel composites were created by placing a mild steel cup containing a white iron ingot in a furnace at 1250°C (Figure 5.1).

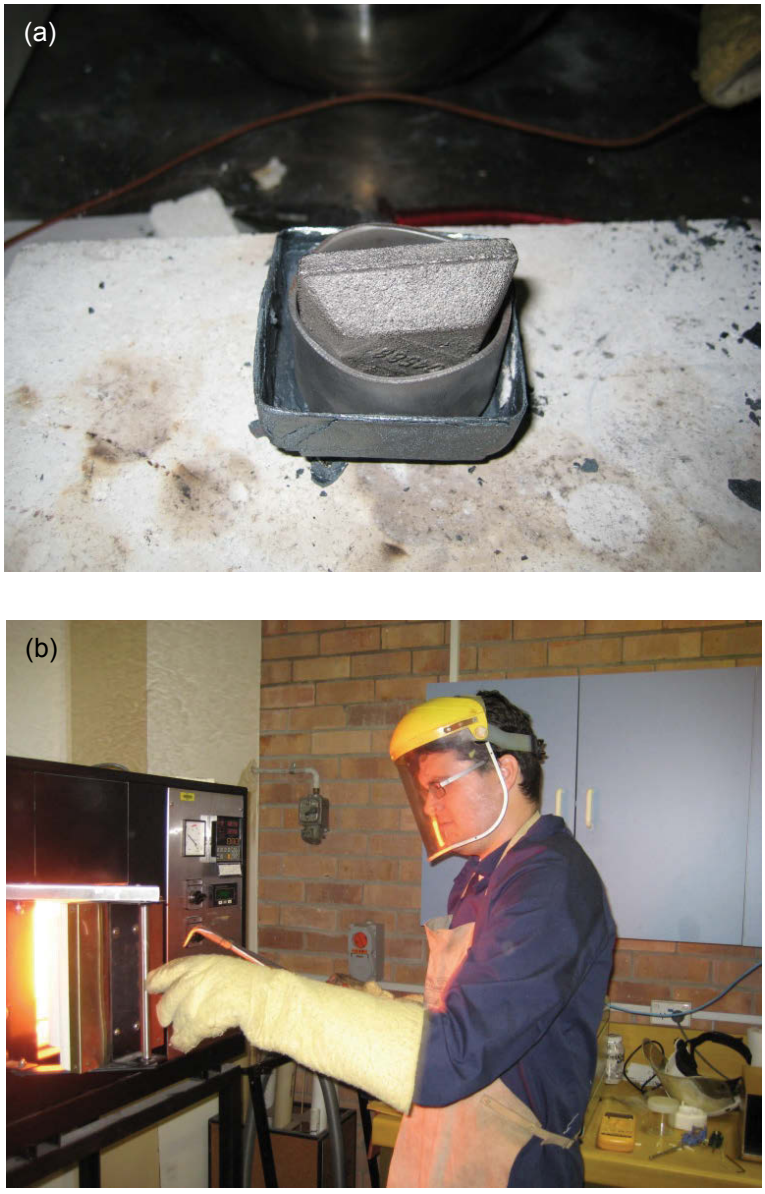

Figure 5.1: (a) White iron ingot in mild steel cup. This cup was placed inside a larger steel cup to avoid spillage of molten iron in furnace in case of failure of the mild steel cup. (b) shows the high temperature furnace used in this study.

As discussed previously, the WCI used was developed by Huggett and Ben-Nissan and has a melting point of only 1209°C [27] with the composition shown in Table 5.1.

TABLE 5.1. NOMINAL COMPOSITION OF WHITE CAST IRON USED IN TRIALS.

Element	Wt.%
C	4.1
Cr	12.0
Mn	1.6
Ni	1.0
Si	0.5
Fe	Balance

When the WCI became molten, it wetted the surface of the steel thereby initiating a complex sequence of metallurgical phenomena, including both partial dissolution of the mild steel substrate, and mass transfer of alloying elements in both directions across the interface, Figure 5.2.

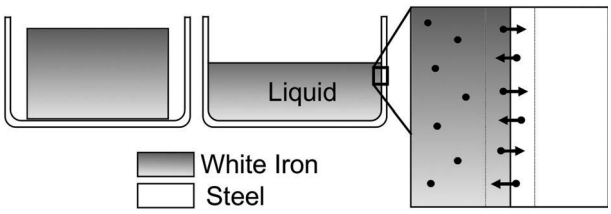

Figure 5.2: Cross sectional schematic of white iron/mild steel composites with graphical representation of atomic diffusion between layers.

Samples were cast with soak times ranging from 5 to 25 minutes, followed by furnace cooling. The temperature of the melt was monitored by a thermocouple placed in the steel cup and a data logger gathered the data. An example of the temperature profile of a sample placed into a furnace at 1250°C is shown in Figure 5.3. The purpose of varying

the soak time was to determine the optimal bonding conditions under minimum soak time. The samples were sectioned and polished for microstructural analysis in order to assess the effect of soak time on the development of the interfacial region.

Samples were also cast with a white iron of the same composition to which 10 vol.% niobium carbides ranging from 1-30μm in diameter had been added. These particles are more dense than the liquid white iron (8.35g/cm^3 *vs.* ~7.2g/cm^3) and relatively inert at 1250°C in white iron. They were added to assess the extent of the settling in the melt. This alloy was created by remelting 48.87g of the low melting point white iron in addition to 6.13g NbC particulates in an Edmund Buhler argon arc furnace, creating a 55g button containing 10 vol.% NbC particulates. This was then cast in a mild steel cup as described in the previous paragraph.

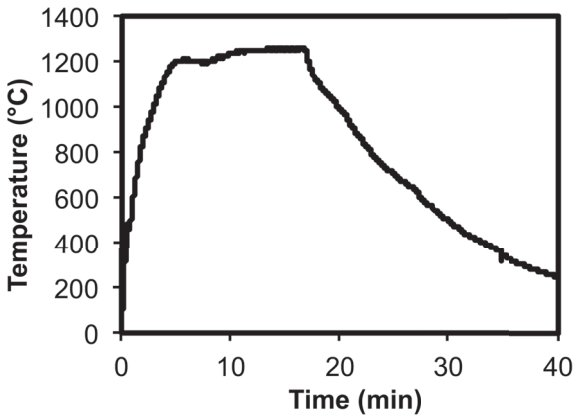

Figure 5.3: Typical heating curve of sample undergoing a 10 minute soak time.

5.2.2 – Sample Preparation

5.2.2.1 – Microstructural Analysis

Polishing was carried out on a Kent 3 automatic lapping and polishing instrument with a Struers magnetic disc attachment. Samples were hand ground using subsequent orthogonal grindings starting at 200 grit and finishing with 1200 grit. Following grinding, the sample was polished with 6 μm diamond on a napless nylon pad with a 1000 N load for 10 minutes followed by 1 μm diamond on a napless nylon pad with a 1000 N load for 5 minutes. Using napless pads resulted in a plane surface while pads

with nap resulted in relaxation of the matrix around the carbides due to the large differential in hardness, which is undesirable. Finally, to remove any remaining fine scratches, samples were hand polished with 50 nm colloidal silica for approximately 20 seconds on a neoprene pad, which provides a small amount of both fine mechanical polish and chemical etching. Extended polishing with colloidal silica on a neoprene pad should be avoided as carbide/matrix boundaries are preferentially etched.

5.2.2.1 – High Temperature Confocal Laser Scanning Microscopy

Samples for confocal microscopy investigation were prepared by casting white iron pins inside a quartz tube of 4 mm ID, which were then press fitted into a 3.98 mm diameter hole drilled into the core of a 10 mm diameter mild steel rod. The composite sample was then sectioned into 2 mm thick discs as shown in Figure 5.4. These samples were then polished.

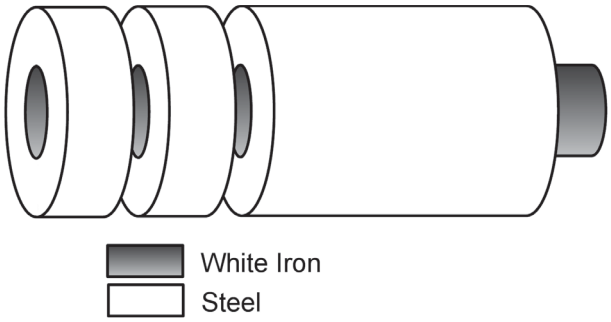

Figure 5.4: Schematic of cylindrical test samples, created for confocal laser microscopy.

5.2.3 – Analysis Techniques

5.2.3.1 – SEM Based Techniques

Several microanalysis techniques were employed to examine phases and defects present within the interfacial region, including scanning electron microscopy, energy dispersive spectroscopy, and wavelength dispersive spectroscopy. A Zeiss 55VP FEGSEM was generally used to obtain micrographs. This was operated at 20 kV with an aperture of 120 μm in a high current mode. Backscattered electrons were gathered using a Rutherford backscatter detector providing an image with contrast based on atomic number. EBSD data was obtained using a HKL Nordlys S system mounted on the aforementioned Zeiss instrument and data was analysed using HKL Tango (mapping) and HKL Mambo (pole figures). X-ray mapping (XRM) was performed using the Moran Scientific X-Ray Analysis System incorporated on a Jeol 733 microprobe. The maps were ZAF corrected.

Some samples were etched for further microanalysis using either a 2% nital or acidic ferric chloride etch.

5.2.3.2 – Computational Analysis

DICTRA diffusion simulation software§ was employed to model the diffusion between the white iron and the mild steel. While the software has built in parameters to calculate the rate of solid-state diffusion in the substrate, the mass transfer within the melt is not well quantified. These variables are corrected using a labyrinth factor [88, 89], which was calculated based on experimental findings and was used to increase all diffusion coefficients by a constant factor.

§ DICTRA is a product of Thermo-Calc Software AB, Norra Stationsgatan 93, Plan 5, SE-113 64 Stockholm

5.2.3.3 – HIGH TEMPERATURE CONFOCAL LASER SCANNING MICROSCOPY

In order to assess the development of the interfacial layer *in-situ,* high temperature confocal laser scanning microscopy (HTCLSM) was conducted in a Lasertec 1LM21 series confocal laser scanning microscope, under an ultra-high purity inert atmosphere (>99.9999% Ar). In this furnace, a 1.5 kW halogen lamp heats the specimen and the temperature is measured by a type B thermocouple welded to the outer edge of the platinum crucible holder. A schematic of the HTCLSM is shown in Figure 5.5.

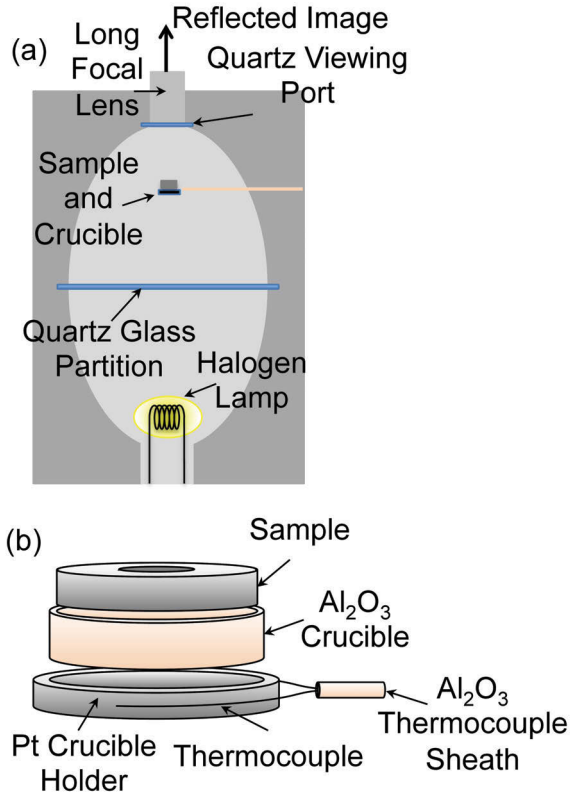

Figure 5.5: (a) Schematic diagram of the infrared furnace of the laser-scanning confocal microscope and (b) the sample holder.

5.2.3.4 – NANOINDENTATION

Nano-indentation profiles of the interface were taken using a Hysitron Triboindentor 900 (Figure 5.6). This provides hardness and reduced modulus data of the various phases.

Figure 5.6: Hysitron Triboindentor 900 nano-indentation system.

A diamond Berkovich tip was used with a maximum load of 1000 μN. Loading and unloading was carried out over a 20 second period with the loading and unloading calibration curve with respect to time shown in Figure 5.7.

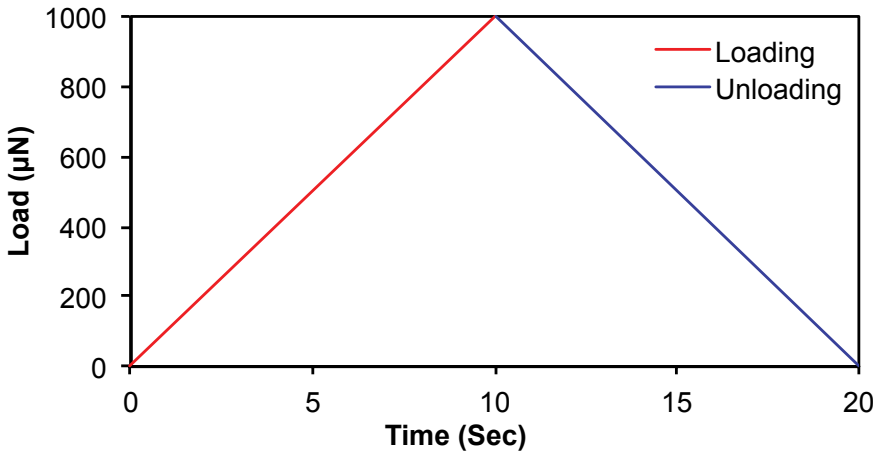

Figure 5.7: Loading and unloading calibration curve.

A load versus displacement curve shown in Figure 6 provides both hardness:

$$H = \frac{P_{max}}{A_r} \qquad \text{EQUATION 5.1}$$

where P_{max} is the maximum load and A_r is the residual area of the indentation. The hardness provided from the tests carried out in this study is uncalibrated so actual hardness may not be quantified but as the hardness of the phases shown are well documented, this is not necessary. The hardness tests shown simply provide a comparative measurement.

Reduced Young's modulus is given by:

$$E_r = \frac{1}{\beta}\frac{\sqrt{\pi}}{2}\frac{S}{\sqrt{A_p(h_c)}} \qquad \text{EQUATION 5.2}$$

where β is a geometric constant of the indenter (Berkovich = 1.034), $A_p(h_c)$ is the projected area of the indentation at contact depth h_c and stiffness:

$$S = \frac{dP}{dh} \qquad \text{EQUATION 5.3}$$

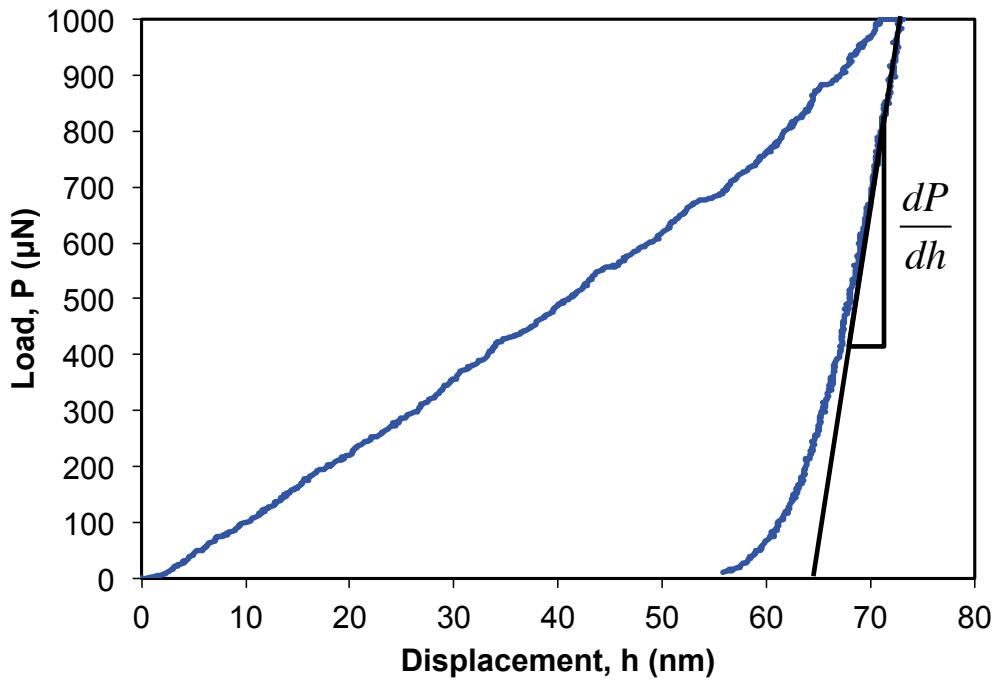

Figure 5.8: Typical single indent load versus displacement curve.

Two line profiles were taken across the interface of each sample spaced 5 μm apart. Each line consisted of 40 indentations each spaced 5 μm apart.

5.2.3.5 – Three-Point Bend and Tensile Tests

In order to establish the strength of the bond between the steel and the white iron, specimens for both three-point bend and tensile testing were created by placing a 4 mm diameter steel rod and a 4 mm diameter white iron pin inside a quartz tube with an inside diameter of 4 mm. This tube was sealed and heated till the white iron was liquid and subsequently an interfacial layer was formed. These were created under a variety of soak times. Each specimen was placed in a load cage of a three-point bend apparatus with a distance of 30 mm between outer supports, and tensile test jaws connected to a Shimadzu AGS-X universal tester and loaded with a head displacement of 1 mm/min.

5.3 – Results and Discussion

5.3.1 – Characterization of Interface

The first task to be undertaken in this part of the project was microstructural evaluation of the bond between the steel and the white iron. Two typical joints between WCI and mild steel are shown in Figure 5.9. The stark difference between the microstructures of the samples soaked for 5 and 10 minutes is clear. The porosity that can clearly be seen at the interface of the 5 minute sample will result in poor bonding between the white iron and the steel substrate. It is probable that the porosity is due to oxygen from surface iron oxide on the substrate combining with carbon from the molten white iron to form carbon monoxide. These bubbles will be trapped at the interface if there is inadequate time for them to migrate to the exterior of the sample. However, after soak times of 10 minutes or longer, excellent bonding was exhibited with no cavities evident at the interface. In order to see if there was any residual oxygen at the interface, WDS

mapping was employed at the interface of the sample with a 10 minute soak time. No trace amounts of oxygen were detected and it is expected that any oxygen would have formed CO_2 with the abundant carbon in the liquid white iron and would have floated to the top of the casting. Also visible in Figure 5.9 is the interfacial layer, which is arrowed.

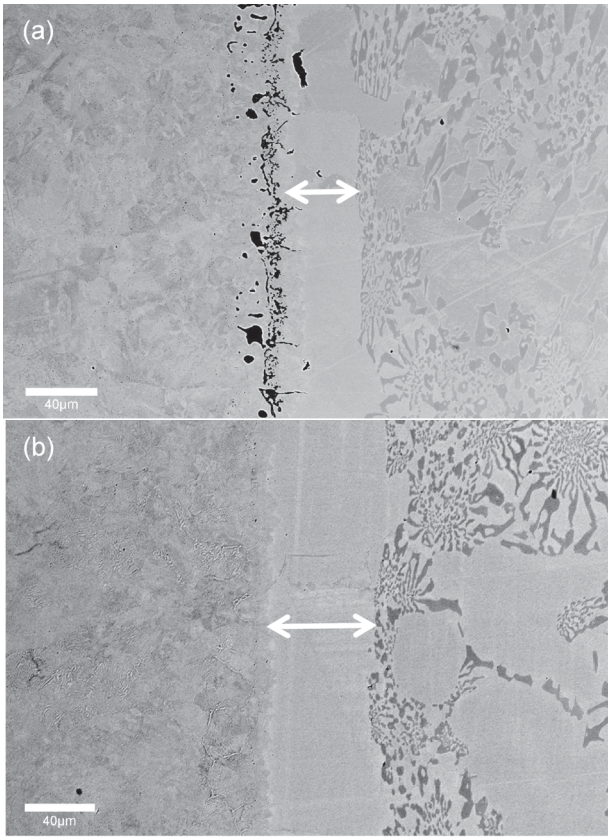

Figure 5.9: BSE images of: (a) Sample held for 5 minutes at 1250°C and (b) Sample held for 10 minutes at 1250°C. The arrows identify the interfacial layer. Steel substrate is to the left of the interfacial layer and the white iron is to the right. (HWOF = 337µm)

Having established that a minimum soak time was necessary, the next objective of the microstructural characterization was to determine the nature of the joint.

By employing a nital etching agent, the α ferrite was preferentially etched revealing the fine cementite in the pearlitic structure of the steel substrate close to the interface. Figure 5.10(a) reveals the extent of the carbide formation in the previously carbide-free steel substrate. It can be seen that close to the interface of the composite, the steel substrate is comprised of nearly 100% pearlite and the proportion of pearlite decreases further into the substrate. When the microstructure of the steel substrate is examined

more closely in Figure 5.10(b) it can be seen that coarse cementite has precipitated along the grain boundaries of the substrate and one grain boundary that extends to the interface of the substrate and the interfacial zone aligns with a grain boundary in the interfacial layer.

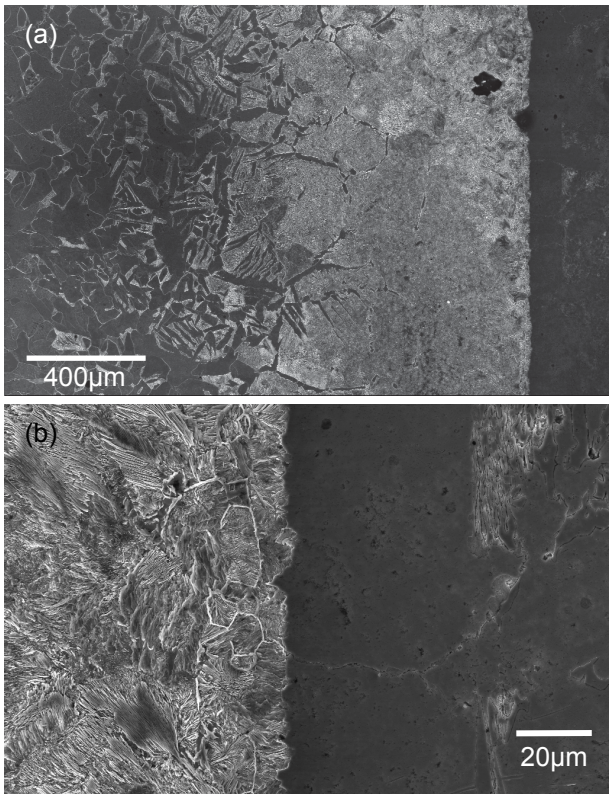

Figure 5.10: (a) Micrograph of interfacial region showing decreasing amount of pearlite (right to left) across the steel substrate (HWOF=2.04 mm) and (b) micrograph showing structure of pearlite in the steel substrate close to the interface. HWOF=153.3µm

Figure 5.11 shows backscattered electron (BSE) images of the interfacial region of samples cast for 5 to 25 minutes. As previously mentioned, porosity appeared at the interface of the sample cast for only 5 minutes. With all soak times of 10 minutes and greater, a good bond was established from an aesthetic point of view, with no porosity appearing at the interface. The microstructure on either side of the interfacial region appears to be largely consistent in all samples and there appears to be a trend of the interfacial region increasing in width with increasing soak time. It should be noted that differences in contrast between the images is due to varying processing conditions and not compositional differences.

The shading of all the interfacial regions appears to be similar to that of the matrix of the white iron indicating that these two regions may be similar in composition.

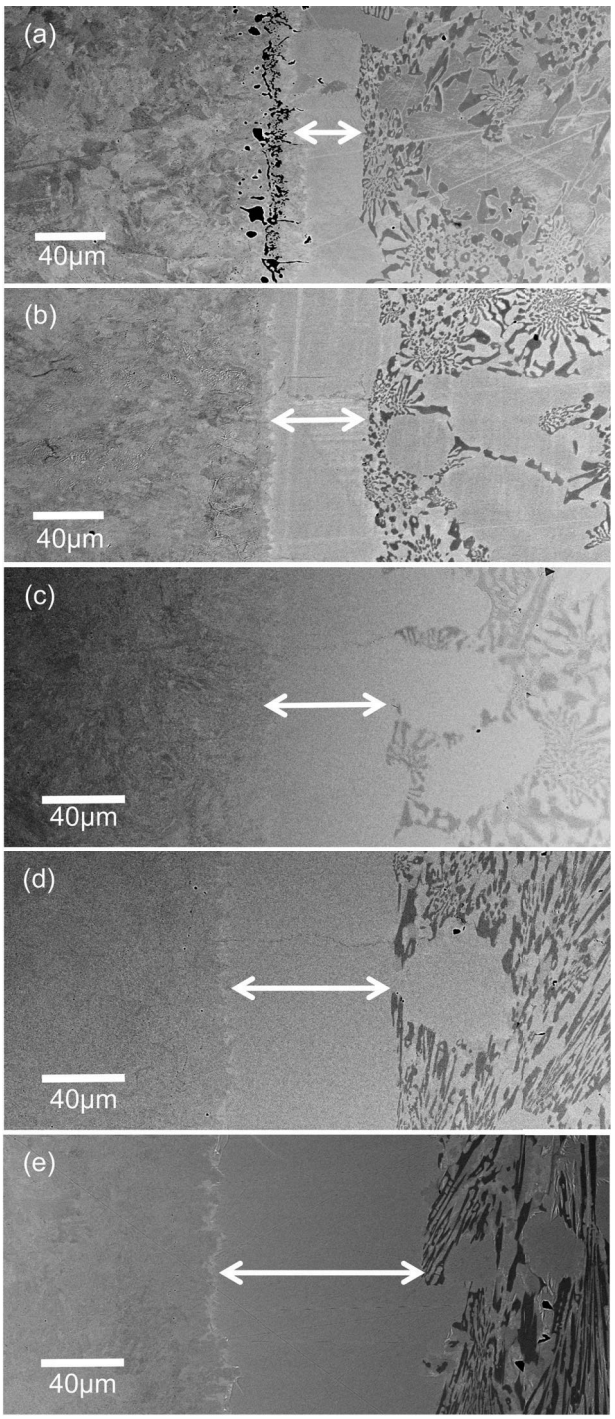

Figure 5.11: BSE images of interface in composites soaked at 1250°C for (a) 5 minutes, (b) 10 minutes, (c) 15 minutes, (d) 20 minutes and (e) 25 minutes with the width of interfacial region highlighted by arrows. (BSE imaging) (HWOF = 337µm)

It was found through the usage of electron backscatter diffraction (EBSD) that the interface layer was comprised of relatively large grains of retained austenite, Figure 5.12(a). Variances in colour indicate a difference in orientation based on the inverse pole figure (IPF) colouring scheme shown in Figure 5.12(c).

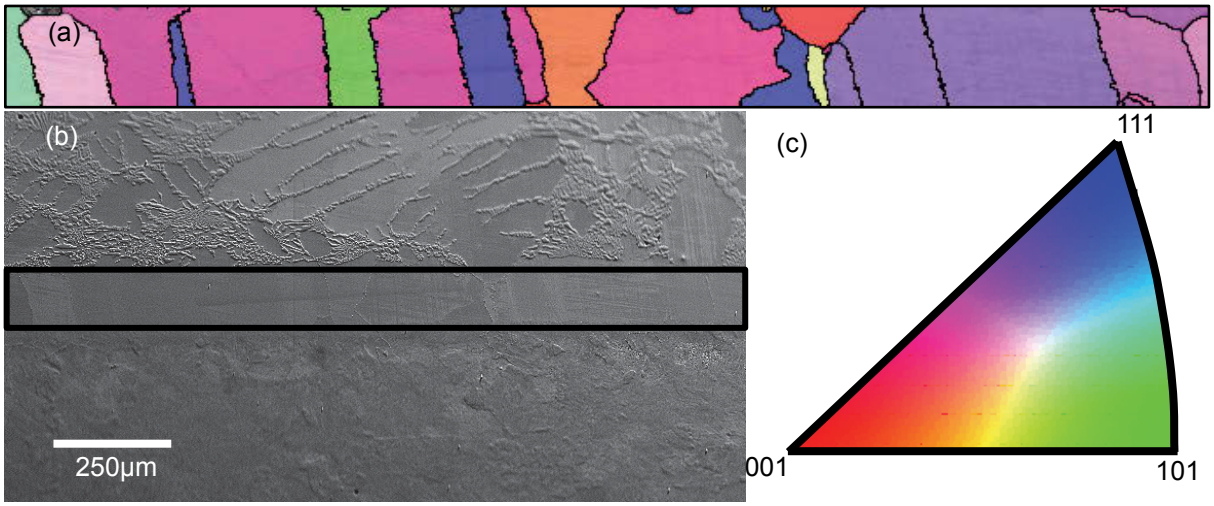

Figure 5.12: (a) EBSD map of interfacial region showing multiple austenite grains along the interface. The region where this map was taken is highlighted by the black box on the backscattered electron image (BSE) (b) Above this region is WCI, and below is steel. (HWOF = 1.5mm) (c) IPF colouring scheme of EBSD map.

The EBSD map shown above is comprised of approximately 25 grains of austenite and, based on the IPF colouring scheme shown in Figure 5.12(c), the majority of the grains seem to be purple-red in colour. At first sight, this may indicate a preferential growth direction of this interfacial region but there are also grains with very different orientation (green-yellow) dispersed throughout. Therefore it is believed that the high proportion of grains with similar orientation is not due to a preferential growth direction in this case, but is rather a sampling effect due to the small number of grains measured. Pole figures, produced by combining the EBSD data, are shown in Figure 5.13. The direction perpendicular to the interface corresponds to the centre of each diagram, and there is no special significance to the other geometric directions since the sample had radial symmetry in those directions. The data indicates that there is no particular texture with reference to the plane of the interface. The results must

therefore be interpreted as meaning that the solidification process produced a random orientation within the austenite interface layer.

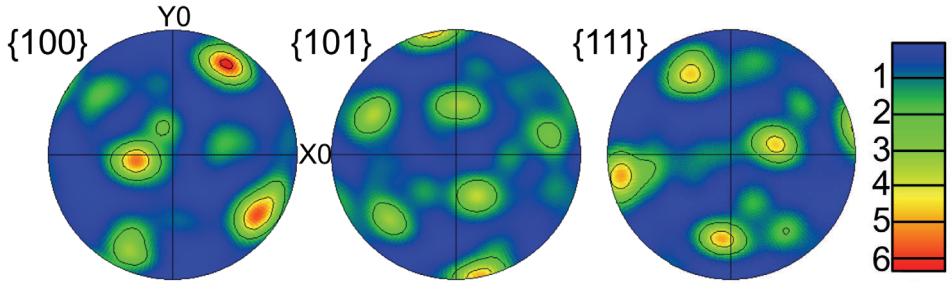

Figure 5.13: Pole figures of the austenitic interfacial region. There is no particular crystallographic texture and the maxima shown are generated by sampling issues since the section contained only about 25 austenite grains.

The chromium white cast iron solidified with the characteristic hypoeutectic microstructure of primary austenite dendrites and an eutectic mixture of M_7C_3 carbides and austenite. Phase identification was facilitated by EBSD and the M_7C_3 identified by its diffraction pattern and morphology. The region of the substrate immediately adjacent to the austenitic interfacial layer was found to consist of pearlite but the fraction of pearlite decreased with distance away from the interface as shown in Figure 5.10(a).

XRM has become a very useful tool for characterising the distribution of elements and phases in materials [90]. The elemental maps shown in Figure 5.14 show four quite distinct regions within this joint. On the left of the micrographs is the steel substrate, between the substrate and the interfacial layer is a diffusion affected zone, shown most clearly with the greyscale gradient across the Cr map shown in Figure 5.14(b). This zone will be investigated further in the next chapter. The interfacial region appears to have a similar composition to that of the matrix of the hypoeutectic white iron and the composition and structure of these regions are investigated further later in this section. The location of these regions is shown in Figure 5.15.

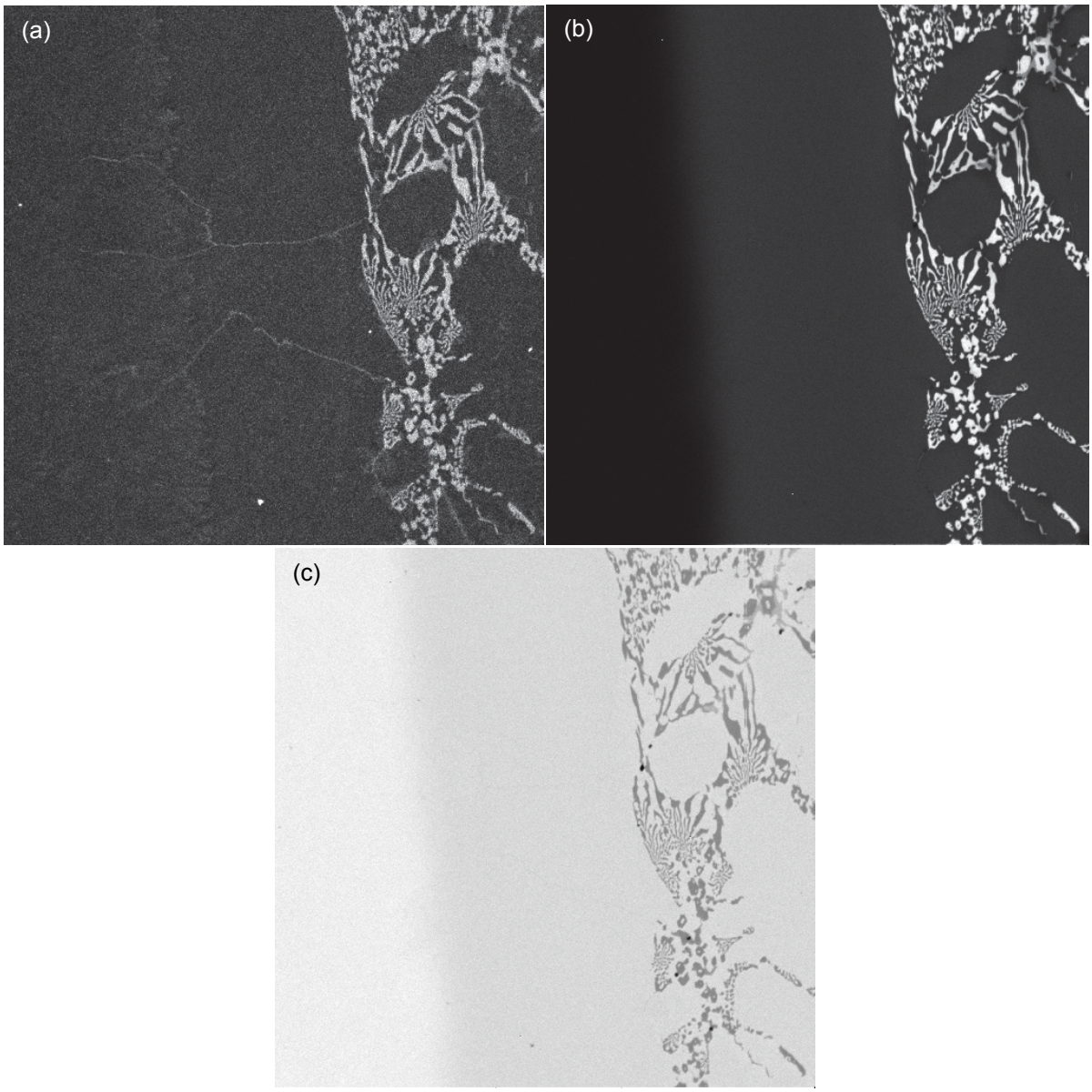

Figure 5.14: Elemental maps of the interfacial region. (a) Carbon, (b) chromium and (c) iron. HWOF=260μm

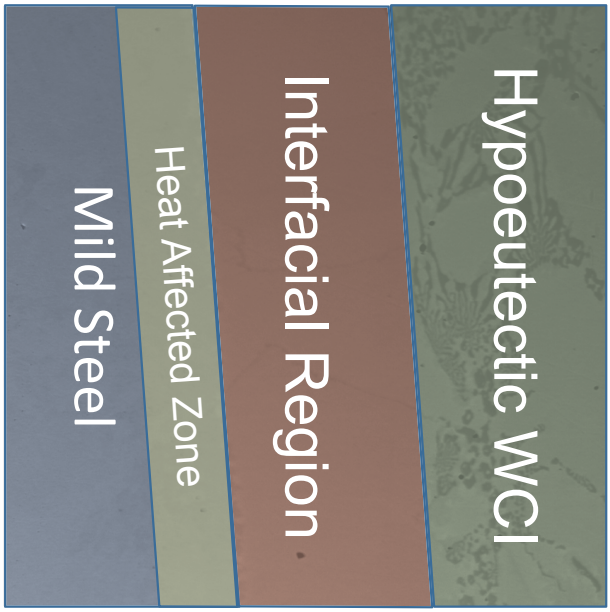

Figure 5.15: Micrograph highlighting the four zones at the join of this composite.

The composition of the interfacial region appears to be the same as that of the matrix of the white cast iron from these elemental images. Thin, string-like carbides seem to extend across the interfacial region and appear in the carbon map but not in the chromium map indicating that these carbides are of a different nature to that of the chromium carbides in the white iron. These same carbides that extend across the interfacial region also reside around the chromium carbides in the white iron. The Scheil diagram shown in Figure 5.16(b) shows the solidification path for this low melting point white iron and predicts the presence of these carbides.

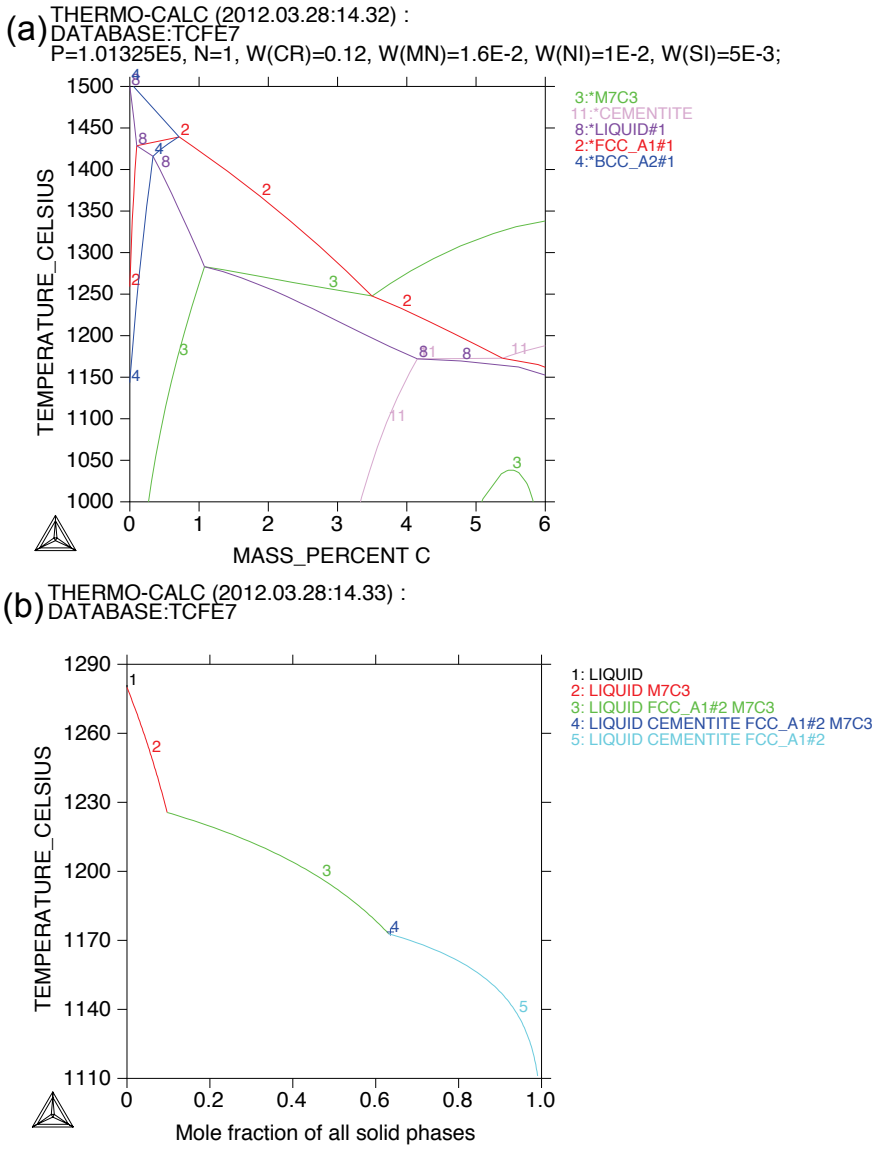

Figure 5.16: (a) Equilibrium phase diagram of Fe-12Cr-1.6Mn-1Ni-0.5Si-4.1C alloy. (b) Scheil diagram showing the solidification path of this alloy.

The Scheil diagram calculated using Thermocalc predicts that M_7C_3 carbides should solidify first (ie. the alloy is predicted to be hyper-eutectic) but this is due to Thermocalc's inaccurate representation of phases within the equilibrium phase diagram (Figure 5.16(a)) for the Fe-12Cr-1.6Mn-1Ni-0.5Si-C system. In fact, it has been shown through experimental measurement by Huggett [27] that the eutectic lies at 4.1 wt.% carbon with a melting point of 1209°C. Therefore, as discussed in chapter 1, the alloy is actually eutectic to hypo-eutectic in nature.

The Scheil diagram then shows eutectic solidification of both the M_7C_3 carbides and the FCC austenite phase. This is followed by a very short period of solidification of M_7C_3 carbides, austenite and cementite and finally austenite and cementite. Cementite is not as hard as complex M_7C_3 carbides and is thus undesirable in high wear applications. In this study this study a small amount of cementite is unavoidable due to the composition of the alloy but the formation may be minimised by rapid cooling of the composite post casting. However, care will have to be taken when cooling the composite rapidly so that large magnitudes of thermal stress are not generated.

The distribution and relative abundances of various elements can be illustrated in a high magnification image by assigning colours to elements of interest, creating a pseudo-coloured X-ray map identifying each phase by a different colour or shade, Figure 5.17. This makes XRM particularly useful for distinguishing the spatial distribution of specific elements and phases within a sample.

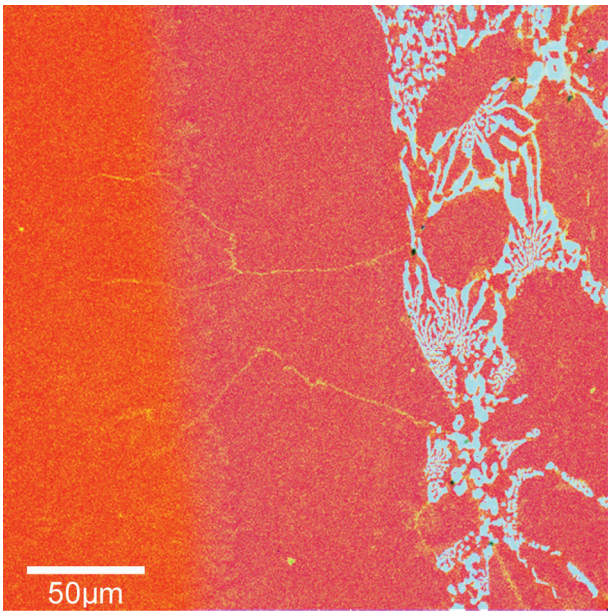

Figure 5.17: Pseudo-colour X-ray map of interfacial region. Iron is represented by red, chromium blue and carbon green. Sample had been soaked at 1250°C for 25 minutes (HWOF = 260µm).

Two-dimensional scatter diagrams, as shown in Figures 5.18(a)-(c), show pixel frequency versus element concentration within a given field of view, and are plotted against each other for selected elements within the sample. Thermal colouring adds a

third dimension to these diagrams by indicating the number of points on the diagrams with the indicated elemental concentrations. From these scatter diagrams, nodes corresponding to different chemical phases may be identified [91]. Identification of the phases is facilitated by mapping the data back onto the micrograph to construct a chemical image of the specimen, Figure 5.19. It is clear that the two distinct nodes in Figure 5.18(a)-(c) correspond to α-phase and γ-phase, while the diffuse streak is associated with diverse measurements made on the γ+carbide eutectic. It is also apparent that the austenite of both the cast iron and interfacial layer is rich in Cr, Table 5.2, and evidently formed by growth out of the cast iron melt. The high alloy content of this austenite has evidently suppressed the martensitic transformation temperature to below room temperature.

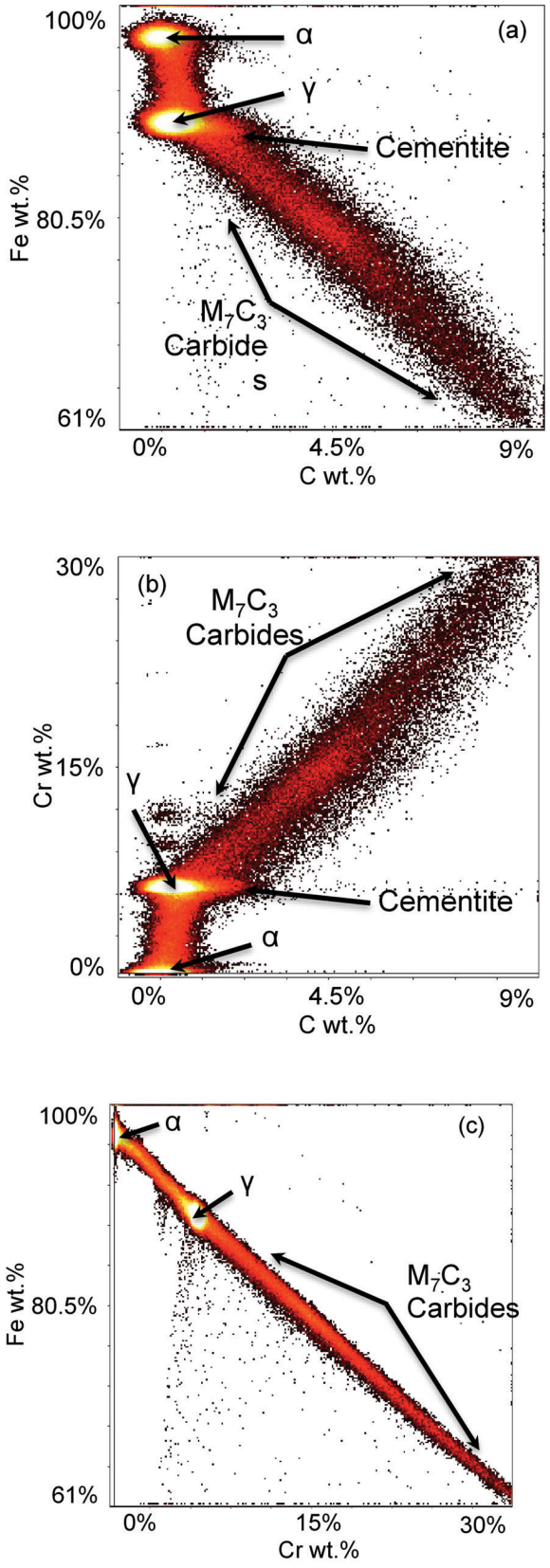

Figure 5.18: Scatter diagrams showing the concentration dimensions of various phases within the interfacial region of these composites. Sample had been soaked at 1250°C for 25 minutes.

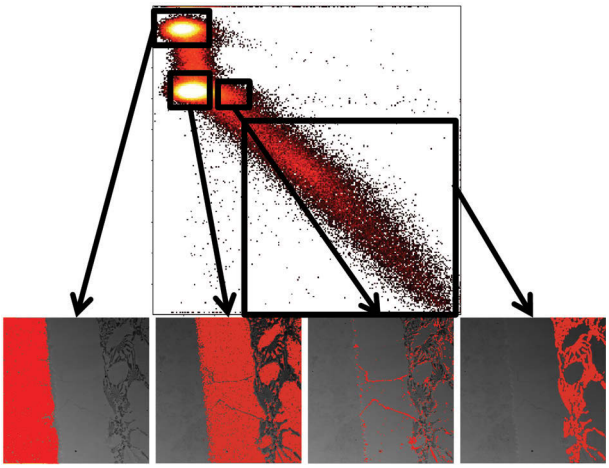

Figure 5.19: Selection of nodes within scatter diagram and overlay of selected region on BSE image. Sample had been soaked at 1250°C for 25 minutes.

When these nodes are selected, chemical data may be extracted and the composition of each phase can be found. Table 5.2 displays the composition of the major phases comprising the interfacial region.

TABLE 5.2. COMPOSITION OF AUSTENITE, FERRITE AND M_7C_3 CARBIDES IN MICROSTRUCTURE PRODUCED BY 25 MINUTE SOAK AT 1250°C. ALL COMPOSITIONS ARE QUOTED IN MASS PERCENT.

Phase	Fe	Cr	C	Ni	Mn	Si
Ferrite	98.1	0.1	0.3	0.5	0.3	0.2
Austenite	90.2	5.5	0.6	1.5	1.3	0.7
M_7C_3	60.6	28.0	8.6	0.6	1.7	0.2

EBSD maps were also taken of this same area in the interfacial zone and the corresponding map is shown in Figure 5.20(b). From this map we can see a difference in crystallographic orientation of the grains either side of the string-like carbides

extending across the interfacial region. In this map both austenite and M_7C_3 grains are coloured based on the inverse pole figure colouring scheme shown in Figure 5.20(c).

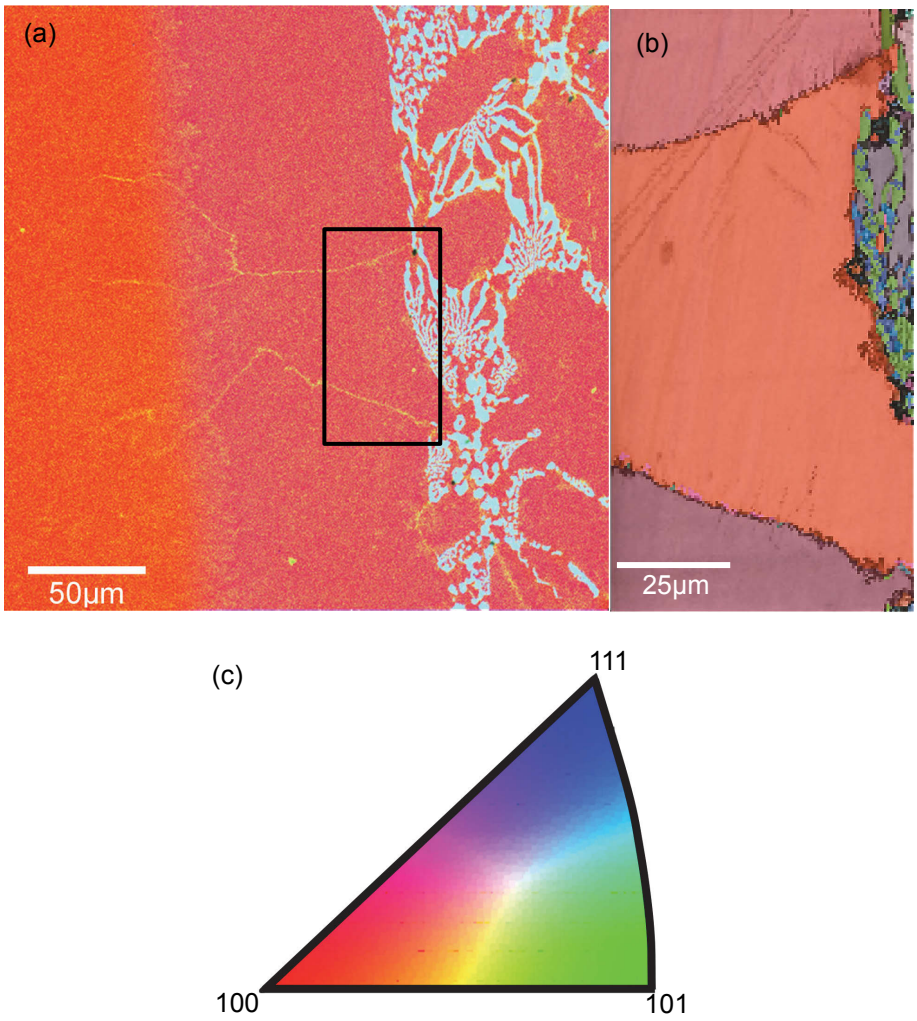

Figure 5.20: (a) Pseudo coloured X-ray map of interfacial region with area examined using EBSD highlighted. (HWOF = 260µm) (b) Shows EBSD map of interfacial region directly adjacent to the white iron wear layer. (HWOF = 66µm) Colouring is based on the inverse pole figure colour sheme shown in (c).

From the X-ray mapping that has been performed and the solidification pathway simulation, it can be assumed that the carbides residing along the grain boundaries are cementite but in order to confirm this, a high magnification EBSD map was taken at the grain boundary of two austenite grains lying within this interfacial region (Figure

5.21(a)). Figure 5.21(b) shows the Kikutchi pattern of the carbide residing along the grain boundary and it matches with that of Fe_3C.

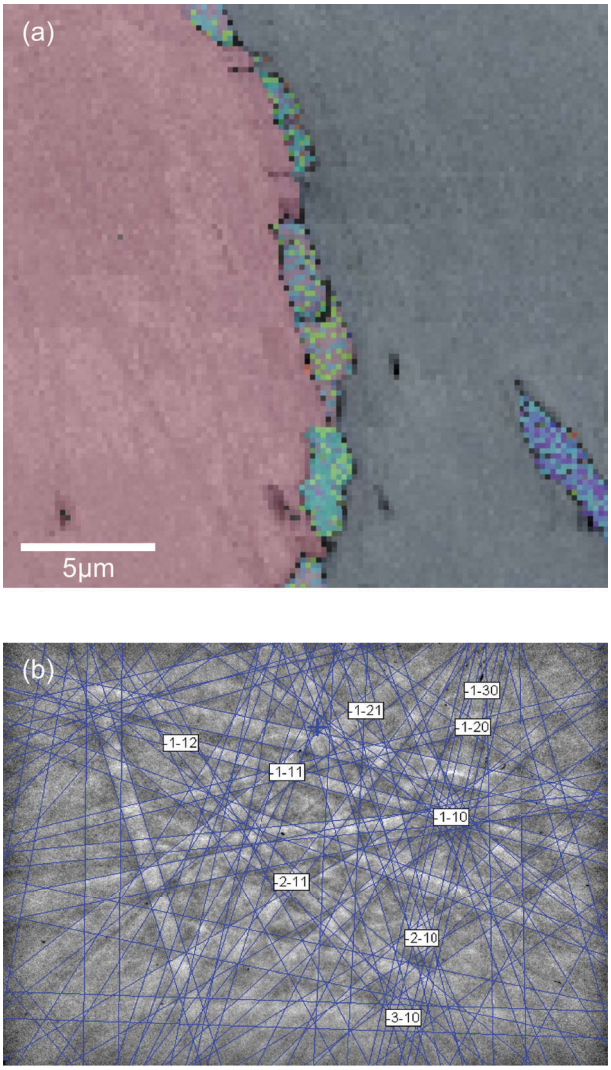

Figure 5.21: (a) EBSD map of carbides (center) residing along the grain boundary of austenite grains on the left and right hand sides of the image. (HWOF = 23.6μm) (b) Kikuchi pattern of Fe3C (Space Group 62) found along the grain boundaries.

In order to gain a better understanding of the growth processes occurring at the interface, relatively dense NbC particulates were added to the melt to assess the state of each region at the soak temperature of 1250°C. It was believed that if the interfacial layer was once in a liquid state NbC particulates would be expected to be found within this layer.

From Figure 5.22 it can be seen that the carbides have settled in the melt of a sample with a soak time of 15 minutes. The carbides were initially homogeneously dispersed through the button created in the argon arc furnace due to the large amount of turbulence created by the argon arc furnace and also the rapid cooling due to the water chilled copper base. The button was then placed in the mild steel cup and, as it became molten, the carbides began to settle due to the difference in density. It can be seen that the area at the top of the micrograph possesses no NbC particulates as they have all settled toward the steel substrate located at the bottom of the micrograph.

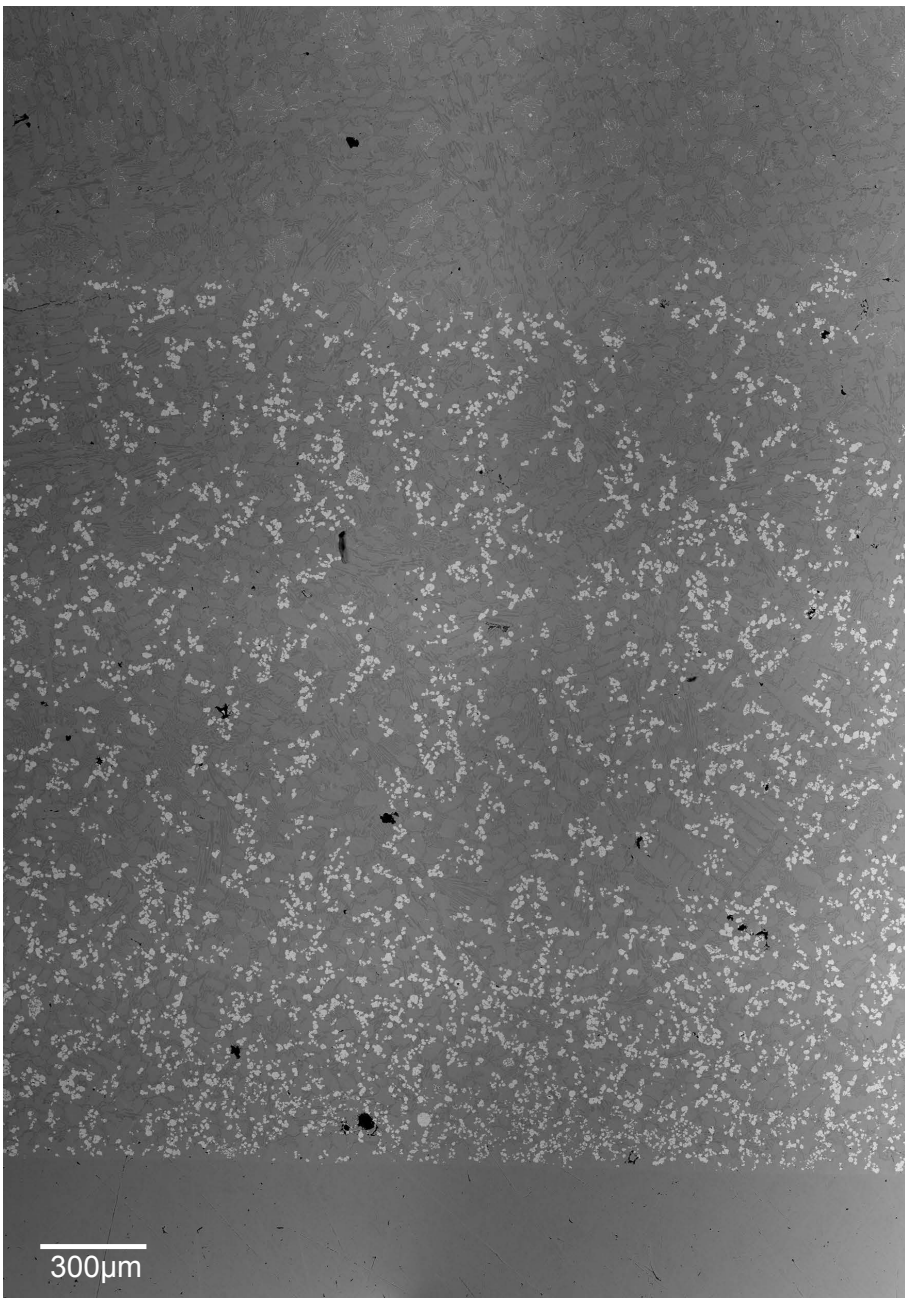

Figure 5.22: Settling of NbC in kiln cast steel white iron composites. (HWOF = 2.85mm)

The pseudo-coloured X-ray map shown in Figure 5.23 shows the location of the NbC particulates within the interfacial region of the composite. It can be seen that the particulates have settled into the interfacial region. This indicates that this region was once in the liquid phase and either formed at high temperature or upon cooling.

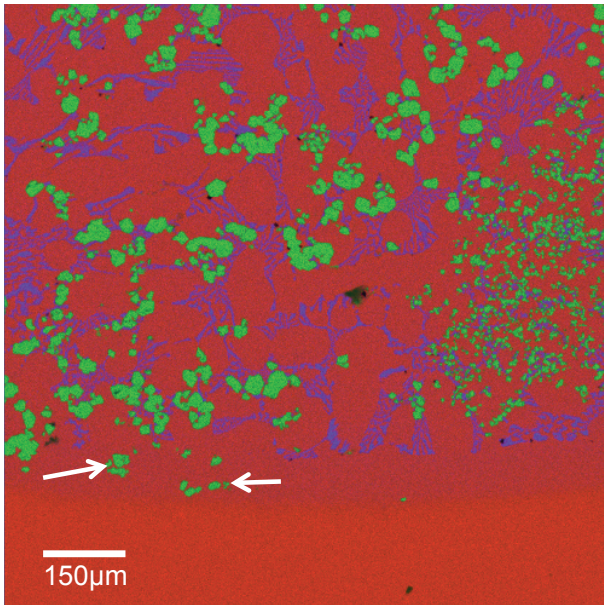

Figure 5.23: Pseudo-coloured X-ray map of interfacial region with NbC added. Nb is coloured green in this micrograph with Fe red and Cr blue. NbC particulates can be seen within the interfacial zone (arrowed). (HWOF = 1.5mm)

Nano-indentation profiles were taken across the interfacial region of all samples cast between 10 and 25 minutes and these line profiles are shown in Figure 5.24. These nano-indentation line profiles have been graphed with the point at which the interfacial region changes from the epitaxially grown austenite layer to the pearlitic substrate located at $x = 0$ in order to assist in highlighting the growth of this interfacial region.

Each line profile is comprised of a relatively low hardness pearlitic substrate shown at the left. The hardness then increases as the proportion of pearlite increases and then sharply drops off as the indentor strikes the interfacial region. This transition is clearly identified in all samples and the hardness appears to be relatively constant across this region. Thereafter, the hardness sharply increases whenever the indenter strikes the

M_7C_3 carbides, but decreases whenever a measurement is made of the matrix of the white iron.

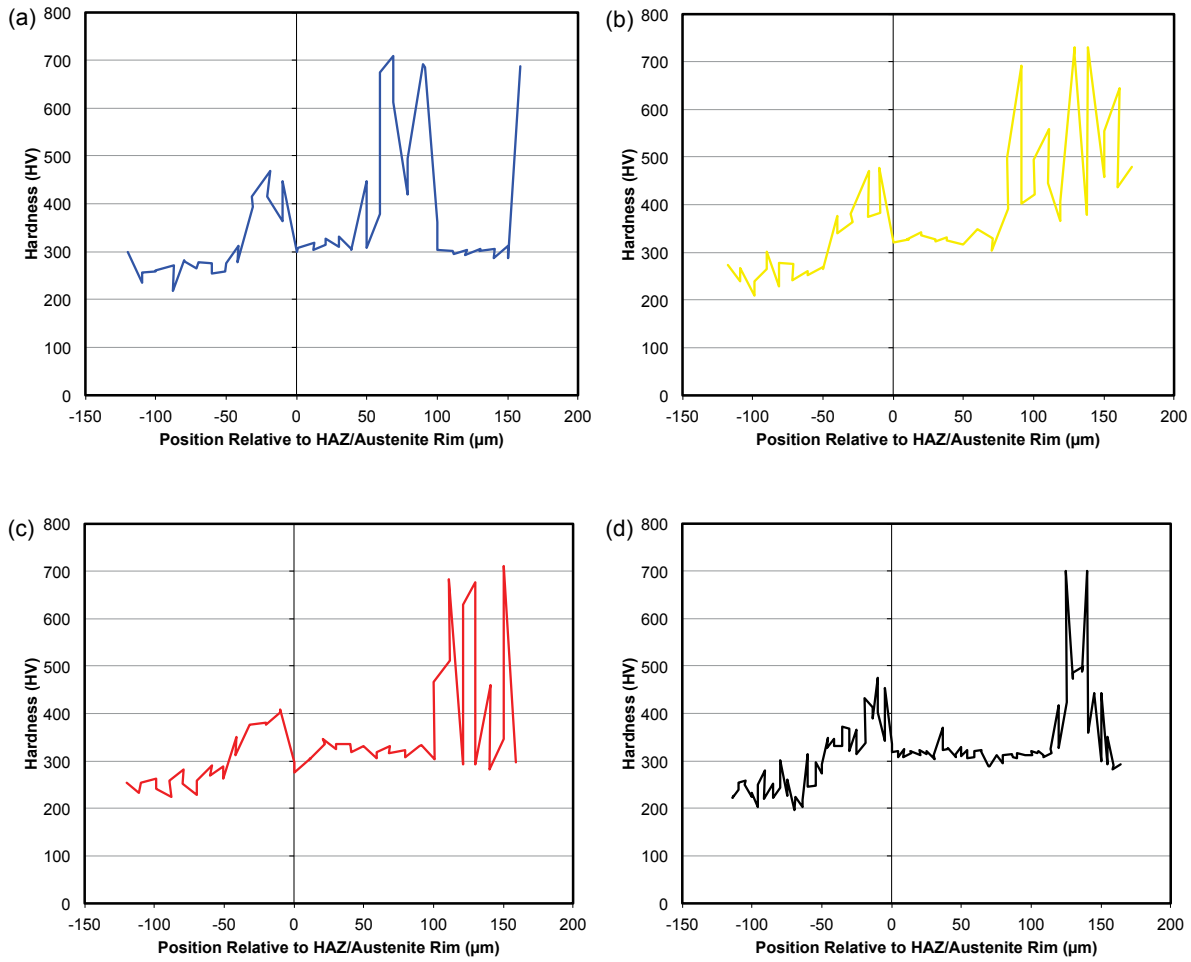

Figure 5.24: Nano-indentation profiles across the interfacial region of composites cast showing comparative hardness for (a) 10 minutes, (b) 15 minutes, (c) 20 minutes and (d) 25 minutes.

The facts that (i) X-ray mapping indicated that the interfacial region has a composition very similar to the austenite in the matrix of the white iron, (ii) the hardness of the interface is similar to that of the austenite of the white iron, and (iii) the dense NbC particulates became occluded this region prove that it was once in the liquid phase. Therefore, this region was created from the liquid white iron and not due to modification of the steel substrate by inward solid state diffusion of elements.

Using all the techniques mentioned previously including X-ray mapping, BSE imaging and nano-indentation, the growth rate of this interfacial layer was identified and the results obtained are shown in Figure 5.25. It was found that the interfacial layer grew at a rate of approximately 6 μm per minute at 1250°C, with an approximately linear relationship. It is believed that this rate of interfacial growth would increase with soak temperature due to the increased rate of diffusion of atoms across the interface. Diffusion across the interface is discussed in greater detail in the next chapter.

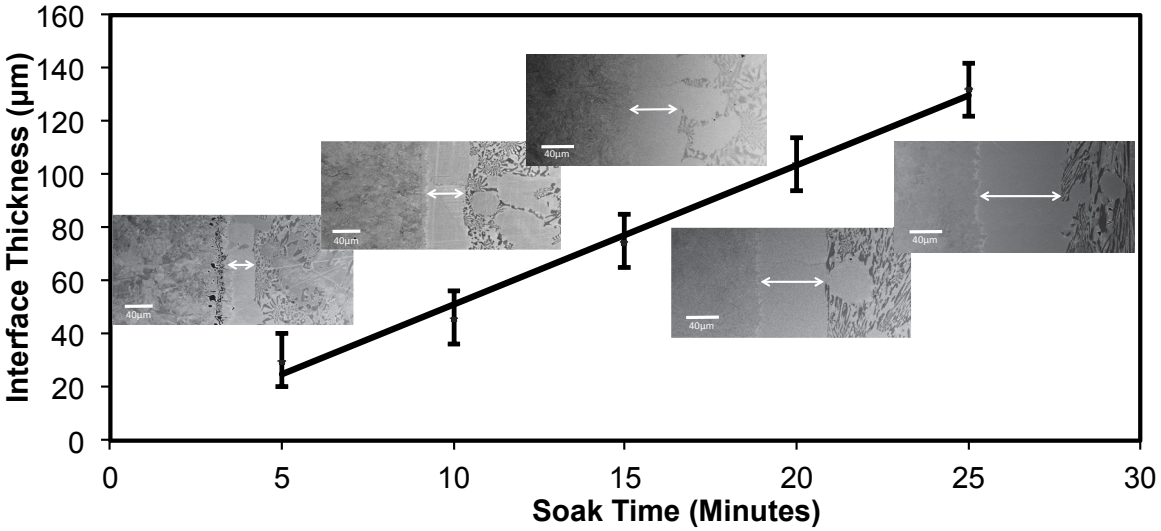

Figure 5.25: Interfacial growth respective to soak time.

5.3.2 – High Temperature Confocal Laser Scanning Microscopy

In order to gain a better understanding of how this interfacial layer grows, HTLSCM was employed to follow the development of the interfacial boundary, *in-situ* during heating of the composite at 1250°C.

Please note, images in Figure 5.26 show the white iron on the left and steel substrate on the right, which is the opposite of how samples are displayed elsewhere in the chapter. Figure 5.26(a) shows the starting microstructure of the white iron/steel composite before the white iron has been cast onto the steel substrate. The vertical striations on the steel are tool marks from the low speed diamond saw used to cut the sample. The dotted white line running down the middle of the micrograph indicates the location of

the interface between the two materials. The interface changes location throughout the series of photos but this is due to the thermal expansion of the alumina rod suspending the sample in the middle of the furnace chamber and the operator attempting to keep it in the middle of frame.

In Figure 5.26(b), the eutectic carbides are becoming quite obvious as the white iron transforms from austenite + M_7C_3 + Fe_3C to austenite + M_7C_3. From Figures 5.26(d-f), it can be seen that the white iron is being transformed into the liquid phase. The liquid white iron appears dark due to the shape of the liquid meniscus not reflecting light back to the camera. When the sample became fully molten, it slightly wetted the surface of the mild steel, obscuring the interface between the two materials. When the molten white iron comes in contact with the mild steel substrate, it would be expected that carbon diffuses into the steel due to the concentration gradient between the two materials. This is most likely the explanation for the decrease in the melting temperature of the substrate as shown in Figure 5.27(a). Simultaneously the molten white iron is partially dissolving the steel substrate. In turn, this causes iron from the substrate to transfer into the boundary layer of the melt. Figures 5.26(h-l) shows this interfacial layer forming with the layer showing an increase in thickness with increasing soak time. The growth front appears to be planar and grows at a constant rate. A small undissolved oxide moved around the surface of the melt and came to rest on the growing interfacial layer. The oxide is pushed into the melt by the growing layer but is eventually overtaken and captured by the layer.

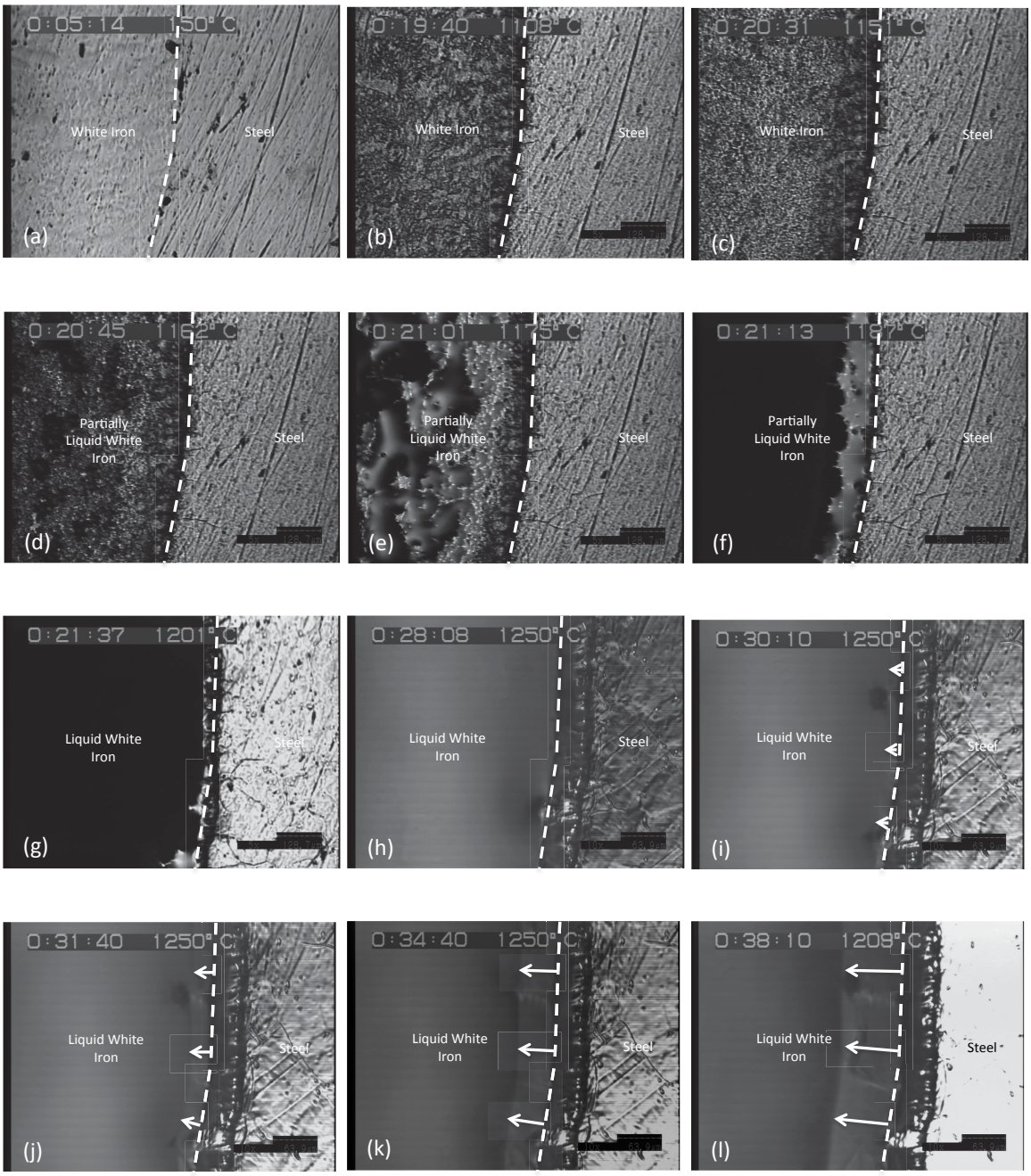

Figure 5.26: (a-f) Shows the original interface of the interference-fitted sample indicated by the dotted white line. The sample is heated and the white iron is transformed into its liquid state. No heat treatment has been applied to this sample. (g) White iron has become completely liquid. (HWOF = 910µm) (h) At a higher magnification it can be seen that the liquid white iron has partially wetted the surface of the steel and has obscured the original surface of the steel but the location of the interface is identified by the white dotted line. (i-l) The interface can be seen growing into the liquid white iron with the arrows indicating the direction of interfacial growth. (HWOF = 485µm)

As localized carbon levels in the liquid white iron around the interface decrease due to both transfer into the substrate and dilution by the molten substrate material, the melting point of the alloy directly at the interface increases as shown in Figure 5.27(b). When the carbon content decreases to the extent where the liquidus rises above 1250°C, a layer of austenite will begin to grow and this process will continue, increasing the thickness of this newly formed layer, until diffusion of carbon from the white iron into the mild steel is stopped.

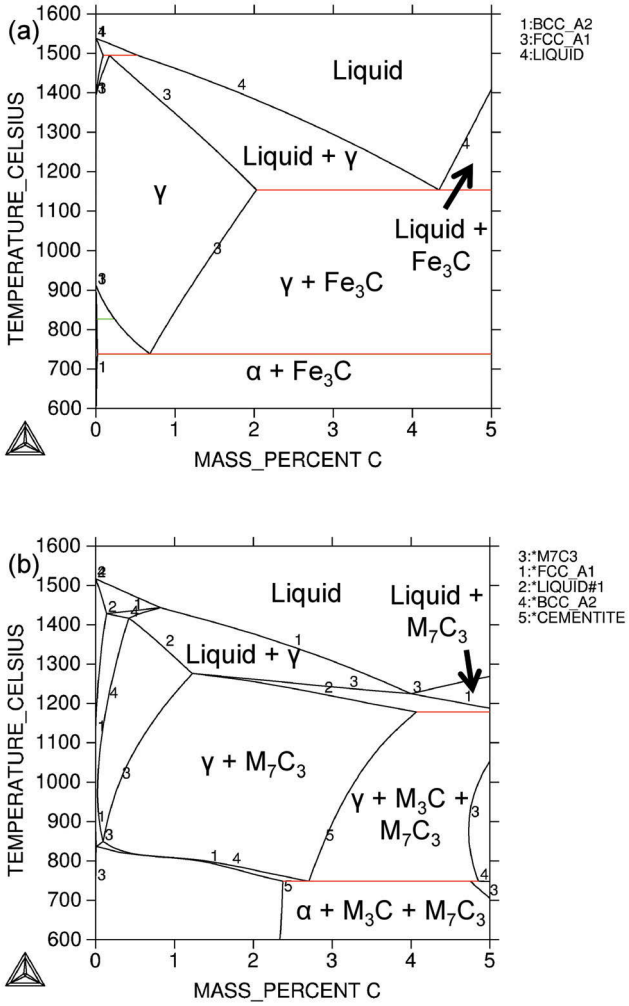

Figure 5.27: (a) Iron-carbon metastable phase diagram [92] and calculated phase diagram of low melting point white iron. (b) Fe-12Cr-C phase diagram. Liquidus is shown to increase as carbon content decreases from eutectic composition of 4.1% [27].

In order to further illustrate the mechanism by which this interfacial layer forms, Figure 5.28 shows the phase formation at 1250°C as the mild steel is introduced through

dissolution into the white iron as calculated by Thermocalc. It can be seen that after the mass fraction of steel added exceeds approximately 15%, austenite begins to form and the volume of liquid metal decreases.

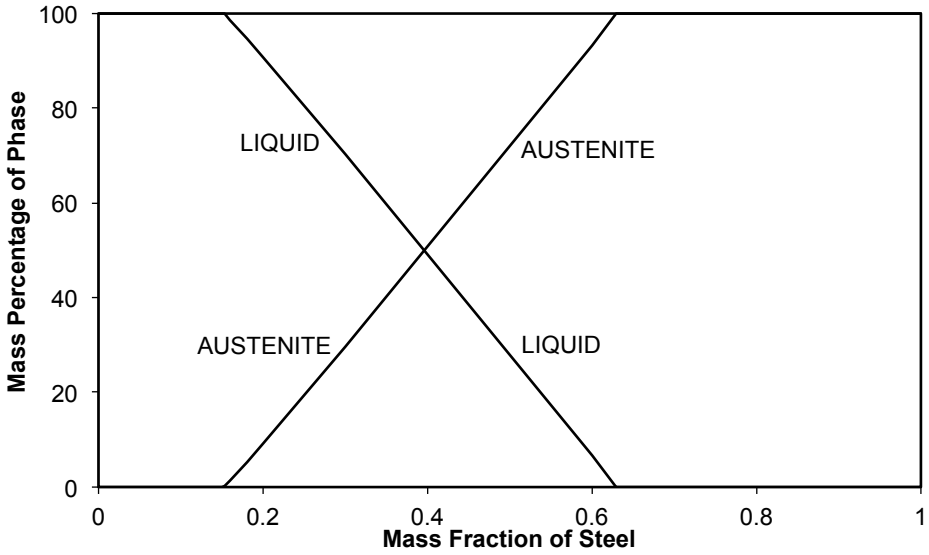

Figure 5.28: Volume percent of phases at 1250°C with increasing mass fraction of steel.

Figure 5.29(a) shows the surface of the disc-shaped sample after the white iron has been cast onto the steel and the liquid white iron has solidified. On the right hand side of the micrograph is the steel substrate. The interfacial layer can be seen inside this and then the white iron layer. The white iron layer appears to be covered in long, acicular carbides, with some of these carbides actually growing out on top of the steel substrate. These carbides have grown due to the carbon content in the liquid white iron being slightly less than the eutectic composition, thus when the material solidified, the austenite formed first creating regions higher in carbon as the austenite can only retain a certain amount of carbon. This high carbon solution then solidified as a hypereutectic, forming a dense layer of carbides as shown in Figure 5.29(b).

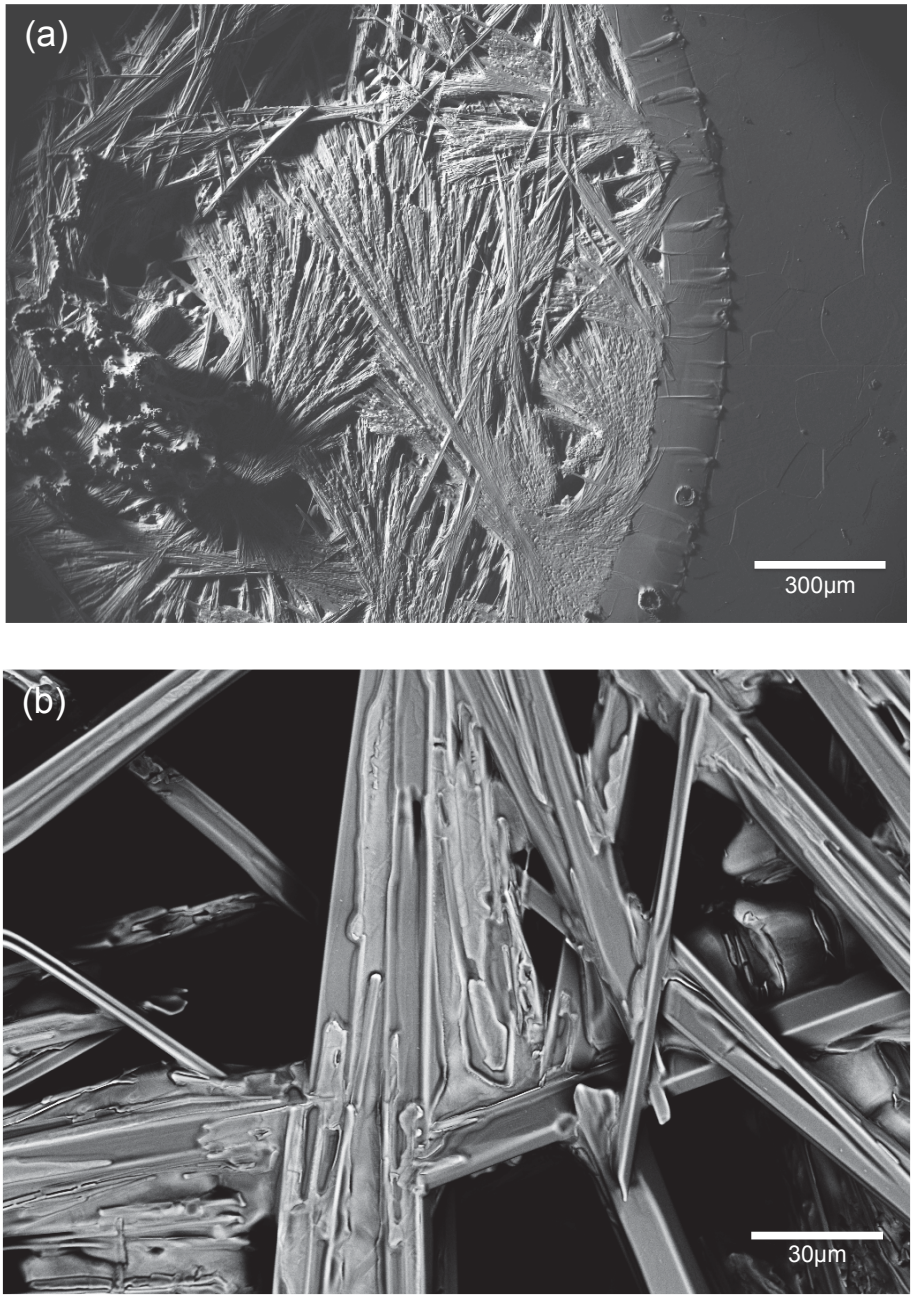

Figure 5.29: (a) Secondary electron image of the surface of a sample after heating in the confocal microscope. HWOF=2mm (b) High magnification image of carbides that have solidified at the surface of the white iron. (HWOF = 200µm)

Solid state diffusion is relatively slow when compared with the diffusion of the carbon atoms in the liquid phase so it was believed that there would be a concentration gradient of carbon across the interfacial region. This was analysed quantitatively using WDS mapping, Figure 5.30. The question of diffusion will be discussed further in the following chapter. In Figure 5.21, it can be seen that, while there is no significant

variance in carbon concentration across the interfacial region, there appears to be a high concentration in carbon along the grain boundaries of the interfacial austenite. This carbon residing along the grain boundaries was found to be in the form of Fe_3C. This Fe_3C would have precipitated at the grain boundaries during cooling after the soak. It can be seen that this grain boundary film of Fe_3C extends about 50 μm into the substrate. Therefore, at the soak temperature this part of the substrate was also austenitic, as would indeed be expected from the phase diagram (Figure 15(a)) for a material of Fe-0.6%C content. Since the grain boundary is continuous across the interface it can be deduced that the austenitic interfacial layer grew epitaxially on the lower carbon austenitic layer of the substrate. However, after cooling to room temperature the lower carbon austenite of the substrate formed pearlite.

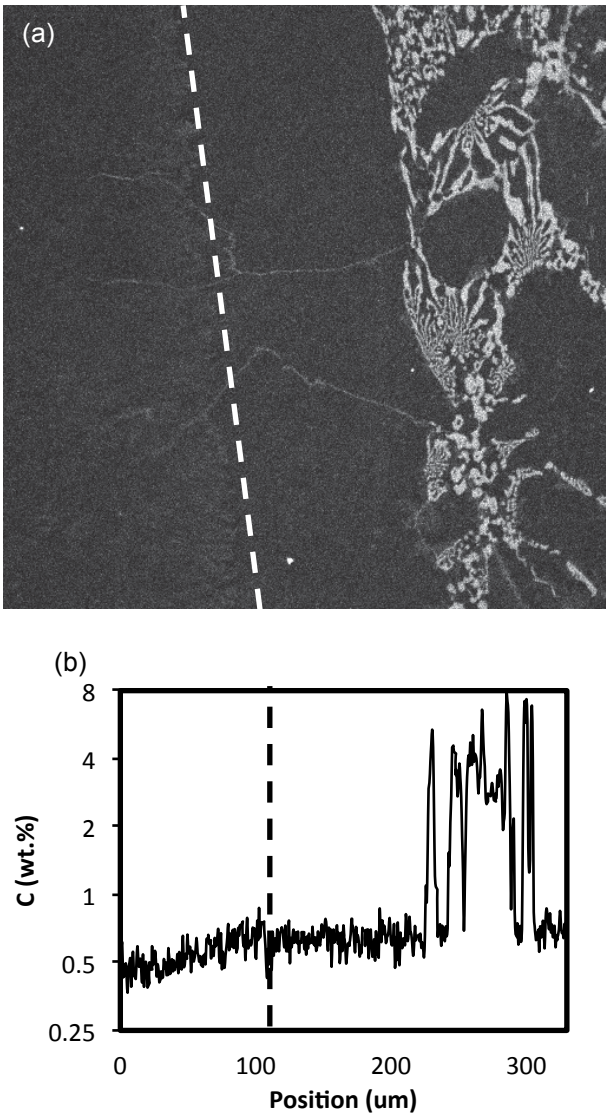

Figure 5.30: (a) Carbon map of interfacial region. Greyscale is based on carbon concentration with carbon levels above 8wt.% shown as white and below 0.2wt.% black. (HWOF = 260μm) (b) Average carbon contents as a function of position. Dotted lines indicate the transition from interfacial layer to the steel substrate. Note, vertical scale is logarithmic.

The carbon map shown in Figure 5.30 shows precipitation of Fe_3C carbides at the grain boundaries in this interfacial layer with the grain boundary providing a nucleation site for the growth of the carbide. In the HTCLSM micrograph shown in Figure 5.31 precipitation of carbides from the newly formed austenite layer are seen at the surface, most likely at grain boundaries or other lattice defects. These small carbides appear as small spots on the micrograph.

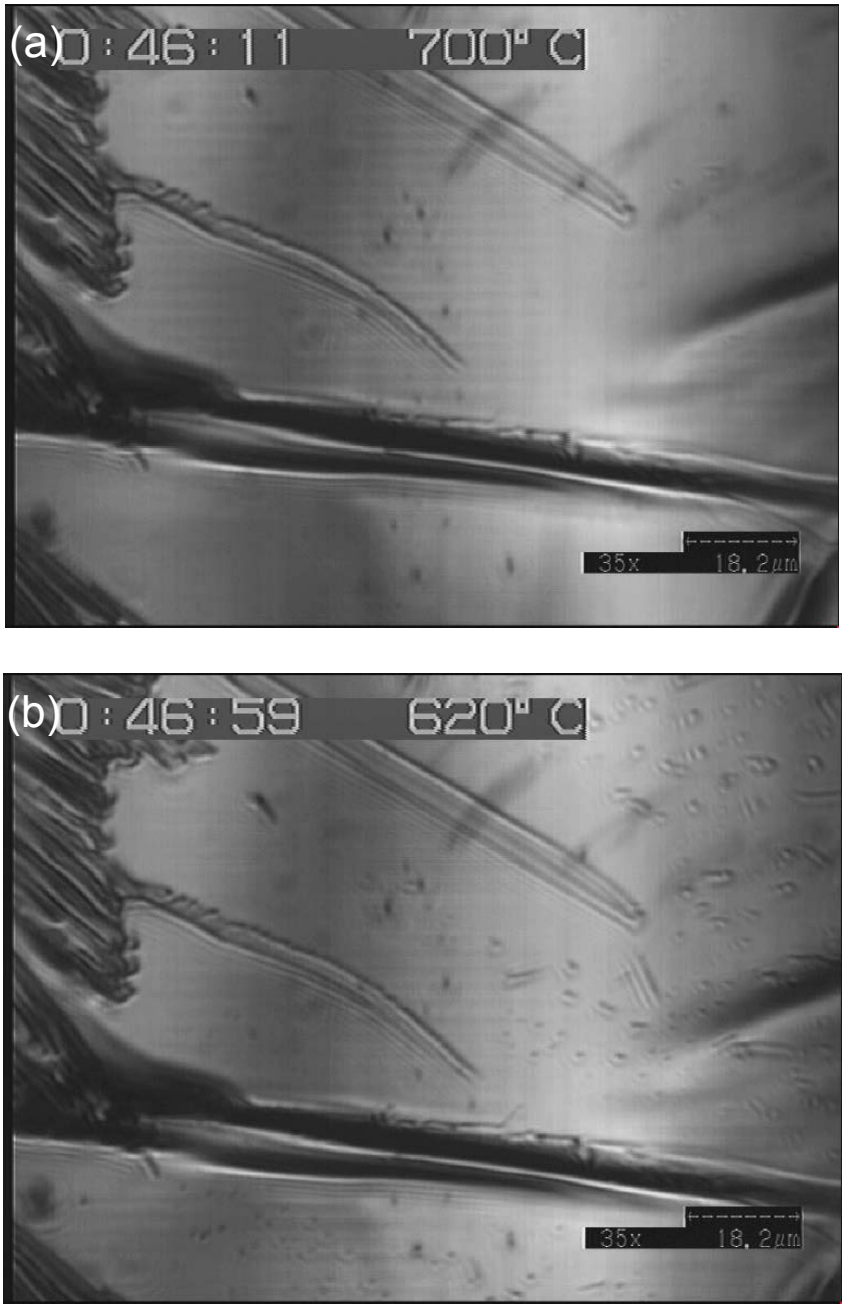

Figure 5.31: (a) High temperature laser scanning micrograph of interfacial region after solidification of the liquid white iron. The carbides that have solidified at the surface of the melt have grown over the surface of the interfacial region on the left hand side of the micrograph. (b)After the temperature has dropped below 700°C, carbides begin to precipitate in this layer as the austenite layer becomes unable to retain the carbon. (HWOF = 130μm)

In Figure 5.32 a high magnification scanning electron micrograph is shown of these precipitated carbides. This image also shows that the austenite layer grew in thin layers.

Although the deposition of austenite is caused by the combined effects of localized depletion of carbon and increase in iron content causing the melting point of the melt directly adjacent to the solid substrate to increase, it is not clear why this process should be intermittent. As such the presence of the layers was unexpected. It can be seen that the carbides appear to have nucleated along these planes.

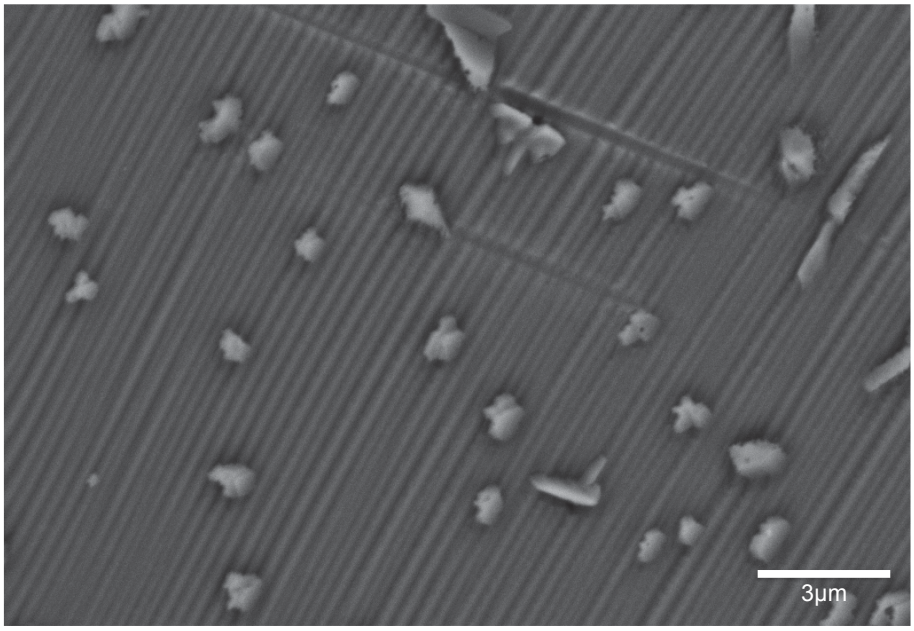

Figure 5.32: High magnification image of the surface of the confocal specimen. Small Fe_3C carbides have precipitated. (HWOF = 20.2µm)

5.3.3 – Mechanical Testing

Finally, in order to assess how these composites perform when placed under stress, three-point bend testing was carried out on cylindrical composites prepared as described earlier. The load was applied at the interface of the two materials.

These tests showed that the maximum three-point flexural load that these 4 mm diameter, rod-shaped composite samples could experience was ~800-1000N. It was found that all samples broke within the white iron region of the composite sample and thus the load vs. displacement curves shown in Figure 5.32 all exhibit a sharp decrease is flexural load due to the brittle fracture mode of the white iron. No trend can be seen

with increasing soak time and the maximum flexural load is very similar to that of the plain low melting point white iron samples shown in Chapter 2.

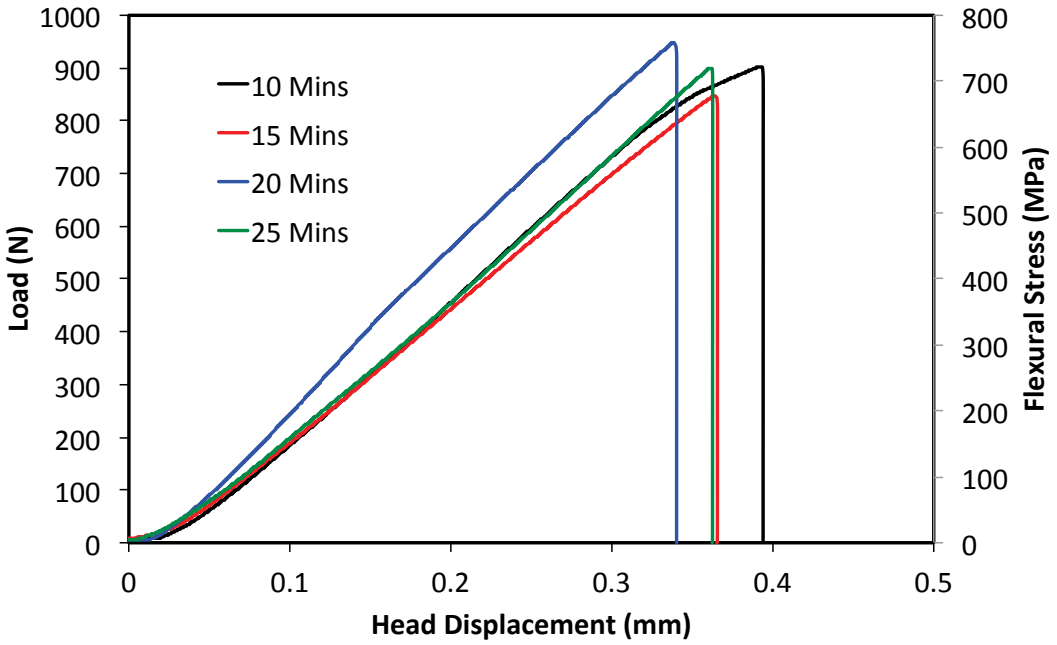

Figure 5.33: Load and flexural stress vs displacement curve for 4 mm diameter, rod shaped composite specimens with varying soak times.

It can be seen in Figure 5.33 that the maximum flexural stress or modulus of rupture exhibited by these test specimens is ~650-800MPa.

From these test results it can be deduced that all samples failed within the white iron region of the composite. The thickness of the interfacial region had no effect on the flexural strength of the white iron/steel composite. Figure 5.34 shows the fracture surface of one of these test specimens. It can be seen that the material exhibited a brittle fracture mechanism.

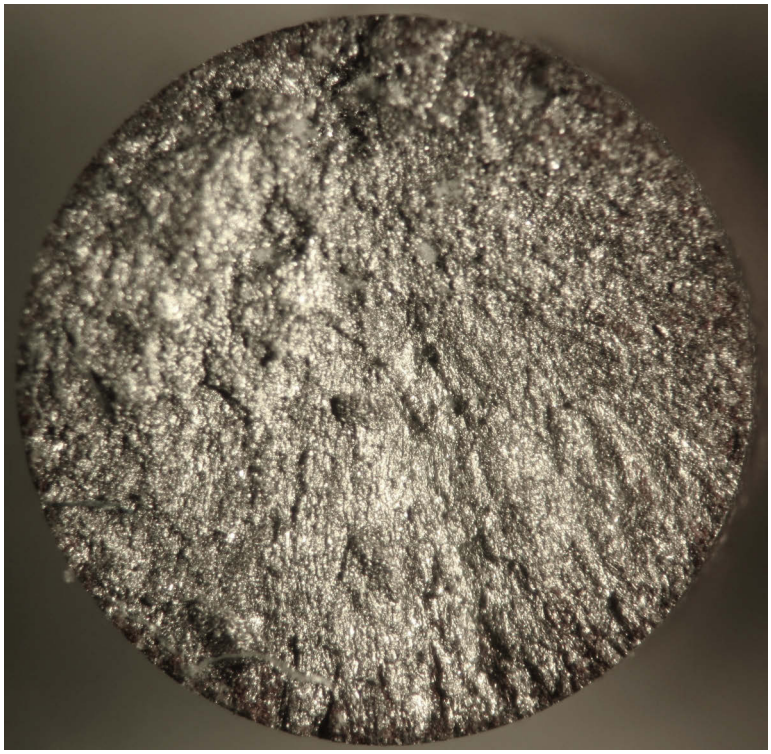

Figure 5.34: Fracture surface of specimen after three point loading. Fracture surface is located in the white iron region of the test specimen.

5.4 – Chapter Conclusions

In this study, the interface formed during the kiln casting of white cast iron onto a mild steel substrate has been investigated as a function of soaking time. Soaking the composite at 1250°C for 10 minutes or longer eliminated porosity on the interface, because it provided time for any carbon monoxide bubbles formed to migrate out to the free surface of the composite through the still molten liquid cast iron. An austenitic interfacial layer was found to develop between white iron and the steel, by epitaxial growth from the melt onto the austenite of the substrate. This layer was retained to room temperature due its high degree of alloying, but the austenite of the substrate reverted back to a ferrite plus pearlite mixture.

Through the usage of combined EDS and WDS X-Ray mapping, qualitative and quantitative data was obtained showing spatial distribution and chemical composition of the various microconstituents. The thickness of this interfacial layer was measured

using both *ex*- and *in-situ* techniques and it was found that this interfacial layer grew linearly with soak time.

In order to confirm these findings, high temperature laser scanning confocal microscopy was employed to examine the formation of this interfacial layer *in-situ*. This technique confirmed a seven-stage process is occurring in the creation of these composites.

1. Melting of the white iron .
2. The liquid white iron partially dissolves the steel substrate.
3. Iron from the substrate transfers into the liquid cast iron while a counter-current diffusion of the carbon from the cast iron occurs into the substrate. This results in a localized increase in iron and decrease in carbon in the liquid cast iron at the interface.
4. Both compositional changes drive an increase in the melting point of the liquid close to the interface and, once sufficient dissolution of the substrate has taken place, growth of a rim of austenite occurs.
5. From this point onwards a planar growth front of austenite continues to grow in a linear fashion in a direction orthogonal to the substrate. A carbon concentration gradient exists between the liquid white iron and the steel, causing carbon atoms to diffuse along the newly created grain boundaries of this interfacial layer and into the original substrate.
6. Once the temperature decreases further, the remaining molten white iron solidifies.
7. Hypereutectoid Fe_3C carbides form along the grain boundaries of the austenite of the interfacial layer as it cools through the two-phase austenite plus Fe_3C phase field.

CHAPTER 6 - MASS TRANSFER AT THE INTERFACE

6.1 INTRODUCTION

In the previous chapters it was shown that formation of a good joint between the steel and the white iron involved considerable counter-current mass transfer of alloying elements, as well as a back-and-forth movement of the solid-liquid interface. In order to get a better understanding of the mechanisms involved in these phenomena, the mass transfer across the interface must be explored in more detail.

6.1.1 HISTORY OF DIFFUSION

Some of the first experimental works that studied diffusion were conducted by Thomas Graham (1805-1869) largely in the years 1829-1833. What is now known as Graham's law states that:

'The diffusion or spontaneous intermixture of two gases is effected by an interchange in position of indefinitely minute volumes of the gases, which volumes are not of equal magnitude, being, in the case of each gas, inversely proportional to the square root of the density of that gas.' [93]

Through these studies, Graham linked diffusion with the thermal motion of atoms or molecules. The diffusion of salts in liquids were also studied and he found that diffusion in liquids was at least several times slower than in gases [93].

Adolf Eugen Fick (1829-1901) provided the next major advance in the area of diffusion when he developed a mathematical framework to describe the phenomena of diffusion using an analogy between Fourier's law of thermal conduction and diffusion[94]. Fick's

first law states that diffusion is a spontaneous phenomenon when a system contains two or more components whose concentrations vary from point to point and there is a natural tendency of mass to be transferred in the direction that eliminates (or minimises) concentration differences within that system:

$$J = -D\frac{\partial \emptyset}{\partial x} \qquad \text{EQUATION } 6.1$$

Where J is the diffusion flux in dimensions of length^{-2} time^{-1}, D is the diffusion coefficient or diffusivity in dimensions of length^{2} time^{-1}, Φ is the concentration in dimensions of amount of substance.length^{-3} and x is the position.

Fick's second law shows the effect of diffusion on the concentration field due to a time:

$$\frac{\partial \emptyset}{\partial t} = D\frac{\partial^2 \emptyset}{\partial x^2} \qquad \text{EQUATION } 6.2$$

Fick also discovered and defined diffusion coefficients and measured this coefficient for salt in water.

William Chandler Roberts-Austen (1843-1902) was the first to discover solid state diffusion while expanding on Graham's works and Svante August Arrhenius (1859-1927) established the effect of temperature on the diffusion coefficient of materials as shown in Equation 6.3[95]

$$D = A.\, e^{\left(\frac{-Q}{RT}\right)} \qquad \text{EQUATION } 6.3$$

where A is the prefactor constant, Q is the activation energy for diffusion, R is the universal gas constant and T is the temperature. For cases involving the diffusion of elemental particles (atoms, electrons etc.) Boltzmann's constant k_B is used instead of the gas constant.

After these findings it was believed that atomic diffusion in metals was carried out via an exchange or ring mechanism suggesting that in binary alloys, both components would possess the same diffusion coefficient. Ernest Kirkendall (1914-2005) and his co-workers observed an inequality in the diffusion of copper and zinc between brass and copper as the interface between the two phases moves[96]. The movement of inert markers from the initial interface of a diffusion couple is now known as the Kirkendall effect and proves the vacancy mechanism of diffusion in metals and alloys.

After World War 2, a great deal of research went into solid-state diffusion and our understanding of diffusion mechanisms grew immensely through the usage of radioactive isotopes.

6.1.2 Solid State Diffusion and Its Mechanisms

Diffusion is best summed up as a kinetic process driven by a system's state of non-equilibrium [97-99]. This definition posits that, when there is a difference in concentration of a species within a system, this system will progress toward a state of equilibrium by species located in a region of higher concentration moving to a region of lower concentration. On an atomistic level, diffusion can be considered as a random walk. In the case of fluids this may take the form of Brownian motion of the particles, as first discovered by Brown[100] in 1827 and developed by Einstein[101] in 1905.

Diffusion is a thermally activated process that increases in rapidity exponentially with increasing temperature and occurs spontaneously via a reduction in the Gibbs free energy. Transport via convection on the other hand requires an external force in order to overcome viscous resistance. As crystalline solids resist flow, they are generally not subject to convection.

This study involves the casting of liquid white cast iron onto a solid mild steel substrate and as such atomic transport by both the diffusion and convection mechanisms are occurring in the formation of these composites

In this chapter we will be focussing on solid state diffusion mechanisms and also the mass transfer occurring across the solid-liquid interface. Convection of the fluid will not be considered. Thus it will be assumed that the liquid metal layer is well mixed and in equilibrium. In order to explain the phenomena occurring during this study, an understanding of both the various solid state diffusion mechanisms, and the mass transfer across a boundary layer, is required.

When the solute atoms are much smaller that the solvent atoms they occupy interstitial sites within the host lattice and diffuse by moving from one interstitial site to one of its neighbouring sites as shown schematically in Figure 6.1.

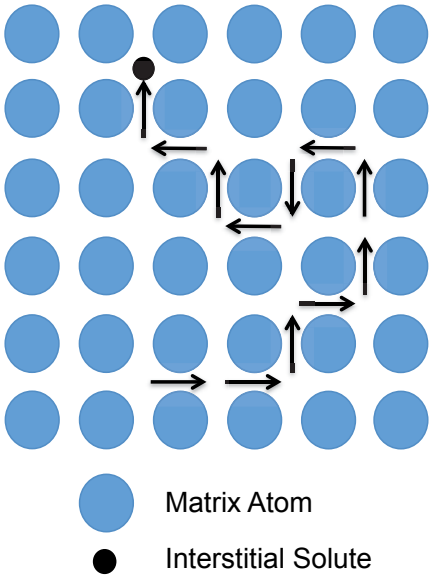

Figure 6.1: Direct interstitial mechanism of diffusion.

Since this diffusion mechanism does not require a lattice defect along which the atom can travel, the diffusion of atoms migrating via this mechanism is relatively fast. Of course only small atoms such as H, C, N and O can diffuse this way, and then only in metals or other materials that contain suitable interstitial spaces.

If an interstitial atom is nearly the same size as the lattice atoms, diffusion may occur via the interstitialcy mechanism in which an interstitial atom may push an atom from the crystal lattice into an adjacent interstitial site as demonstrated in Figure 6.2. The energy

required for an interstitialcy diffusion mechanism in a metal is relatively high in comparison with the vacancy mechanism described later in this section so this mechanism occurs very rarely under thermal diffusion. This mechanism is however very important for radiation induced diffusion as the irradiating particle displaces the atom from the lattice into an interstitial site leaving behind a vacancy.

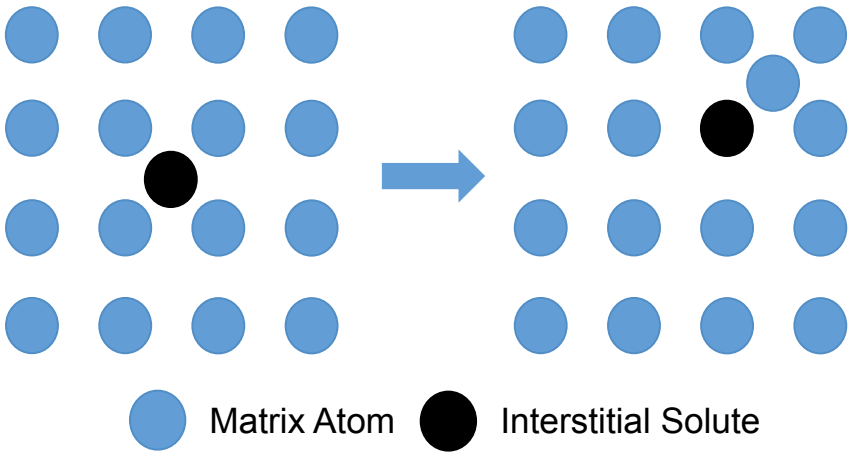

Figure 6.2: Interstitialcy mechanism of diffusion.

Early in the 20th century it was believed that when the size of the solute atoms is similar to that of the atoms in the host lattice, each atom must substitute for the other. There were two substitutional diffusion mechanisms that explain the exchange of neighbouring atoms. These are called the *direct exchange[102, 103]* and *ring mechanism[104]* and are shown in Figure 6.3.

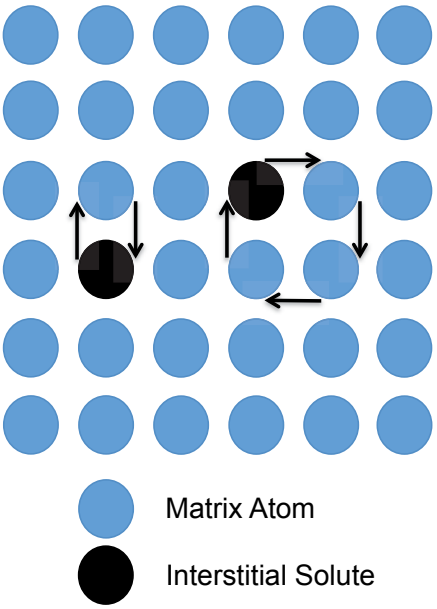

Figure 6.3: Direct exchange and ring diffusion

Both mechanisms would suggest an equal diffusion coefficient for both diffusion species but, as mentioned earlier, when the Kirkendall effect was discovered in the 1940's showing a difference between the diffusion rates of atoms in a binary alloy[96, 105] both mechanisms were mostly rejected. Nevertheless, such collective mechanisms are still believed to occur in amorphous solids[106].

In crystalline metals and ionic crystals it was found that the dominant method by which matrix atoms diffuse is through an interaction with atomic defects or vacancies in the atomic lattice of the host material. This mechanism is schematically shown in Figure 6.4.

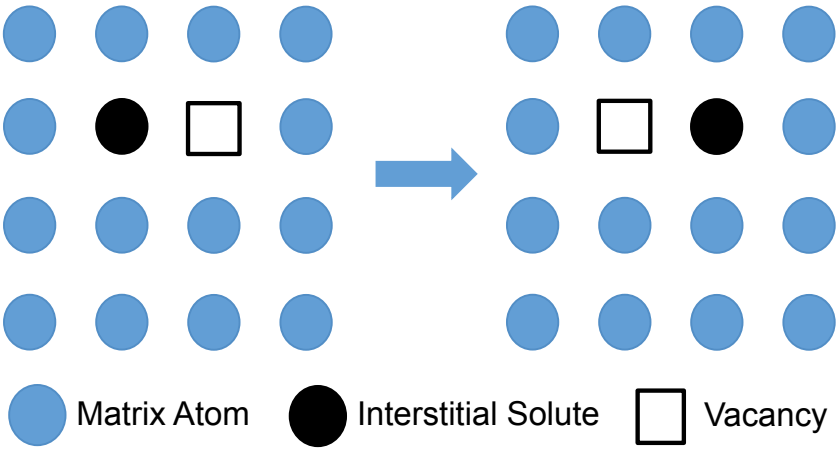

Figure 6.4: Monovacancy mechanism of diffusion.

These atomic defects themselves are induced thermally, and are a natural feature of any crystal lattice. For example, to create a vacancy, energy is required to remove an atom from a lattice site to some lowly coordinated site on a surface, grain boundary or dislocation thereby leaving behind a vacant site. If multiple atoms are moved to surface sites due to a large binding energy between the atoms, an agglomeration of vacancies (divacancies, trivacancies...) is created. This is known as the divacancy mechanism. As the temperature increases, the rate at which mono and divacancies occur increases, however the rate at which divacancies occurs increases more rapidly. Vacancy diffusion at temperatures greater than approximately two thirds of the melting point is dominated by the divacancy mechanism[107, 108].

By 1950, diffusion along grain boundaries was well documented by autoradiographic images [109]. Grain boundaries are highly defective locations in a material, zones where the periodic structure of the lattice breaks down. Grains in polycrystalline materials are oriented randomly and as such a wide range of grain boundaries exist. The nature of grain boundaries depends on the misorientation of the adjacent grains and the orientation of the relative boundary plane. Four main categories are used to describe grain boundaries including:

(i) Low angle boundaries where the misorientation between the two grains is less that 15°
(ii) High angle boundaries occur where misorientations are greater than 15°
(iii) Special high angle boundaries such as twin boundaries
(iv) General boundaries which are the standard type of grain boundaries occurring in polycrystalline materials

In 1951, Fisher[110] proposed a model which is widely accepted and upon which most mathematical treatment of grain boundary diffusion is based. Calculations are based upon an isolated grain boundary of a certain width and diffusion coefficient that is much greater than that of lattice diffusion in the adjacent grains. Le Clair estimated that the ratio between the diffusivity along grain boundaries to that in the lattice is of several orders of magnitude[111].

Three major classifications for grain boundary diffusion were developed by Harrison in 1961[112] and are called Type A, B and C kinetics. These classifications are defined by three characteristics; the temperature at which the diffusion occurs, the length of time that the diffusion occurs and the average grain size.

Type A kinetics occur at high temperatures and/or long annealing times and/or when the microstructure is made up of primarily small grains. Under this regime, the diffusion fields surrounding the grain boundaries are so large they overlap and the lattice diffusion length is at least 20% larger than the distance between grain boundaries as shown in Equation 6.4[113].

$$\sqrt{Dt} \geq d/0.8 \qquad \text{EQUATION 6.4}$$

This results in a relatively planar growth front as shown in Figure 6.5.

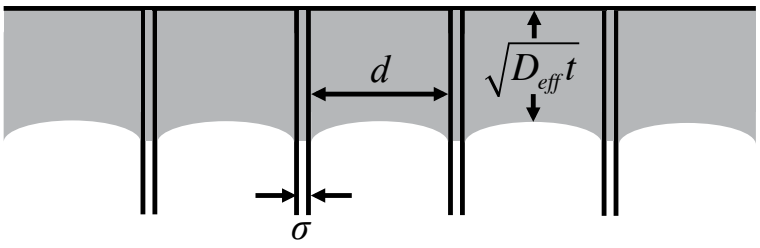

Figure 6.5: Type A diffusion regime in a polycrystal.

An approximate expression for the effective diffusion, D_{eff}, in a Type A diffusion regime polycrystalline material was proposed by Hart[114] and is shown in Equation 6.5.

$$D_{eff} = gD_{gb} + (1\text{-}g)D \qquad \text{EQUATION 6.5}$$

The quantity g is the fraction of atomic sites in the grain boundary of the polycrystal and can be expressed as:

$$g = \frac{q\,\sigma}{d} \qquad \text{EQUATION 6.6}$$

where q is a numerical factor depending on the grain shape. Parallel grain boundaries have a q factor of 1 and q is 3 for cubic grains.

Type B kinetics occur when the temperature is lower and/or annealing time is shorter and/or the grain size is larger than in type A kinetics. Much like type A kinetics, type B kinetics have a volume diffusion field surrounding the grain boundary but the rate of lattice diffusion is considerably slower than that of diffusion at the grain boundary and as such the diffusion fields of neighbouring grain boundaries do not overlap as demonstrated in the diffusion profile shown in Figure 6.6.

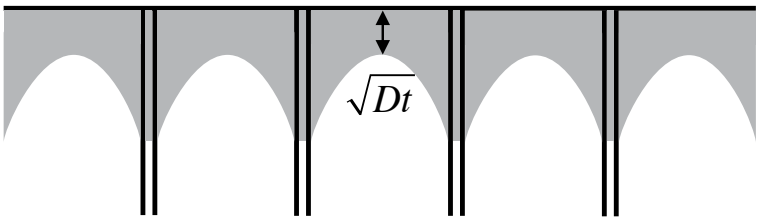

Figure 6.6: Type B diffusion regime in a polycrystal.

Figure 6.7 shows the average concentration per unit distance away from the grain boundary, $\bar{c}$ as a function of the penetration distance *z.* It should be noted that $z^{6/5}$ has no physical meaning and is only used as it is a good empirical mathematical representation of the diffusion profile shape. This "step" in the diffusion profile indicates that diffusion in this region is caused by lattice diffusion from the surface and not from the grain boundary.

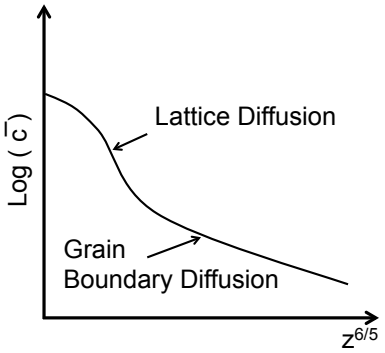

Figure 6.7: Average concentration with respect to penetration distance.

Figure 6.8 shows type B kinetics diffusion profiles for self-diffusion in silver polycrystals. The relative species activity can be seen to be linear with respect to the grain boundary diffusion length where grain boundary diffusion predominates and then a slope change occurs when lattice diffusion becomes the major mode of diffusion.

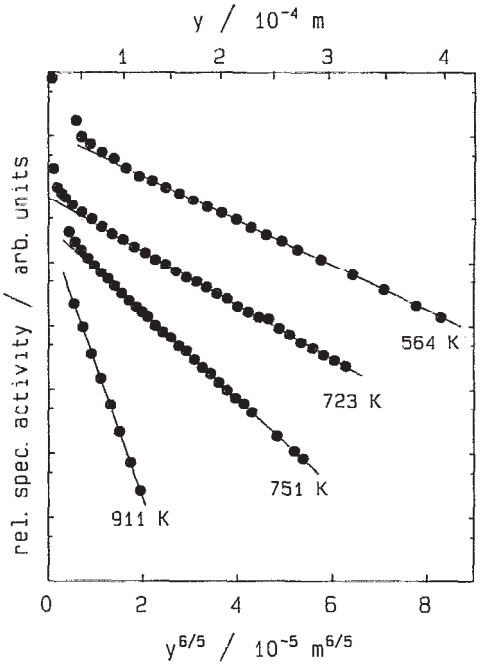

Figure 6.8: Diffusion profiles of grain boundary self-diffusion in Ag[115].

Type C diffusion only occurs when the annealing temperature is sufficiently low and/or diffusion occurs over a relatively short period of time. Under this diffusion mechanism, diffusion only occurs along the grain boundaries without any volume diffusion fields surrounding the grain boundaries as shown in Figure 6.9.

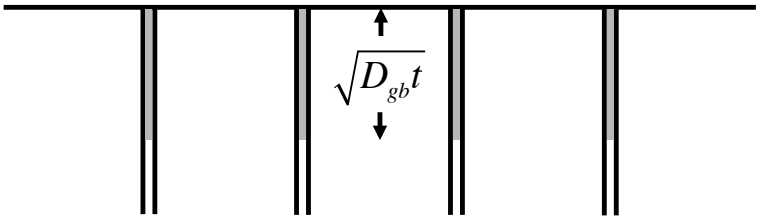

Figure 6.9: Type C diffusion regime in a polycrystal.

6.1.3 Surface Heat Treatment Solutions to Fick's Second Law

As mentioned previously, in this study we will be examining diffusion occurring at the interface between liquid white iron and a solid mild steel substrate. As such, the concentration at the surface of the mild steel will be vastly different to that of the bulk.

In order to solve Fick's second law linear diffusion equation in such a system, an error function solution known as the Grube solution may be used.

Grube's solution, as shown in Equation 6.7, models the diffusion out of one half of a diffusion couple, through an interface, into a semi-infinite medium. (Often a special definition for the position for the interface, known as the 'Matano interface', is used. This is the location that partitions the amount of diffusing element material into equal 'lost' and 'gained' amounts. To a first approximation this is the same as the position of an actual physical interface.) In Grube's equation C_x is the concentration at some distance x from the interface, C_0 is the initial concentration of one half of the diffusion couple, C_s is the concentration at the interface, x is the distance in centimetres from the interface, D is the interdiffusion coefficient in square centimetres per second and t is the time in seconds of the diffusion treatment.

$$C_x = C_0\text{-}(C_s\text{-}C_0)\times\left(\mathrm{Erf}\left(\frac{x}{(Dt)^{0.5}}\right)\right) \qquad \text{EQUATION 6.7}$$

It should be noted that the diffusion constant used in this model is constant for a given temperature T, and does not vary with composition as is the case with most diffusion couples in reality. The variation of diffusion coefficient is small when the concentration of the second element in the diffusion couple is small but increases with greater concentrations. This assumption is a limitation of this model but is needed to provide an analytical solution to Fick's second law.

6.1.4 DIFFUSION COEFFICIENTS OF VARIOUS ELEMENTS IN IRON

In order to accurately model the diffusion of elements across the interface of these white iron steel composites the rate at which these elements diffuse in iron must first be established. Table 6.1 shows the diffusion coefficients of various tracer elements within iron. Iron in the ferrite phase is designated by α and austenite by ɣ. The parameters shown must be substituted into Equation 6.3 to provide an actual estimate of D at some specific temperature.

TABLE 6.1: DIFFUSION COEFFICIENTS OF DIFFERENT ELEMENTS IN IRON.

Tracer Element	Temperature Range (°C)	A ($cm^2.s^{-1}$)	Q ($kcal.mol^{-1}$)	D ($m^2.s^{-1}$)	Reference
C^{14}	350-850 (α)	$6.2*10^{-3}$	19.2	1.09E-09	[116]
	900-1350 (ɣ)	0.1	32.4	2.24E-10	[116]
Cr^{51}	800-880 (α)	$8.52^{+3.2}_{-2.33}$	59.9±1.6	2.16E-12	[117]
	950-1400 (ɣ)	$10.8^{+3.35}_{-2.56}$	69.7±1.7	1.07E-13	[117]
Mn^{54}	800-900 (α)	$0.35^{+0.31}_{-0.17}$	52.5±2.3	1.02E-12	[118]
	920-1280 (ɣ)	$0.16^{+0.06}_{-0.05}$	62.5±1	1.72E-14	[118]
Ni^{63}	800-900 (α)	9.9	61.9±2	1.30E-12	[119]
	930-1050 (ɣ)	0.77±0.2	67±0.7	1.87E-14	[120]
	1140-1400 (ɣ)	3	75	5.17E-15	[119, 121]

It should be noted that diffusion is generally an order of magnitude greater in the ferrite phase than in the austenite phase and this is due to the less dense atomic packing of the body-centred cubic ferrite (68%) when compared with the closest packing (74%) of the face-centred structure in the austenite.

Equation 6.3 shows how the diffusion coefficient, D, is calculated from both A and Q which are both common methods by which to define the diffusion coefficient of materials. As $Q_{GB} < Q_V$, as the temperature increases, the rate of diffusion at grain boundaries increases less rapidly when compared with volume diffusion so at higher temperatures the differences between diffusion coefficients may be less significant[122].

Table 6.2 shows the findings of Fridberg et al.[123], where the ratio of the rate of diffusion of each of the elements at 1200°C is compared to that of carbon in austenite. It can be seen that the rate of diffusion of chromium, manganese and nickel is much slower than that of carbon. This is due to the carbon atoms' smaller physical size when compared with the metallic elements. These tests were performed in single crystals and were measuring the rate of volume diffusion. Of course, in the present project the steel substrate consists of many grains and thus the rate of diffusion of carbon in the steel will be increased due to the atoms ability to diffuse through the grain boundaries of the austenite as well.

TABLE 6.2: RATIO OF DIFFUSION RATES FOR ELEMENTS IN AUSTENITE IN COMPARISON TO CARBON[123].

Element	Ratio at 1200°C
Cr	1/1690
Mn	1/27500
Ni	1/59400

6.1.5 DIFFUSION COUPLE

The use of diffusion couples for the construction of phase diagrams has been used for quite some time[124] and although outside of the scope this project due to the complexity of the multi-phase, solid-liquid interface in this study, it would be prudent to look at this modelling technique and how it may be used in future studies on the topic.

Kodentsov et al.[125] provides a discussion of the usage of diffusion couples when determining phase diagrams. All of the discussion revolved around solid-state diffusion couples but still provides a basic understanding of how such systems may be used. Although any system in which diffusion is occurring is not in a state of equilibrium, for these calculations local equilibria is assumed within the diffusion zone.

A Ag-Cu solid-liquid diffusion couple was examined by Kuntz et al.[126] where a binary alloy was held isothermally and cellular precipitation of the copper base metal occurred adjacent to the silver substrate.

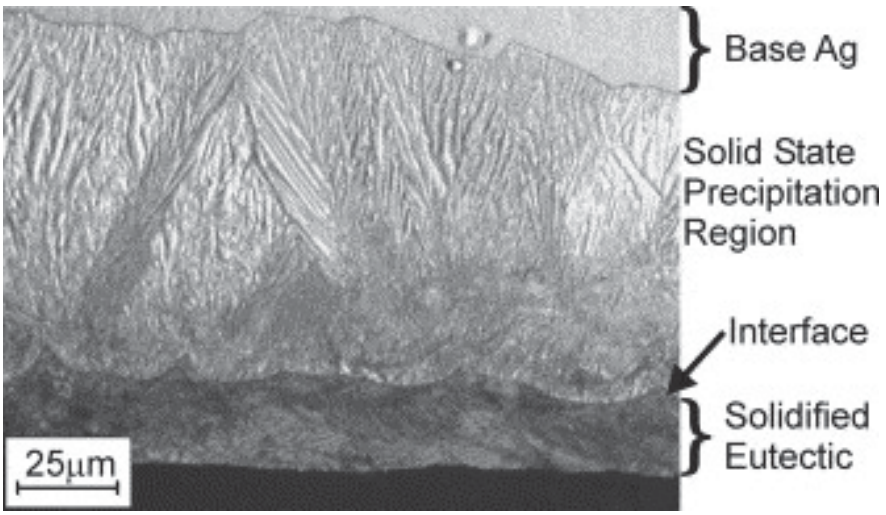

Figure 6.10: Optical micrograph of the interface showing the solidified eutectic and the cellular precipitation adjacent to the interface[126].

While the diffusion couple was not mathematically modelled in this paper, the nature of the isothermal phase formation was examined using DSC. This study showed a moving boundary, similar to that in the present study.

Tanaka and Kajihara[127] studied a copper-aluminium solid-liquid binary diffusion couple and modeled mathematically the composition of the liquid phase at the interface, Figure 6.11. It can be seen that with increasing soak time and soak temperature, the penetration depth of interdiffusion also increases.

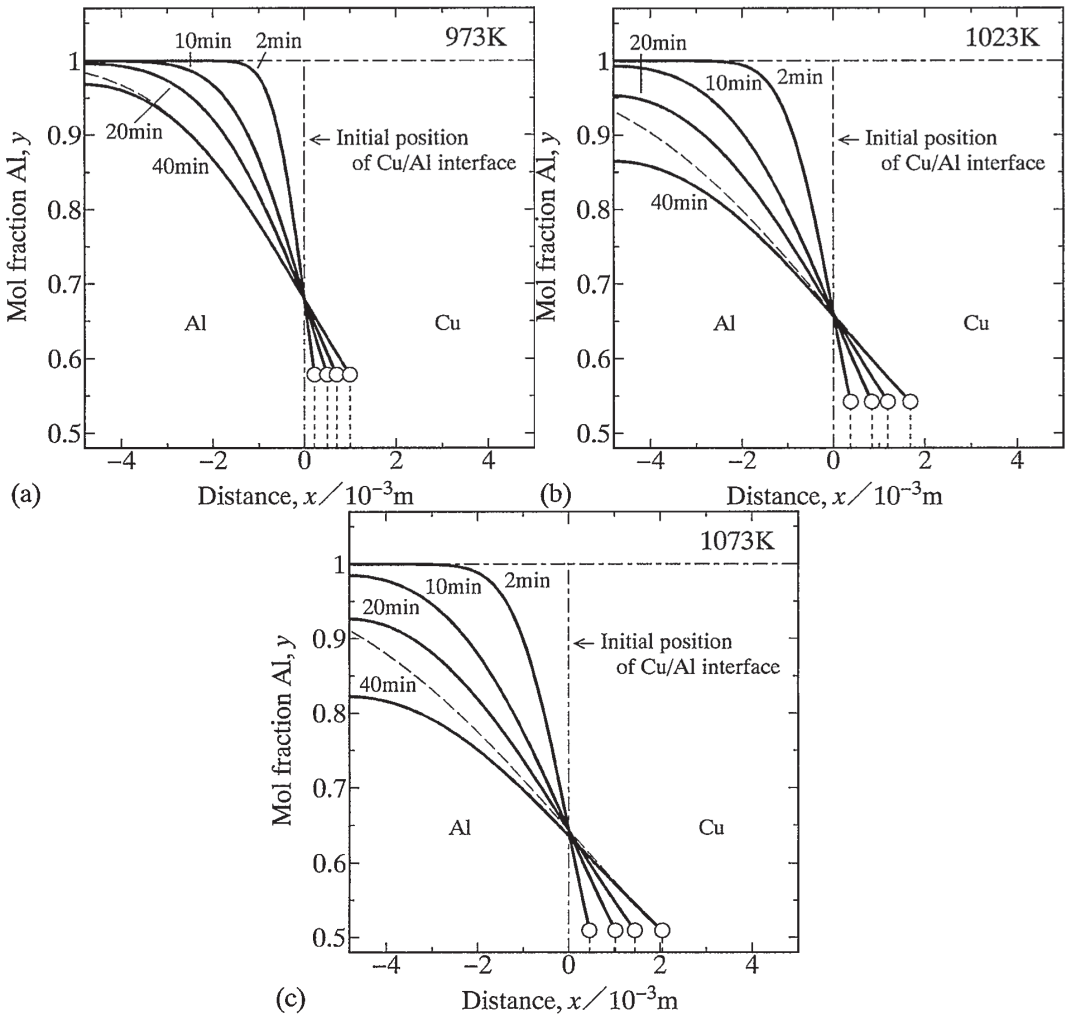

Figure 6.11: Concentration profiles of Al in the L phase calculated for (a) T = 973 K, (b) T = 1023 K and (c) T = 1073K[127].

Diffusion couples simulate the diffusion across an interface quite well but are extremely complex and are generally used in binary systems and most often at solid-solid interfaces. Using such a model is outside of the scope of this project. Instead a much simpler, first-order approach is detailed in the results section of this chapter.

6.2 EXPERIMENTAL

Diffusion studies in this project can be divided into two sections, experimental determination of diffusion between the two materials by plotting concentration curves across the interface using energy dispersive spectroscopy (EDS) and wavelength dispersive spectroscopy (WDS), and theoretical predictions of diffusion rates and mass transfer using computational methods.

6.2.1 Experimental Determination

Samples that were made for previous sections in this project were used for experimental determination of the diffusion across the interface of the composite. Samples were sectioned, mounted and polished in order to gather full spectrum line scans using both EDS and WDS. WDS was required to map carbon as the energy of the Kα X-rays given off from carbon (0.2774eV) is too low to penetrate the beryllium window of a standard EDS detector.

6.2.1 Theoretical Determination

Theoretical determination of the diffusion processes occurring at the interface of these composites was performed by using the DICTRA diffusion simulation software. While the software has built-in parameters to calculate the rate of solid-state diffusion in the substrate [88], the mass transfer from the melt to the solid phase, and within the liquid phase itself, is not well quantified. Mass transfer across the solid-liquid interface was controlled here by using a 'labyrinth factor' [128], which however in this case was used to *increase* rather than (as usual) decrease the rate of diffusion. This is because convective motion in the melt would greatly accelerate mass transfer. The factor used was chosen by trial and error to produce a rate of interface migration that reproduced the experimentally observed rate. Phase equilibria were calculated using ThermoCalc with the TCFE-7 database and kinetics data came from a database built into DICTRA.

Software was also created by the author to model the diffusion of elements from the Matano interface into the mild steel substrate based on Grube's solution for Ficks second law. Grube's solution predicts the diffusion from the Matano interface into a semi-infinite medium and was explained in detail in the introduction to this chapter.

6.3 Results and Discussion

In this study, the diffusion of various elements across the interface of a white iron/steel composite was studied. The method by which these samples were created was detailed in the previous chapter.

In order to examine the concentration of various elements, EDS based X-ray mapping was employed. Figure 6.10 shows where this line profile was taken from, with the concentration coming from an average of 10 pixels above the line and 10 pixels below.

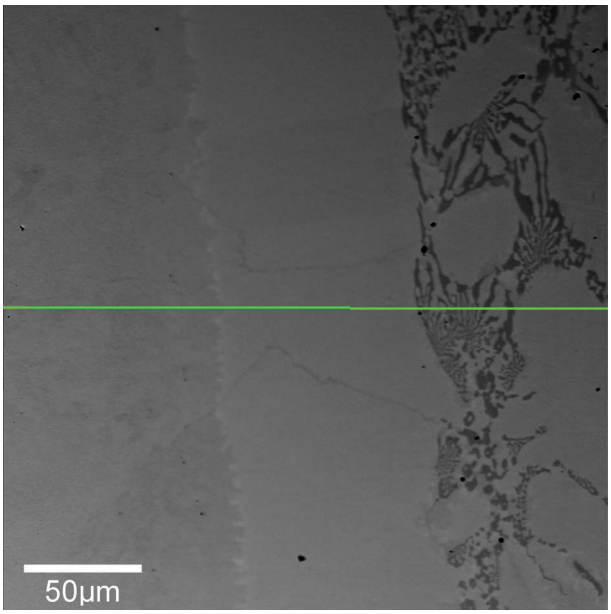

Figure 6.10: BSE image of the interfacial region. Green line indicates the region from which the line profile was taken. (HWOF = 260µm)

Figure 6.11 shows the line profiles for both iron and chromium across the interfacial region of one of the composites after a 25 minute soak time. On the left-hand side of the image lies the steel substrate with the interfacial region in the center and the white iron to the right. The region between approximately 60-110 µm shows the concentration gradient of both iron and chromium between the steel substrate and the epitaxially grown interfacial layer. Across this region solid state diffusion of both elements occurred, with chromium diffusing from first the liquid white iron and then from the

newly formed interfacial layer, and iron diffusing from the steel substrate into the interfacial layer and liquid white iron.

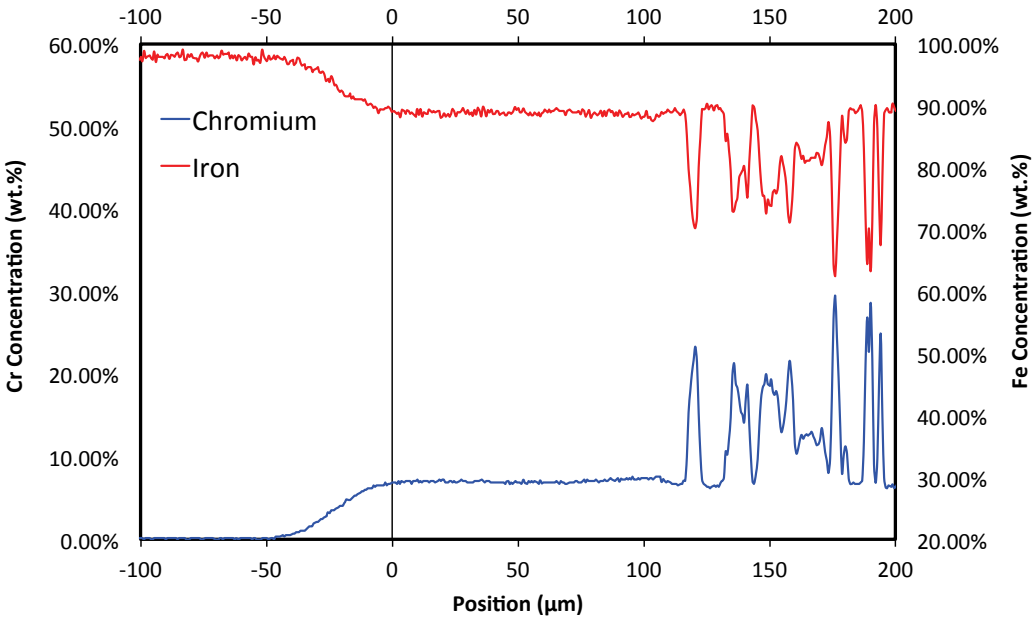

Figure 6.11: Concentration line profiles for both chromium and iron. Chromium concentration is shown with the blue line while iron is shown with the red. The steel substrate is shown to the left of zero and the interfacial zone and white iron is shown to the right.

It can be seen that the iron and the chromium atoms seem to substitute for each other. After a 25-minute soak time, chromium has diffused approximately 50 µm into the steel substrate. The nominal chromium composition of the steel substrate was 0.03% chromium, which is shown on the left hand side of Figure 6.11, and the chromium content increases to approximately 6 wt.% at the interfacial layer.

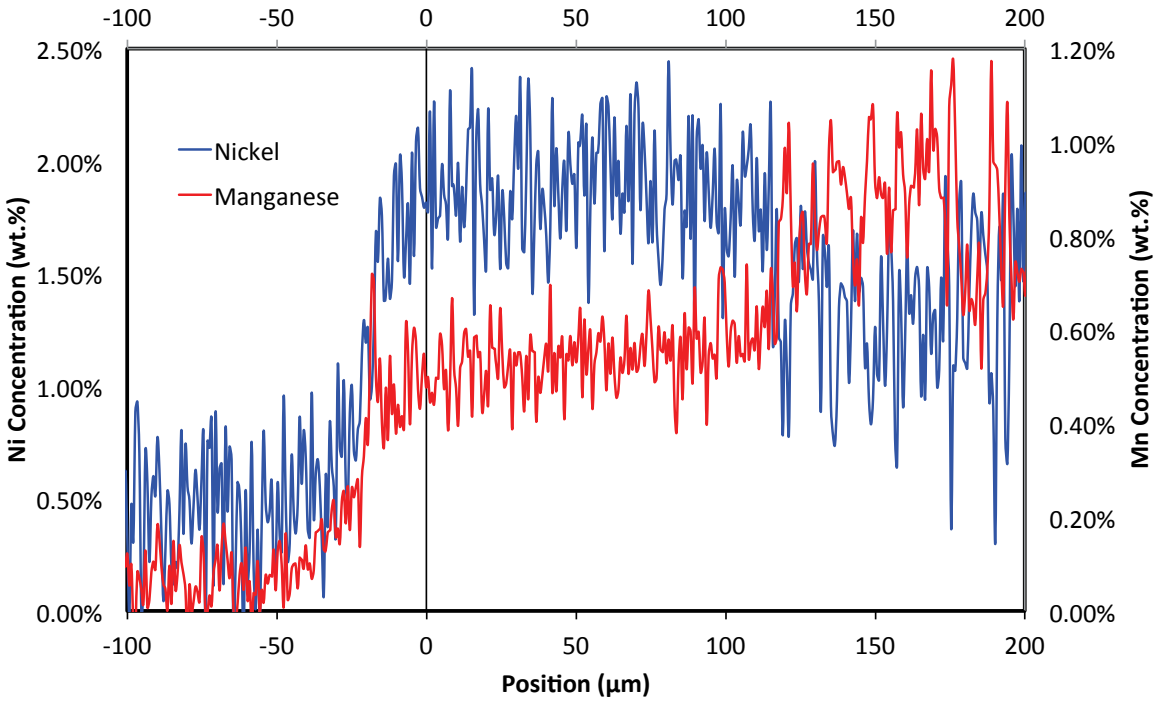

Figure 6.12: Concentration line profiles of nickel and manganese across the interfacial region of the sample. The steel substrate is shown to the left of zero and the interfacial zone and white iron is shown to the right.

Figure 6.12 shows the extent of the diffusion of manganese and nickel across the interface of the white iron/steel composites. While the concentration profile is noisy, it can be seen that the nickel diffused approximately 30 µm into the steel substrate and manganese diffused approximately 40 µm into the steel substrate. This difference is to be expected when viewed in the light of the diffusion coefficients shown in Table 6.1.

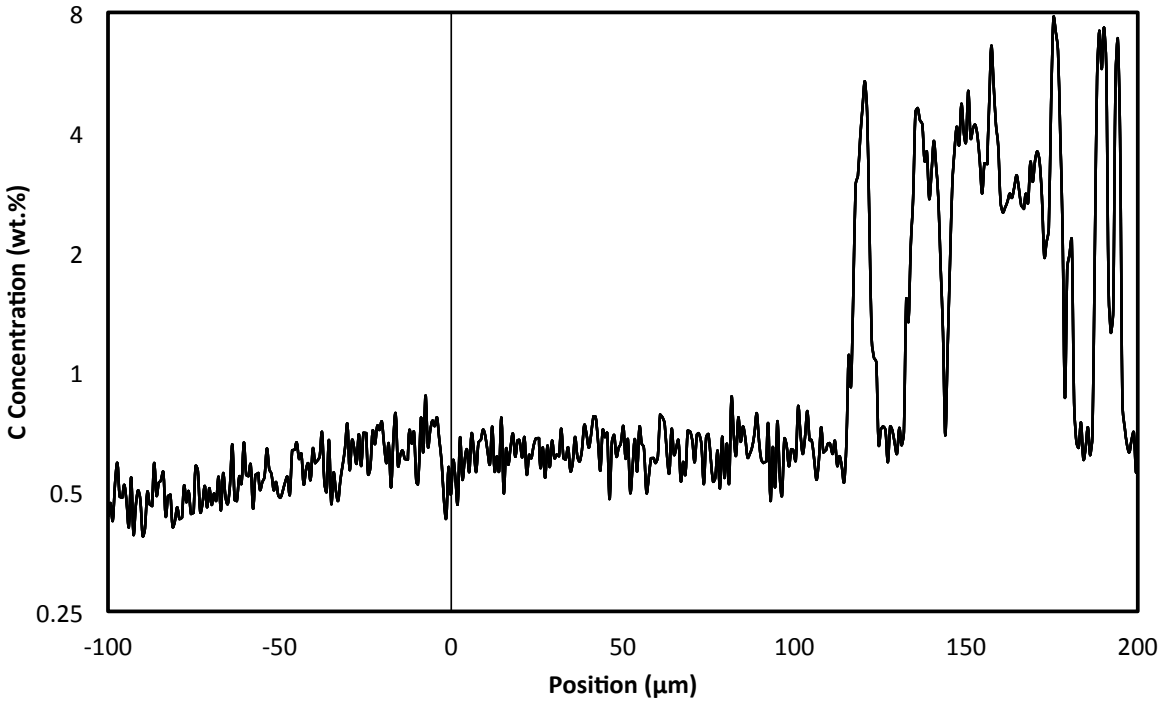

Figure 6.13: Carbon diffusion profile of the interfacial region. The steel substrate is shown to the left of zero and the interfacial zone and white iron is shown to the right. Note the vertical concentration scale is logarithmic.

The carbon concentration of the original steel substrate was approximately 0.05 wt.% so it can be seen that carbon has diffused a lot further than the range of the X-ray map. In order to examine the extent of diffusion of carbon into the steel substrate, a low magnification WDS stage scan was performed across the interface.

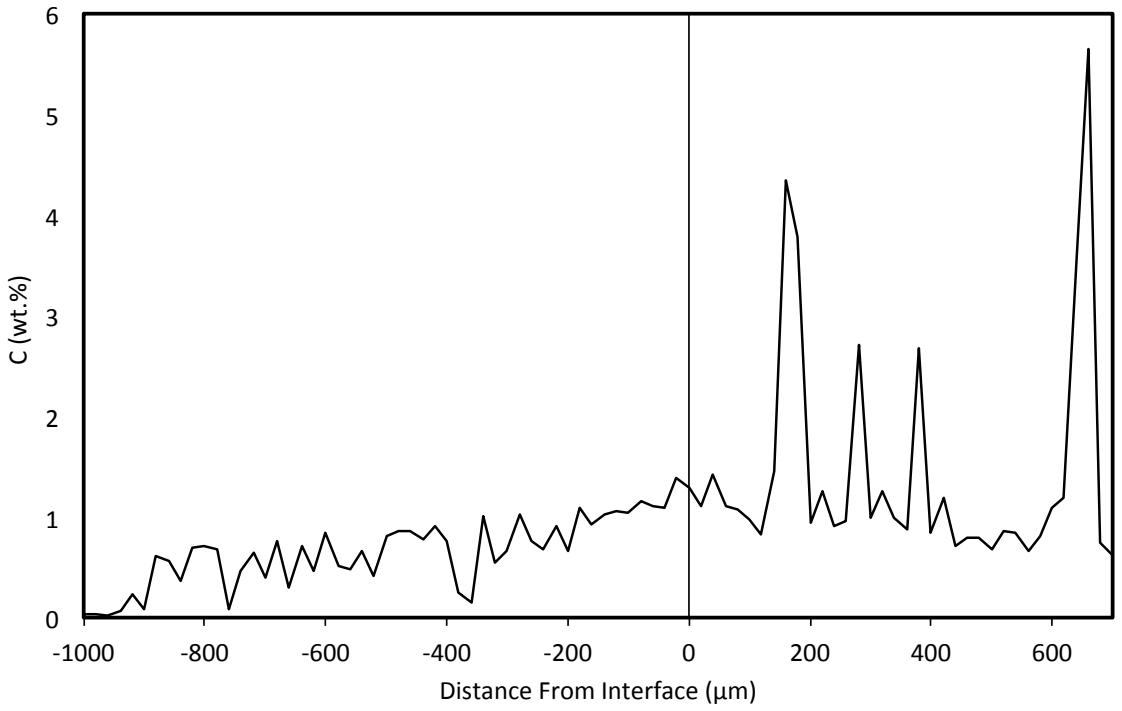

Figure 6.14: WDS stage profile of the interfacial region of a white iron/steel composite. The steel substrate is shown to the left of zero and the interfacial zone and white iron is shown to the right. Measurements were taken every 20 μm.

The WDS carbon stage scan shown in Figure 6.14 displays the extent of the diffusion of carbon from the white iron into the steel substrate. Some high carbon spikes can be seen within the steel substrate, and are caused by dense regions of cementite (Fe_3C). The carbon appears to have diffused at least 900 μm into the steel substrate. Actually, the carbon has diffused much further into the substrate than even this scan reveals but it clearly shows that carbon has diffused much further than chromium, manganese and nickel due to its considerably greater rate of diffusion.

Figure 6.15 shows a micrograph of the interfacial region of one of the white iron/steel composites. This sample was etched using a nital etch which etches the ferrite and reveals the cementite which appears light grey in colour. It can be seen that the density of cementite close to the interfacial region is much greater and reduces in density toward the outer edge of the steel substrate (ie. away from the white cast iron).

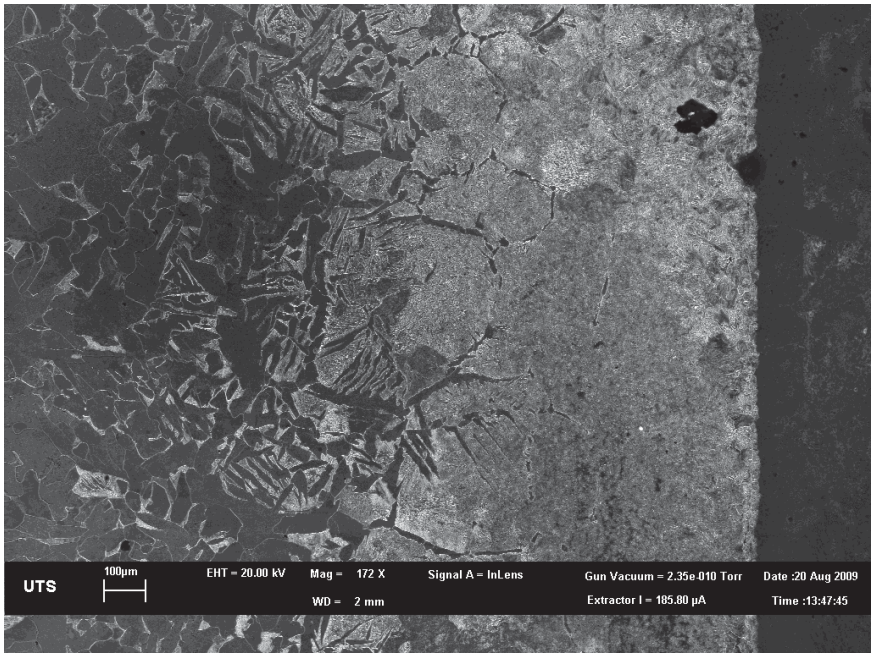

Figure 6.15: Secondary electron in-lens electron micrograph of the interfacial region of a white iron/steel composite. The sample has been etched using a nital etch, removing the ferrite and revealing the cementite, which is light grey in colour. (HWOF = 2.1mm)

At the outer edge of the substrate it can be seen that the carbides are primarily located at the grain boundary of the steel substrate. Further into the substrate it can be seen that the carbon first diffused along the grain boundary accompanied by volume diffusion surrounding the grain boundary. Closer to the interface, the volume diffusion fields were so large that they joined and the material appears to be completely pearlitic.

As illustrated in previous chapters, diffusion at the interface of these composites is a very complex problem with many phases being present, a moving boundary layer in the form of the steel substrate being dissolved and many species diffusing. Modeling such phenomena is extremely problematic. Nevertheless, it is extremely helpful to consider a relatively simple first-order approximation which will be detailed in this chapter in order to make comparisons to the experimentally determined diffusion profiles. Theoretical diffusion profiles into the steel substrate of each of the elements were created using Grube's solution to Fick's second law, as detailed in the experimental section of this chapter. These calculations, made using software developed by the author, were based on the nominal soak time of the sample and although some diffusion would have occurred below the ferrite transformation temperature in the steel,

diffusion was only modelled with the steel in its austenite phase. Given the very great effect of temperature on diffusion coefficients this is a reasonable approximation. These diffusion calculations do not take into account the effect of grain boundary diffusion and the diffusion coefficient used was that of volume diffusion, as shown in Table 6.1.

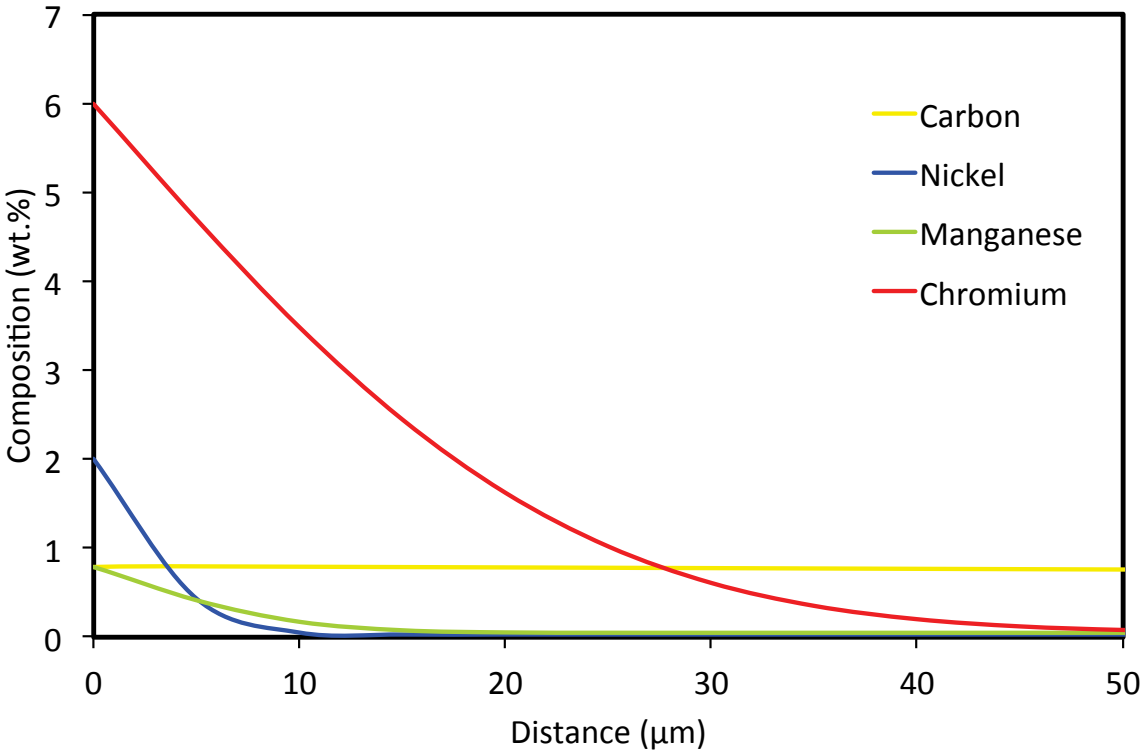

Figure 6.16: Theoretical diffusion profile of Cr, Mn, Ni and C based on Grube's solution to Fick's second law after a soak time of 10 minutes at 1250°C.

As can be seen in Figure 6.16, the extent of diffusion of each of the elements varies quite greatly as would be expected based upon the diffusion coefficients shown in Table 6.1 and the EDS results. It appears that Grube's solution predicts that the nickel will diffuse into austenite approximately 11µm, the manganese 18µm and the chromium 50µm. The carbon diffusion profile appears to be almost horizontal when compared with the other elements on the particular horizontal scale used. This is due to the much greater rate of diffusion of carbon when compared with the other elements.

Figure 6.17 shows the extent of the diffusion of carbon into the austenite on an expanded horizontal scale. As can be seen the carbon has diffused a great deal further than the other elements into the steel substrate.

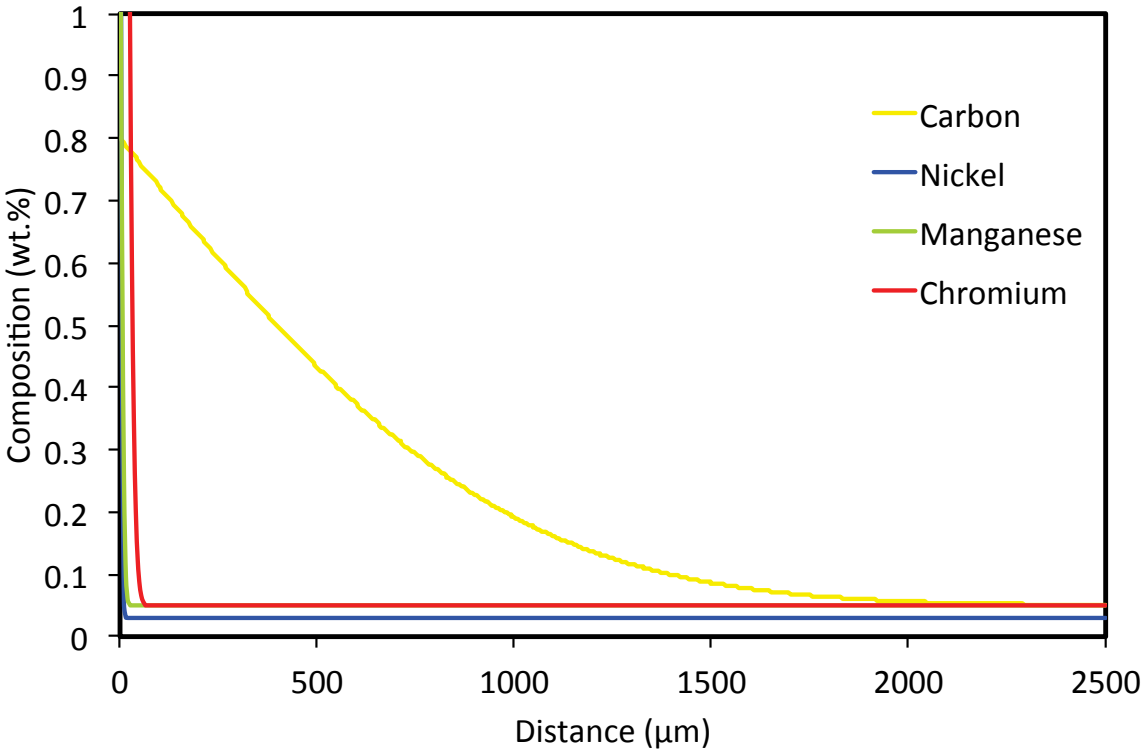

Figure 6.17: Theoretical diffusion profile of Cr, Mn, Ni and C based on Grube's solution to Fick's second law, seen after 10 minutes at 1250°C.

When comparing these theoretical results with the experimental EDS results it can be seen that they match fairly closely with the theoretical predictions as shown in Figure 6.18. The small difference between the calculated and measured profiles for Cr might be due to the diffusion coefficient used being a little low for the particular austenitic matrix. However, the 'depth' of penetration of the calculated and measured curves is very similar.

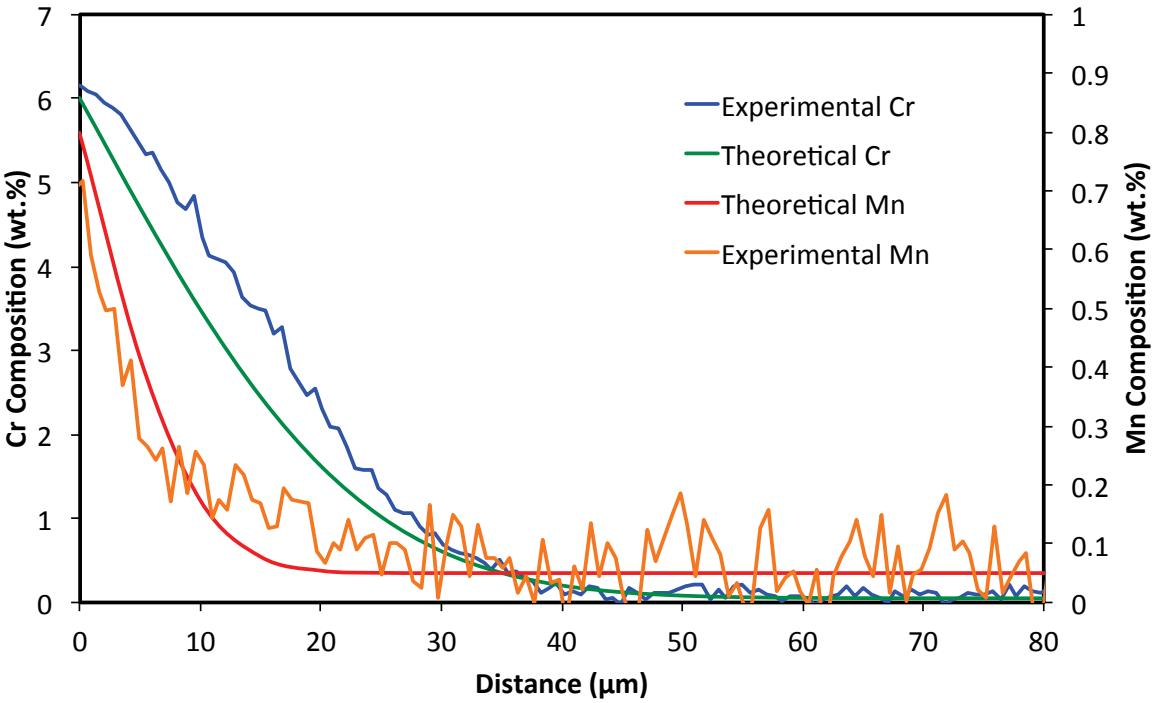

Figure 6.18: Comparison of the extent of diffusion between Grube's theoretical solution and X-ray EDS profile of the chromium content from the interface between the austenitic interfacial layer and the steel substrate.

Further insight into the thickening of the interfacial layer and diffusion of carbon into the steel substrate of these composites was obtained by conducting simulations of the process using the DICTRA software package. DICTRA is a sophisticated software package that simulates the diffusion of a variety of elements in a multi-component alloy system. Using both thermodynamic and kinetic data built into the software, the movement of atoms across the interface was calculated. Figure 6.19 shows a simulation of the carbon concentration as a function of time and distance across the interface at 1250°C. Simulations were carried out using the composition of Huggett's low melting point white iron[27], which is Fe-12Cr-4.1C-1.6Mn-1Ni-0.5Si, for the liquid white iron and Fe-0.05C for the steel substrate. The input script for the simulation is shown in Appendix 1. A labyrinth factor was used to increase the rate of diffusion due to the fact that DICTRA cannot simulate the turbulence in the melt due to convection, which would increase the rate of diffusion from the melt into the steel substrate.

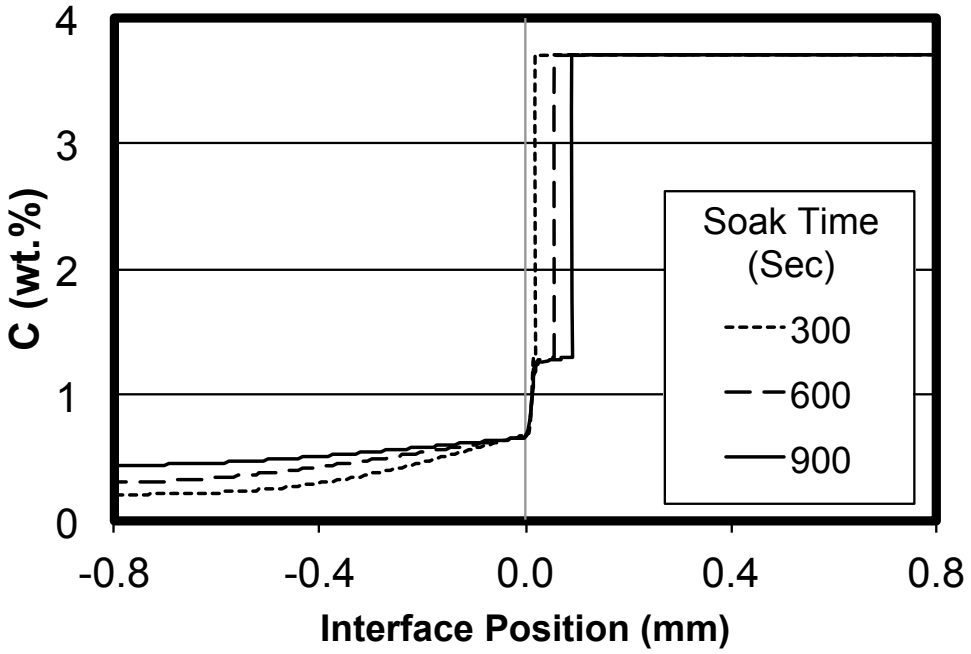

Figure 6.19: DICTRA thermodynamic diffusion simulation of interfacial growth in these mild steel/white iron composites during isothermal treatment at 1250°C.

The location of the original interface between the mild steel and the white iron was located at +0.040 mm relative to the interface at the end. An interesting aspect of the simulation was that it predicted that, as the carbon diffused into the mild steel, it initially reduced the melting point of the steel substrate below that of the soak temperature, causing the substrate to partially melt and dissolve into the liquid white iron. This is the situation at about 300 seconds, at which point the interface transitions directly from the substrate to the melt without any interfacial layer. However, from this time onwards, the increase in Fe concentration in the melt resulted in the growth of an austenite layer with approximately 1.5 wt.% C, which increased in thickness with soak time. This phenomenon relies upon either a lack of convection in the melt or on it having a relatively small volume so that a discernible increase in its content of Fe can occur. Both of these factors are likely to be satisfied in the experimental samples prepared in this project. As noted in the previous chapter and was confirmed by EBSD, this interfacial layer forms epitaxially upon the austenitic steel substrate.

In order to better understand the joining mechanism of this technique, the mechanism will be broken down in its constituent parts and modelled mathematically.

The first stage of this process is the dissolution of the steel substrate. In this model it will be assumed that the iron that is introduced from the steel substrate is completely mixed throughout the liquid white iron. This is not an unreasonable assumption as optical emission spectrometry revealed an increase in iron content when comparing the composition of the original low melting point white iron with that of the white iron in a cast composite 10-20mm from the interface as shown in Table 6.3.

TABLE 6.3: COMPOSITION OF WHITE IRON BEFORE AND AFTER CASTING.

Element	Low Melting Point White Iron (Wt.%)	Cast Composite White Iron (Wt.%)
Fe	80.9	81.7
Cr	12	11.7
C	4.1	3.8
Mn	1.5	1.4
Ni	1	0.9
Si	0.5	0.5

From Figure 6.20 it can be seen that the composition only requires an increase of 0.3 wt.% iron in order to bring the liquidus up to the recommended soak temperature of 1250°C. This iron, as suggested earlier, will come from the steel substrate.

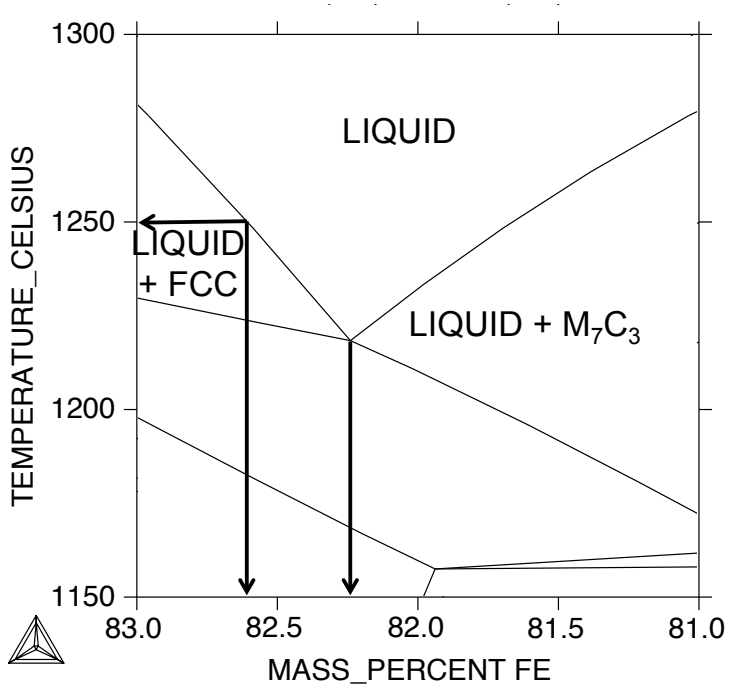

Figure 6.20: A small region around the eutectic of the phase diagram of the low melting point white iron showing the variation in liquidus with changing iron content. Note, the Mass Percent Fe axis is in *descending* order to replicate the appearance of the traditional carbon varying phase diagram.

In order for the steel substrate to dissolve into the liquid metal, the melting point of the steel must be decreased and this occurs by the diffusion of carbon from the liquid metal into the substrate. In Figure 6.21 a phase diagram of the eutectic region of iron-carbon is shown. The mild steel used in this study contained very few alloying elements and only 0.08% C placing its melting point over 1500°C. However, the melting point of the substrate is reduced as carbon diffuses into it, until at 1.6% C it will melt at 1250°C

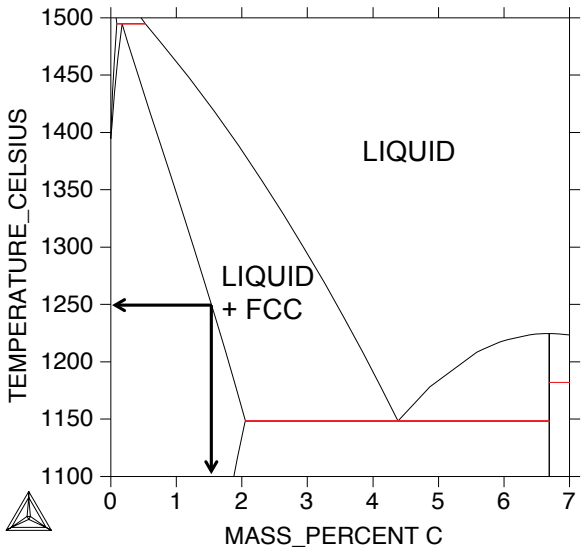

Figure 6.21: A small region around the eutectic of the phase diagram of iron-carbon showing the variation in liquidus with changing carbon content.

Once the substrate has dissolved/melted, the iron that was in the affected volume disperses throughout the melt and the process continues until the iron content in the melt has increased to the point where the liquidus of the melt reaches 1250°C, at which point a rim of austenite begins to grow on the substrate.

In order to calculate the amount of the substrate that will be dissolved, the volume of iron required to increase the liquidus of the melt to 1250°C must be calculated. The amount depends critically on the volume of the molten phase, since more Fe is required for larger volumes of melt. The phase diagram shown in Figures 6.20 and 6.21 provide the necessary limiting compositions. With this in mind, it can be seen that with a greater liquid volume relative to the total substrate surface area, more of the steel substrate will be dissolved before the liquidus of the melt reaches 1250°C. This is illustrated in Figure 6.22. This is a factor that must be taken into consideration when creating these kiln cast composites as, if the ratio is too great, the substrate will dissolve completely into the melt.

Figure 6.22 was calculated based on a density of steel of 7.8 g/cm^3. With a known total surface area of the substrate, the total volume of the substrate that must be dissolved may be calculated. This also reveals the thickness of the dissolved layer. This exercise would need to be carried out when designing such castings.

From Grube's solution to Fick's second law, as shown in Equation 6.7, the time taken to reach a carbon content of 1.6% (above which the substrate will become liquid) may be calculated. By rearranging Equation 6.7 we get:

$$Dt = \left[\frac{x}{\left(\text{invErf}\left(\frac{C_x}{C_0-(C_S-C_0)}\right)\right)}\right]^2 \qquad \text{EQUATION 6.8}$$

Where D is the diffusion constant if the element, in this case carbon, through the substrate, x is the distance predetermined as the amount of the substrate that must be dissolved in order to increase the melting point of the white iron and C_x is equal to 1.6 which is the composition above which the substrate will dissolve.

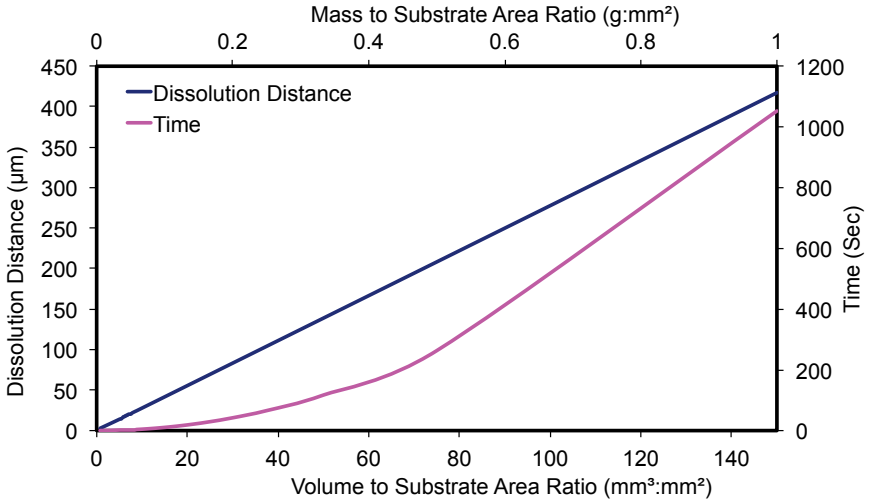

Figure 6.22: A plot showing the relationship between both the thickness of the dissolved layer of the substrate and time taken to dissolve this layer, and the ratio of amount of white iron and substrate surface area.

Now that the amount of substrate dissolution has been calculated, the diffusion profile of the carbon into the steel substrate must be calculated in order to calculate the total amount of carbon that has been removed from the liquid white iron, which will in turn reveal the thickness of the interfacial layer that will form. As any concentration greater than 1.6% carbon would have dissolved the substrate, the diffusion profile created will

have a carbon concentration of 1.6% at the Matano interface. Due to the dissolution, this interface would have moved over time but for the purpose of this section of the simulation that is irrelevant.

By integrating Grube's solution as shown in Equation 6.9:

$$\int_0^T C_0\text{-}(C_s\text{-}C_0)\times\left(\mathrm{Erf}\left(\frac{x}{(Dt)^{0.5}}\right)\right)\,dx \quad \text{EQUATION 6.9}$$

where *T* is the substrate thickness, we get the area under the diffusion profile and from this the total amount of carbon that has diffused into the substrate from the liquid melt may be ascertained. The mass of carbon that has diffused into the substrate may be calculated using Equation 6.10

$$\text{Mass of Carbon} = \text{Mass of Substrate} \times \left(\frac{\text{Area Under Curve}}{(T \times 100)}\right) \qquad \text{EQUATION 6.10}$$

This carbon was removed from the liquid white iron prior to the formation of an interfacial layer containing 1.6wt.% carbon. Once sufficient iron has entered the melt and the austenitic rim is about to form, carbon continues to diffuse into the substrate and the interfacial layer is left behind. Thermocalc predicts this interfacial layer will have a density of 7.46g.cm^{-3} at 1250°C so the density of carbon removed from the melt to form this layer will be 0.1865 g.cm^{-3}, (7.46*(4.1%*-1.6%). By dividing the mass of carbon that has been removed, Equation 6.10, from the melt by this density, the total volume of the interfacial layer may be obtained and when the surface area of the substrate is taken into account, the thickness of the interfacial layer may be calculated. Figure 6.24 shows the predicted thickness of a composite containing 500 g of white iron with a substrate surface area of 8500 mm^2.

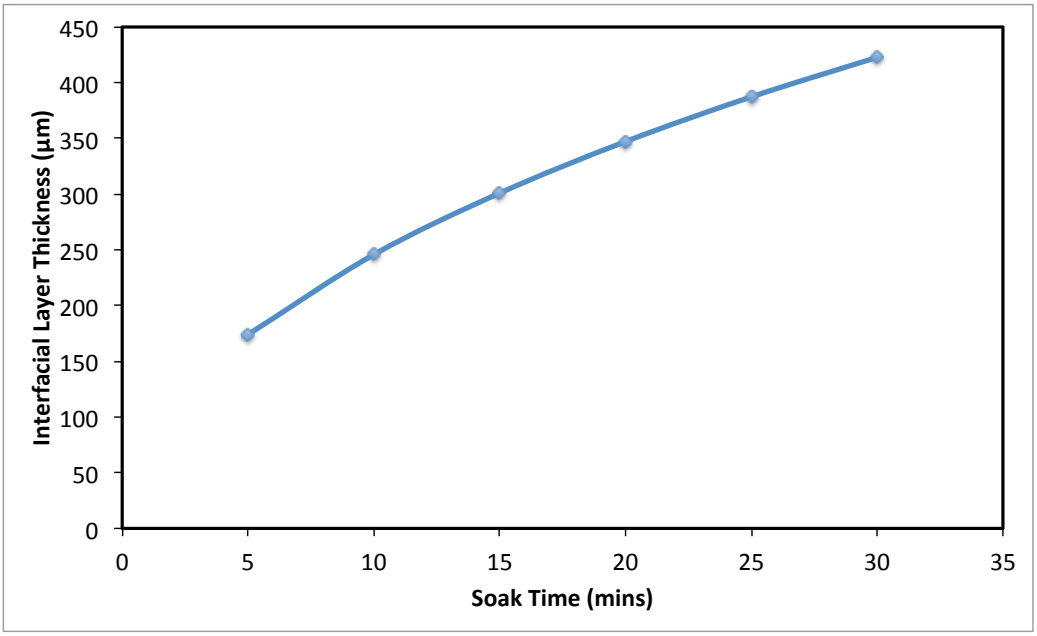

Figure 6.24: Predicted interface thickness of composite containing 500 g liquid white iron and 8500 mm^2 substrate area.

From these results it can be seen that the predicted thickness of the interfacial layer is about three times greater than the thicknesses found experimentally. However, this result is not unexpected as the model does not include a boundary layer with varying levels of carbon depletion, and it simply assumes a constant concentration of 4.1wt.% carbon in the melt. What is important in these simulations is that, with soak times of 5 minutes and greater, the relationship between soak time and interfacial layer thickness is very close to linear.

6.4 Chapter Conclusions

In this chapter, the diffusive mass transfer that governs the formation of the interfacial bond between the molten white iron and the steel substrate has been modelled. As shown in the previous chapter, the interfacial layer has formed via epitaxial growth of austenite from the liquid white iron upon the high temperature austenite of the mild steel substrate. Diffusion profiles of experimental samples were created using both energy dispersive spectroscopy and wavelength dispersive spectroscopy and were compared with theoretical diffusion profiles created based on Grube's solution to Fick's

second law. It was found that the theoretical diffusion profiles matched very closely with the profiles that were obtained experimentally.

The formation of the interfacial layer was also studied using two complementary theoretical techniques. A powerful diffusion simulation package called DICTRA was used to predict the diffusion of elements from the white iron into the steel substrate and the subsequent effect on the interface. This was then compared to a custom-written model which invoked Grube's diffusion equation, pre-calculated phase diagrams (using Thermocalc) and a mass balance to predict the behaviour of the interface. Both approaches provided a satisfactory explanation for the observed results. In summary, they predicted the diffusion of carbon into the steel substrate, which subsequently reduced the melting point of the steel directly adjacent to the interface between the liquid and solid substrate. Effectively, the liquid white iron dissolved this layer. With the loss of carbon from the steel and diffusion of iron into the liquid white iron from the steel, the liquidus of the neighbouring liquid white iron increases and, finally, a layer of austenite is deposited on the steel substrate. The layer increases in thickness with time at a linear rate with long soak times, as observed experimentally.

CHAPTER 7 CONCLUDING REMARKS

The purpose of this work was to elucidate the interfacial phenomena that occur when white cast iron is cast against a steel substrate. The project was motivated by a desire to develop a technique by which high wear parts may be created in both a cost-effective and energy-efficient fashion. There have been a variety of techniques that have been employed in the past to create parts of this nature but all have their limitations in terms of efficiency or in their ability to create parts of a complex geometry. It was hoped that the proposed kiln casting scheme would offer an improvement.

In the second chapter of this thesis, it was shown that white irons are a very suitable alternative to hardened steels in applications that experience a high degree of abrasive wear. However, their inherent low fracture toughness restricts their usage as the sole material in parts experiencing high impact but may provide useful in circumstances where a more ductile material is used as a substrate and the white iron is used as a wear layer.

The white iron chosen in this thesis is a low melting point (M.P. = 1209°C) white iron developed by Huggett and Ben-Nissan[27]. This alloy was chosen as it possesses a relatively high volume fraction of carbides (CVF = 29%) and two benefits come from the fact that it melts at a low temperature; firstly less energy will be required to melt the alloy and secondly the degree of oxidation of the steel substrate will be reduced.

In the third chapter the question of how best to avoid oxidation of the substrate was examined. The composition of the substrate and the nature of the processing conditions were considered. It was confirmed that use of substrates of either type 310 and 253MA stainless steel would result in far less oxidation than mild steel at the 1250°C processing temperature. In addition some alleviation of oxidation could be gained by performing the casting in an inert atmosphere of argon.

Type 310 stainless steel exhibited better oxidation resistance than the 253MA stainless steel as well as higher maximum flexural stress and a higher flexural modulus. Mild steel exhibited slightly lower mechanical properties than type 310 stainless steel but

due to the low quantities of alloying elements and the possibility of oxide protection via coatings or inert atmosphere, it is an enticing prospective substrate material.

In the fourth chapter, type 310 stainless steel was used as a substrate and the low melting point white iron was cast onto it. Counter-current mass transfer occurs the solid-liquid interface when white cast iron is melted against a type 310 substrate with carbon diffusing into the steel via both the grain boundaries and solid state volume diffusion. The excess carbon results in the formation of carbides along the prior austenite grain boundaries and specifically at the junctions between the grain boundaries. Nickel, in contrast, diffused in the other direction, from the steel substrate into the liquid white iron. A good metallurgical bond can be obtained even if melting is conducted in air. Use of X-ray mapping in a SEM revealed extensive diffusion of iron, chromium, nickel and subsequently carbon, and the individual analyses could be combined to yield a detailed understanding of the microstructure. The microstructure could be further characterized using nano-indentation transects, which provided a confirmation of the zonation determined using compositional metallography.

The next chapter described a detailed study into the formation of the interface during the kiln casting of WCI onto a mild steel substrate. The effect of soaking time was specifically examined. Soaking the composite at 1250°C for 10 minutes or longer eliminated porosity on the interface, which provided time for any carbon monoxide bubbles formed to migrate out to the free surface of the composite through the still molten liquid cast iron. An austenitic interfacial layer was found to develop between white iron and the steel, by epitaxial growth from the melt onto the austenite of the substrate. This layer was retained to room temperature due its high degree of alloying, but the unalloyed austenite of the mild steel substrate reverted back to a ferrite plus pearlite mixture on cooling.

Through the usage of combined EDS and WDS X-Ray mapping, qualitative and quantitative data was obtained showing spatial distribution and chemical composition of the various microconstituents. The thickness of this interfacial layer was measured using both *ex*- and *in-situ* techniques and it was found that this interfacial layer grew linearly with soak time.

In order to confirm these findings, high temperature laser scanning confocal microscopy was employed to examine the formation of this interfacial layer *in-situ*. This technique confirmed that a seven stage process is occurring in the creation of these composites:

1. Melting of the white iron
2. Initial partial dissolution of the steel substrate
3. Increase in iron and decrease in carbon of the liquid adjacent to the substrate
4. Increase in the melting point of the interfacial liquid until it begins to grow as a rim of austenite.
5. Planar growth of austenite and an associated inwards diffusion of carbon across the newly formed interfacial layer.
6. Once the soak is ended, solidification of the remaining white iron.
7. Solid-state precipitation of hypereutectoid Fe_3C carbides as the austenite cools through the two-phase austenite plus Fe_3C phase field.

In the final chapter of experimental data, the diffusion phenomena that govern the formation of the interfacial bond between white iron and the steel substrate were investigated. As shown in chapter 5, the interfacial layer has formed via epitaxial growth of austenite from the liquid white iron upon the (high temperature) austenitic steel substrate. Diffusion profiles of experimental samples were measured using both energy dispersive spectroscopy and wavelength dispersive spectroscopy and were compared with theoretical diffusion profiles created based on Grube's solution to Fick's second law. It was found that the theoretical diffusion profiles matched very closely with the profiles that were obtained experimentally.

The formation of the interfacial layer was also studied using theoretical techniques. A simulation package called DICTRA was used to predict the extent of the diffusion of carbon into the steel substrate. This information was coupled with the reduction in the melting point of the steel directly adjacent to the interface to produce as estimate of the position of the solid/liquid interface as a function of time. The DICTRA simulation confirmed that, with the loss of carbon from the steel and diffusion of iron into the liquid white iron from the steel, the liquidus of the neighbouring liquid white iron increases and a layer of austenite is deposited on the steel substrate. This newly formed interfacial layer increases in thickness with time. The rate of growth could be matched

to that of the experimental findings of the previous chapter by adjustment of the simulation's 'labyrinth' parameter. A model based on Grube's solution to Fick's law produced a similar result.

This thesis has shown by a variety of techniques that a strong metallurgical bond between a steel substrate and a highly wear resistant white can be created in a standard air atmosphere. The phenomena occurring during the formation of such joins have been elucidated and found to be relatively complex. Two aspects stand out as being especially important: these are the removal of porosity due to the generation of bubbles of CO, and the subsequent controlled development of an interfacial layer of desired thickness and microstructure. Provided these issues are understood and controlled, the kiln casting technique can be easily carried out in non-specialised furnace equipment with relatively cheap starting materials.

APPENDIX 1

```
@@ exb1c_setup.DCM

@@ WE START BY GOING TO THE DATABASE MODULE.

go da

@@ LET US USE THE SSOL DATABASE FOR THERMODYNAMIC DATA

sw tcfe6 and mark

@@ DEFINE WHAT SYSTEM WE WANT TO WORK WITH

def-species fe c cr mn si ni

@@ EXCLUDE THE THERMODYNAMIC DATA FOR THE PHASES THAT IS NOT NEEDED

rej ph * all

res ph liquid fcc

@@ RETRIEVE DATA FROM DATABASE FILE

get

@@ MOBILITY/DIFFUSIVITY DATA ARE STORED ON A SEPARATE DATABASE FILE.

@@ SWITCH TO MOBILITY DATABASE TO RETRIEVE DATA

pp

mob2

def-sys fe c cr mn si ni

rej ph * all

res ph liquid fcc

get

@@ ENTER THE DICTRA MONITOR WHERE WE WILL SETUP OUR SYSTEM

go d-m
```

@@self

@@fe-fe

am-mob dq(liquid&fe,fe;0)

y

298.15+R*T*LN(1E-06); 6000 n

@@mn-mn

am-mob dq(liquid&mn,mn;0)

y

298.15+R*T*LN(1E-06); 6000 n

@@cr-cr

am-mob dq(liquid&cr,cr;0)

y

298.15+R*T*LN(1E-06); 6000 n@

@@c-c

am-mob dq(liquid&c,c;0)

y

298.15+R*T*LN(1E-06); 6000 n

@@si-si

am-mob dq(liquid&si,si;0)

y

298.15+R*T*LN(1E-06); 6000 n

@@ni-ni

am-mob dq(liquid&ni,ni;0)

y

298.15+R*T*LN(1E-06); 6000 n

@@fe

am-mob dq(liquid&fe,mn;0)

y

298.15+R*T*LN(1E-06); 6000 n

@@mn-mn

am-mob dq(liquid&fe,cr;0)

y

298.15+R*T*LN(1E-06); 6000 n

@@s-s

am-mob dq(liquid&fe,c;0)

y

298.15+R*T*LN(1E-06); 6000 n

am-mob dq(liquid&fe,si;0)

y

298.15+R*T*LN(1E-06); 6000 n

am-mob dq(liquid&fe,ni;0)

y

298.15+R*T*LN(1E-06); 6000 n

@@mn

am-mob dq(liquid&mn,fe;0)

y

298.15+R*T*LN(1E-06); 6000 n

@@mn-mn

am-mob dq(liquid&mn,cr;0)

y

298.15+R*T*LN(1E-06); 6000 n

@@s-s

am-mob dq(liquid&mn,c;0)

y

298.15+R*T*LN(1E-06); 6000 n

am-mob dq(liquid&mn,si;0)

y

298.15+R*T*LN(1E-06); 6000 n

am-mob dq(liquid&mn,ni;0)

y

298.15+R*T*LN(1E-06); 6000 n

@@cr

am-mob dq(liquid&cr,fe;0)

y

298.15+R*T*LN(1E-06); 6000 n

@@mn-mn

am-mob dq(liquid&cr,mn;0)

y

298.15+R*T*LN(1E-06); 6000 n

@@

am-mob dq(liquid&cr,c;0)

y

298.15+R*T*LN(1E-06); 6000 n

am-mob dq(liquid&cr,si;0)

y

298.15+R*T*LN(1E-06); 6000 n

am-mob dq(liquid&cr,ni;0)

y

298.15+R*T*LN(1E-06); 6000 n

@@c

am-mob dq(liquid&c,fe;0)

y

298.15+R*T*LN(1E-06); 6000 n

@@

am-mob dq(liquid&c,mn;0)

y

298.15+R*T*LN(1E-06); 6000 n

@@

am-mob dq(liquid&c,cr;0)

y

298.15+R*T*LN(1E-06); 6000 n

am-mob dq(liquid&c,si;0)

y

298.15+R*T*LN(1E-06); 6000 n

am-mob dq(liquid&c,ni;0)

y

298.15+R*T*LN(1E-06); 6000 n

@@si

am-mob dq(liquid&si,fe;0)

y

298.15+R*T*LN(1E-06); 6000 n

@@

am-mob dq(liquid&si,mn;0)

y

298.15+R*T*LN(1E-06); 6000 n

am-mob dq(liquid&si,cr;0)

y

298.15+R*T*LN(1E-06); 6000 n

am-mob dq(liquid&si,c;0)

y

298.15+R*T*LN(1E-06); 6000 n

am-mob dq(liquid&si,ni;0)

y

298.15+R*T*LN(1E-06); 6000 n

@@ni

am-mob dq(liquid&ni,fe;0)

y

298.15+R*T*LN(1E-06); 6000 n

@@

am-mob dq(liquid&ni,mn;0)

y

298.15+R*T*LN(1E-06); 6000 n

@@

am-mob dq(liquid&ni,cr;0)

y

298.15+R*T*LN(1E-06); 6000 n

am-mob dq(liquid&ni,c;0)

y

298.15+R*T*LN(1E-06); 6000 n

am-mob dq(liquid&ni,si;0)

y

298.15+R*T*LN(1E-06); 6000 n

@@ ENTER GLOBAL CONDITION T.

@@ WE ASSUME THAT THE COOLING RATE IS 10K/MINUTE DOWN TO 1050K.

set-cond glob t 0 1527; * n

@@ WE START BY ENTERING REGION austenite WHEREIN WE PUT THE fcc PHASE

enter-region

fcc

enter-region

liquid

@@ ENTER GRID INTO THE REGION.

enter-grid

fcc

3e-3

lin

200

enter-grid

liquid

1e-2

lin

200

@@ ENTER ACTIVE PHASES INTO REGIONS

enter-phase

act

fcc

matrix

fcc

@@ ENTER INACTIVE PHASES INTO REGIONS

enter-phase

act

liquid

matrix

liquid

@@ ENTER INITIAL COMPOSITION INTO FCC.

enter-composition

fcc

fcc#1

fe

w-p

C lin 0.2 0.2

cr lin 0.01 0.01

mn lin 0.01 0.01

si lin 0.01 0.01

ni lin 0.01 0.01

```
enter-composition
liquid
liquid#1
fe
w-p
C lin 4.1 4.1
mn lin 1.6 1.6
cr lin 12.0 12.0
si lin 0.5 0.5
ni lin 1.0 1.0
@@ BOUNDARY CONDITION WILL BE A CLOSED SYSTEM AS WE DO NOT SPECIFY
@@ ANYTHING ELSE.
ent-geo 0
@@ SET THE SIMULATION TIME
set-simulation-time
1200
10
@@ WE USE IMPLICIT (1) TIME INTEGRATION IN THIS CASE INSTEAD OF THE
@@ MORE ACCURATE BUT LESS STABLE TRAPETZOIDAL METHOD WHICH IS THE
@@ DEFAULT METHOD.
s-s-c
yes
0.5
s-n-l
1e-16
```

1e-5

@@ SAVE THE SETUP ON A NEW STORE FILE AND EXIT DICTRA

save lmkc03 Y

set-inter

exit

REFERENCES

1. Walton, C.F., ed. *Grey and Ductile Iron Castings Handbook*. 1971, Grey and Ductile Iron Founders Society Inc.: Cleveland.
2. Baker, H., ed. *Alloy Phase Diagrams*. Vol. 3. 1992, ASM International.
3. ASTM, *A 48 - Standard Specification for Gray Iron Castings*, 2003 (Reapproved 2008).
4. Davies, J.R., ed. *Cast Irons*. 1996, ASM International.
5. ASTM, *A 532 - Standard Specification for Abrasion-Resistant Cast Irons*, 1993 (Reapproved 2008).
6. ASTM, *A 536 - Standard Specification for Ductile Iron Castings*, 1984 (Reapproved 2009).
7. ASTM, *A 47 - Standard Specification for Ferritic Malleable Iron Castings*, 1999 (Reapproved 2009).
8. Durand-Charre, M., *La Microstructure des aciers et des fontes. (Microstructure of Steels and Cast Irons)*2003: Springer.
9. Powell, G.L.F. and P.G. Lloyd, *A Deep Etching Technique for the Examination of the Carbide of High Chromium Cast Iron in a Scanning Electron Microscope.* Metallography, 1980. **14**(1): p. 37-46.
10. Aleksandrov, N.A. and N.S. Gushchin, *Effect of silicon and of inoculation of the melt on the stability of austenite in cooling of chromium-nickel cast iron.* Metal Science and Heat Treatment, 2006. **48**(7-8): p. 287-289.
11. Rabinowicz, E., *Friction and wear of materials*1965: Wiley.
12. Avery, H.S., *The measurement of wear resistance.* Wear, 1961. **4**(6): p. 427-449.
13. Zum Gahr, K., *Microstructure and wear of materials*. Tribology Series. Vol. 10. 1987: Elsevier.
14. Burwell, J.T. and C.D. Strang, *On the Empirical Law of Adhesive Wear.* Journal of Applied Physics, 1952. **23**(1): p. 18-28.
15. Jahanmir, S., *On the wear mechanisms and the wear equations.* Fundamentals of Tribology, 1978. **6**: p. 455-467.
16. Godfrey, D., *Diagnosis of wear mechanisms.* Wear Control Handbook, 1980: p. 283-311.

17. Rice, S.L., *Diagnosis of wear mechanisms.* A Review of Wear Mechanisms and Related Topics, 1980: p. 469-476.
18. DIN-50320, *Verschleib - Bergriffe, Analyse von Verschleibvorgangen, Gleiderung des Verschleibgebietes*, 1979, Beuth Verlag: Berlin.
19. Mutton, P.J., *Abrasion Resistant Materials for the Australian Minerals Industry*1988: AMIRA.
20. ASTM, *G 40 - Standard Terminology Relating to Wear and Erosion*, 2005.
21. Hutchings, I.M., *Tribology: Friction and Wear of Engineering Materials*1992, London: Edward Arnold.
22. Watson, J.D., P.J. Mutton, and I.R. Sare, *Abrasive Wear of White Cast Irons*. Metals Forum. Vol. 3. 1980.
23. Stauffer, W.A., *The Abrasion of Hydraulic Plant by Sandy Water.* CE Trans 1799, Schweizer Archiv fur Angewandte Wissenschaft und Technik, 1958. **24**(7/8): p. 3-30.
24. Bungardt, K., E. Kunze, and E. Hom, *Investigation of the Structure of the Iron-Chromium-Carbon System.* Archiv Eisenhucttenwes, 1958. **29**: p. 193-203.
25. Jackson, R.S., *The Austenite Liquidus Surface and Constitutional Diagram for the Fe-Cr-C Metastable System.* Journal of the Iron and Steel Institute, 1970. **208**: p. 163–167.
26. Thorpe, W.R. and B. Chico, *The Fe-Rich Corner of the Metastable C-Cr-Fe Liquidus Surface.* Metallurgical Transactions, 1985. **16A**: p. 1541-1549.
27. Huggett, P.G. and B. Ben-Nissan, *Development Of A Low Melting Point White Cast Iron For Use In Composite Alloy Manufacture.* Materials Forum, 2007. **31**: p. 16-23.
28. Schön, C.G. and A. Sinatora, *Simulation of solidification paths in high chromium white cast irons for wear applications.* Calphad, 1998. **22**(4): p. 437-448.
29. Nelson, G.D., G.L.F. Powell, and W.M. Linton, *Investigation of the wear resistance of high chromium white irons*, in *Surface Modification Technologies*, T.S. Sudarshan and J.J. Stiglich, Editors. 2006, ASM International: Materials Park. p. 111-118.
30. Cortie, M.B., J.J. McEwan, and D.P. Enright, *Materials selection in the mining industry : New issues and old challenges. .* Journal of the South Afican Institute of Mining and Metallurgy, 1996. **96**(4): p. 145-157.

31. Chung, R.J., et al., *Abnormal erosion–slurry velocity relationship of high chromium cast iron with high carbon concentrations.* Wear, 2011. **271**: p. 1454-1461.
32. Zum Gahr, K.-H. and D. Doane, *Optimizing fracture toughness and abrasion resistance in white cast irons.* Metallurgical and Materials Transactions A, 1980. **11**(4): p. 613-620.
33. Arnold, B.K., et al., *Wear of cast-bonded components in a coal pulveriser mill.* Wear, 1997. **203-204**: p. 663-670.
34. Buchely, M.F., et al., *The effect of microstructure on abrasive wear of hardfacing alloys.* Wear, 2005. **259**(1-6): p. 52-61.
35. Coronado, J.J., H.F. Caicedo, and A.L. Gómez, *The effects of welding processes on abrasive wear resistance for hardfacing deposits.* Tribology International, 2009. **42**(5): p. 745-749.
36. Huggett, P.G., et al., *A novel metallurgical bonding process and microstructural analysis of ferrous alloy composites.* Materials Forum, 2005. **29**: p. 83-88.
37. Huggett, P.G., et al., *Composite alloy wear parts for use in the mining industry.* Materials Forum, 2006. **30**: p. 23-29.
38. Sapate, S.G. and A.V. RamaRao, *Erosive wear behaviour of weld hardfacing high chromium cast irons: effect of erodent particles.* Tribology International, 2006. **39**(3): p. 206-212.
39. Huggett, P.G., et al., *A novel metallurgical bonding process and microstructural analysis of ferrous alloy composites.* Mater. Forum, 2005. **29**: p. 83-88.
40. Coronado, J.J., H.F. Caicedo, and A.L. Gómez, *The effects of welding processes on abrasive wear resistance for hardfacing deposits.* Tribology Internat., 2009. **42**(5): p. 745-749.
41. Sapate, S.G. and A.V. RamaRao, *Erosive wear behaviour of weld hardfacing high chromium cast irons: effect of erodent particles.* Tribology Internat., 2006. **39**(3): p. 206-212.
42. Chang, C.-M., et al., *Micro-structural characteristics of Fe-40 wt%Cr-xC hardfacing alloys with [1.0-4.0 wt%] carbon content.* Journal of Alloys and Compounds, 2009.
43. Huggett, P.G., *Production and Analysis of Alloy Composites Exhibiting Improved Bonding Using a Novel Vacuum Casting Process*, in *Chemistry and Forensics,* 2008, University of Technology: Sydney.
44. Stone, M., *Centrifugal casting of bi-metal rolls*, 1973, Wean United Inc: USA.

45. *Centrifugal Casting - Union Electric Steel*. 2013; Available from: http://www.uniones.com/the-ues-difference/cast-roll-technology/centrifugal-casting.
46. *Centrifugal casting - Akers Group*. 2013; Available from: http://www.akersrolls.com/templates/TwoColumnList___555.aspx.
47. Paidassa, J., *The Kinetics of the Oxidation of Iron in the Range 700-1250°C.* Acta Metallurgica, 1958. **6**: p. 184-194.
48. Engell, H.J., *The Concentration Gradient of Iron-Ion-Vacancies in Wustite Scaling Films and the Mechanism of Oxidation of Iron.* Acta Metallurgica, 1958. **6**: p. 439-445.
49. Poirier, D., et al., *High Temperature Oxidation of Steel in an Oxygenenriched Low NOX Furnace Environment.* IFRF Combustion Journal, 2006.
50. Di Giampaolo Conde, A.R., et al., *Thick aluminosilicate coatings on carbon steel via sol-gel.* Journal of Non-Crystalline Solids, 1992. **147-148**(C): p. 467-473.
51. Atik, M., et al., *Films for Stainless Steel Corrosion Protection.* Journal of Sol-Gel Science and Technology, 1997. **8**(1): p. 517-522.
52. Shane, M. and M.L. Mecartney, *Sol-gel synthesis of zirconia barrier coatings.* Journal of Materials Science, 1990. **25**(3): p. 1537-1544.
53. Di Maggio, R., et al., *Dry and wet corrosion behaviour of AISI 304 stainless steel coated by sol-gel ZrO2---CeO2 films.* Thin Solid Films, 1996. **286**(1-2): p. 127-135.
54. Czerwinski, F. and W.W. Smeltzer, *The growth and structure of thin oxide films on ceria-sol-coated nickel.* Oxidation of Metals, 1993. **40**(5): p. 503-527.
55. Mei, L.F., K. M. Liang, and H.B. Li, *The Effect of Zirconia Sol-Gel Coatings on Mild Steel Oxidation Resistance.* Key Engineering Materials, 2005. **280 - 283**(High-Performance Ceramics III): p. 1005-1008.
56. Shi, Z.M., et al., *Oxidation Resistance of Mild Steels Coated with Ce4+-Modified TiO2 Nanofilms.* Key Engineering Materials, 2007. **336 - 338**(High-Performance Ceramics IV): p. 1930-1932.
57. Li, H., et al., *Oxidation resistance of mild steel by zirconia sol-gel coatings.* Materials Science and Engineering A, 2003. **341**(1-2): p. 87-90.
58. Guglielmi, M., *Sol-gel coatings on metals.* Journal of Sol-Gel Science and Technology, 1997. **8**(1): p. 443-449.

59. Hirai, S., et al., *Alkaline Corrosion Resistance of Anodized Aluminum Coated with Zirconium Oxide by a Sol-Gel Process.* Journal of the American Ceramic Society, 1998. **81**(12): p. 3087-3092.
60. Izumi, K., et al., *Zirconia Coating on Stainless Steel Sheets from Organozirconium Compounds.* Journal of the American Ceramic Society, 1989. **72**(8): p. 1465-1468.
61. *Steel Plant Specialties*. Available from: http://www.steelplantspecialities.com/.
62. Bika, D., et al., *Sulfur-induced dynamic embrittlement in a low-alloy steel.* Acta Metallurgica et Materialia, 1995. **43**(5): p. 1895-1908.
63. Sargent, L.B., *Titanium Fabrication*, in *United States Patent Office* 1971, Aluminium Company of America.
64. Blickensderfer, R. and J.H. Tylczak, *A large-scale impact spalling test.* Wear, 1983. **84**(3): p. 361-373.
65. Bochnowski, W., et al., *Primary and secondary carbides in high-speed steels after conventional heat treatment and laser modification.* Materials Chemistry and Physics, 2003. **81**(2-3): p. 503-506.
66. Takahashi, S., *Method for continuous heat-treatment of metal under argon atmosphere*, in *European Patent Office*2005, Kanto Yakin Kabushiki Kaisha Hiratsuka-shi, Kanagawa-ken: Japan.
67. Knight, D.G., *Method of heat treating ferrous metal articles under controlled furnace atmosphere*, in *United States Patent Office*1983, Air Products and Chemicals, Inc.: England.
68. Gurry, R., *Composition of Atmospheres Inert to Heated Carbon Steel.* Journal of Metals, 1950. **188**: p. 671-687.
69. Guillet, L., *Nickel-Chrome Steels.* Revue de Metallurgie, 1906. **3**(1): p. 332.
70. Colombier, L. and J. Hochmann, *Stainless and Heat Resisting Steels*1968, New York: St Martin's Press.
71. Klueh, R.L. and D.R. Harries, *High-Chromium Ferritic and Martensitic Steels for Nuclear Applications*2001: ASTM. 220.
72. Crafts, W., *Chromium in Steel*, in *Metals Handbook*1948, American Society For Metals.
73. Van Zwieten, A.C.T.M. and J.H. Bulloch, *Some considerations on the toughness properties of ferritic stainless steels--A brief review.* International Journal of Pressure Vessels and Piping, 1993. **56**(1): p. 1-31.

74. Demo, J.J., *Structure, Constitution and General Characteristics of Wrought Ferritic Stainless Steels*, in *ASTM STP 619*1977, American Society for Testing and Materials.
75. Gulyaev, A.P. and A.N. Levanova, *Brittleness of high-chromium ferritic stainless steels.* Metal Science and Heat Treatment, 1978. **20**(11): p. 881-886.
76. Grubb, J. and R. Wright, *The role of C and N in the brittle fracture of Fe-26 Cr.* Metallurgical and Materials Transactions A, 1979. **10**(9): p. 1247-1255.
77. Binder, W.R. and H.O. Spendlow, *The Influence of Chromium on the Mechanical Properties of Plain Chromium Steels.* Transactions of the American Metals Society, 1951. **43**: p. 759-777.
78. Hochmann, J., *Properties of Vacuum-Melted Steels Containing 25%. Chromium.* Revue de Metallurgie, 1951. **48**: p. 734-758.
79. Peckner, D. and I.M. Bernstein, *Handbook of Stainless Steels*1977: McGraw-Hill, Inc.
80. Brasunas, A., J.T. Gow, and D.E. Harder, *Resistance of Iron-Nickel-Chromium Alloys to Corrosion in Air at 1600-2200°F*, in *Symposium on Materials for Gas Turbines* 1946, ASTM International.
81. Nakamura, Y., *The Oxidation behavior of an iron-chromium alloy containing yttrium or rare earth elements between 900° and 1200°C.* Metallurgical and Materials Transactions B, 1974. **5**(4): p. 909-913.
82. Ramanathan, L.V., *Role of rare-earth elements on high temperature oxidation behavior of Fe-Cr, Ni-Cr and Ni-Cr-Al alloys.* Corrosion Science, 1993. **35**(5-8): p. 871-875, 877-878.
83. Andrews, K.W., *Empirical Formulae for the Calculation of Some Transformation Temperatures.* Journal of theIron and Steel Institute, 1965. **203**(7): p. 721-727.
84. Skinner, E.N., J.F. Mason, and J.J. Moran, *High Temperature Corrosion in Refinery And Petrochemical Service.* Corrosion, 1960. **16**(12): p. 593t-600t.
85. Lucey, T., et al., *Supplemental Proceedings: Materials, Properties, Characterization and Modelling*2012: John Wiley & Sons, Inc.
86. Lucey, T., et al., *Interfacial reactions in white iron/steel composites.* Journal of Materials Processing Technology, 2012. **212**(11): p. 2349-2357.

87. Chang, C.-M., et al., *Micro-structural characteristics of Fe-40 wt%Cr-xC hardfacing alloys with [1.0-4.0 wt%] carbon content.* J. Alloys Compd., 2009. **487**(1-2): p. 83-89.
88. Borgenstam, A., et al., *DICTRA, a tool for simulation of diffusional transformations in alloys.* Journal of Phase Equilibria, 2000. **21**(3): p. 269-280.
89. Turpin, T., J. Dulcy, and M. Gantois, *Carbon diffusion and phase transformations during gas carburizing of high-alloyed stainless steels: Experimental study and theoretical modeling.* Metallurgical and Materials Transactions A, 2005. **36**(10): p. 2751-2760.
90. Moran, K. and R. Wuhrer, *Quantitative bulk and trace element X-ray mapping using multiple detectors.* Microchimica Acta, 2006. **155**(1-2): p. 59-66.
91. Moran, K. and R. Wuhrer, *X-Ray mapping and interpretation of scatter diagrams.* Microchimica Acta, 2006. **155**(1-2): p. 209-217.
92. Computational Thermodynamics Inc. *Metastable Iron-Carbon (Fe-C) Phase Diagram*. 2011; Available from: http://www.calphad.com/iron-carbon.html.
93. Graham, T., *On the Law of the Diffusion of Gases.* The American Journal of the Medical Sciences, 1833. **23**: p. 189-193.
94. Fick, A., *On liquid diffusion.* Philosophical Magazine Series 4, 1855. **10**(63): p. 30 - 39.
95. Arrhenius, S., *Über die Reaktionsgeschwindigkeit bei der Inversion von Rohrzucker durch Säuren.* Zeitschrift für physikalische Chemie, 1889. **4**: p. 224-248.
96. Kirkendall, E., L. Thomassen, and C. Upthegrove, *Rates of diffusion of copper and zinc in alpha brass.* Transactions of the American Institute of Mining, Metallurgical and Petroleum Engineers, 1939. **133**: p. 186.
97. Cussler, E.L., *Diffusion: Mass Transfer in Fluid Systems*1994, NY, USA: Cambridge University Press.
98. Glicksman, M.E., *Diffusion in Solids: Field Theory, Solid-State Principles and Applications* 2000, NY, USA: Wiley.
99. Shewmon, P., *Diffusion in Solids*1989, USA: The Minerals, Metals and Materials Society.
100. Brown, R., *A Brief account of microscopical observations made in the months of June, July and August 1827 on the particles contained in the pollen of plants*, 1828.

101. Einstein, A., *Über die von der molekularkinetischen Theorie der Wärme geforderte Bewegung von in ruhenden Flüssigkeiten suspendierten Teilchen.* Annalen der Physik, 1905. **322**(8): p. 549-560.
102. Huntington, H.B., *Self-Consistent Treatment of the Vacancy Mechanism for Metallic Diffusion.* Physical Review, 1942. **61**(5-6): p. 325-338.
103. Huntington, H.B. and F. Seitz, *Mechanism for Self-Diffusion in Metallic Copper.* Physical Review, 1942. **61**(5-6): p. 315-325.
104. Jefferies, Z., *The Trend in the Science of Metals.* Trans. AIME, 1924. **70**: p. 303.
105. Kirkendall, E., *Diffusion of zinc in alpha brass.* Transactions of the American Institute of Mining, Metallurgical and Petroleum Engineers, 1942. **147**: p. 104.
106. Faupel, F., et al., *Diffusion in metallic glasses and supercooled melts.* Reviews of Modern Physics, 2003. **75**(1): p. 237-280.
107. Mehrer, H., *Atomic jump processes in self-diffusion.* Journal of Nuclear Materials, 1978. **69**(0): p. 38-60.
108. Peterson, N.L., *Self-diffusion in pure metals.* Journal of Nuclear Materials, 1978. **69**(0): p. 3-37.
109. Barnes, R.S., *Diffusion of Copper along the Grain Boundaries of Nickel.* Nature, 1950. **166**(4233): p. 1032-1033.
110. Fisher, J.C., *Calculation of Diffusion Penetration Curves for Surface and Grain Boundary Diffusion.* Journal of Applied Physics, 1951. **22**(1): p. 74-77.
111. Le Claire, A.D., *The analysis of grain boundary diffusion measurements.* British Journal of Applied Physics, 1963. **14**(6): p. 351.
112. Harrison, L.G., *Influence of dislocations on diffusion kinetics in solids with particular reference to the alkali halides.* Transactions of the Faraday Society, 1961. **57**: p. 1191-1199.
113. Belova, I.V. and G.E. Murch, *The transition from Harrison type-B to type-A kinetics in grain-boundary tracer diffusion.* Philosophical Magazine A, 2001. **81**(10): p. 2447-2455.
114. Hart, E.W., *On the role of dislocations in bulk diffusion.* Acta Metallurgica, 1957. **5**: p. 597.
115. Sommer, J. and C. Herzig, *Direct determination of grain-boundary and dislocation self-diffusion coefficients in silver from experiments in type-C kinetics.* Journal of Applied Physics, 1992. **72**(7): p. 2758-2766.

116. Gruzin, P.L., V.G. Kostogonov, and P.A. Platonov, *USE OF CARBON ISOTOPE C14 FOR INVESTIGATION OF THE DIFFUSION OF CARBON IN STEEL.* Journal Name: Doklady Akad. Nauk S.S.S.R., 1955. **100**: p. 1069-72.
117. Bowen, A. and G. Leak, *Diffusion in Bcc iron base alloys.* Metallurgical and Materials Transactions B, 1970. **1**(10): p. 2767-2773.
118. K. Nohara and K. Hirano. *Diffusion 54Mn in iron and iron-manganese alloys*. in *Proc. Intl. Conf. Sci. and Technol. Iron and Steel*. 1970.
119. Borg, R.J. and D.Y.F. Lai, *The diffusion of gold, nickel, and cobalt in alpha iron: A study of the effect of ferromagnetism upon diffusion.* Acta Metallurgica, 1963. **11**(8): p. 861-866.
120. Hirano, K., M. Cohen, and B.L. Averbach, *Diffusion of nickel into iron.* Acta Metallurgica, 1961. **9**(5): p. 440-445.
121. Badia, M. and A. Vignes, *Iron, nickel and cobalt diffusion in transition metals of iron group.* Acta Metallurgica, 1969. **17**(2): p. 177-187.
122. Gale, W.F. and T.C. Totemeier, *Smithells Metals Reference Book (8th Edition)*, Elsevier.
123. Fridberg, J., L.E. Terndahl, and M. Hillert, *Diffusion in Iron.* Jernkontorets Annaler, 1969. **153**: p. 274.
124. Kirkaldy, J.S., *DIFFUSION IN MULTICOMPONENT METALLIC SYSTEMS: I. PHENOMENOLOGICAL THEORY FOR SUBSTITUTIONAL SOLID SOLUTION ALLOYS.* Canadian Journal of Physics, 1958. **36**(7): p. 899-906.
125. Kodentsov, A.A., G.F. Bastin, and F.J.J. van Loo, *The diffusion couple technique in phase diagram determination.* Journal of Alloys and Compounds, 2001. **320**(2).
126. Kuntz, M.L., S.F. Corbin, and Y. Zhou, *Quantifying metallurgical interactions in solid/liquid diffusion couples using differential scanning calorimetry.* Acta Materialia, 2005. **53**(10).
127. Tanaka, Y. and M. Kajihara, *Evaluation of Interdiffusion in Liquid Phase During Reactive Diffusion Between Cu and Al.* Materials Transactions, 2006. **47**(10).
128. Turpin, T., J. Dulcy, and M. Gantois, *Carbon diffusion and phase transformations during gas carburizing of high-alloyed stainless steels: Experimental study and theoretical modeling.* Metall. Mater. Trans. A, 2005. **36**: p. 2751-2760.